University of South Carolina

Scholar Commons

Theses and Dissertations

Spring 2022

Modification of Active Sites in Catalytic Materials for Gas-Phase Heterogeneous Catalysis

Deependra Man Shakya

Follow this and additional works at: https://scholarcommons.sc.edu/etd

Part of the Chemistry Commons

MODIFICATION OF ACTIVE SITES IN CATALYTIC MATERIALS FOR GAS-PHASE
HETEROGENEOUS CATALYSIS

by

Deependra Man Shakya

Bachelor of Science
Tribhuvan University, 2009

Master of Science
Tribhuvan University, 2013

Master of Arts
Tribhuvan University, 2015

_____

Submitted in Partial Fulfillment of the Requirements

For the Degree of Doctor of Philosophy in

Chemistry

College of Arts and Sciences

University of South Carolina

2021

Accepted by:

Donna A. Chen, Major Professor

Michael L. Myrick, Committee Member

Natalia B. Shustova, Committee Member

John R. Monnier, Committee Member

Tracey L. Weldon, Interim Vice Provost and Dean of the Graduate School

DEDICATION

This dissertation work is dedicated to my family and friends. To my parents, Mr. and Mrs. Shakya to whom I am grateful for all their sacrifices and endless encouragement during my graduate school. To my loving wife, Pawitra, for being a constant source of support and reassurance during the challenges of graduate school. To my sisters, Monica and Deepika, thank you for being by my side through thick and thin.

ACKNOWLEDGEMENTS

ABSTRACT

Heterogeneous catalysis remains at the core of chemical manufacturing industries with 80-90 % of chemical processes relying on the use of catalysts. Unlike homogeneous catalyst that has extremely well-defined active sites, active sites in heterogeneous catalysis are complex and show dynamic behavior under reaction conditions, and change their structures, composition, particle size. The complexity associated with these systems has made the rational design of the catalyst a difficult problem. Highly crystalline metal-organic frameworks (MOFs) as heterogeneous catalysts present the unique opportunity to systematically modify the geometries, ensemble sizes, and compositions of highly dispersed active sites due to their tailorable, and post-modifiable pores and cavities with uniform distribution of identical catalytic species.

In this work, we report the first study of a gas-phase hydrogenation reaction catalyzed by highly dispersed metal nodes of a crystalline, bimetallic CuRhBTC(BTC^{3-} =benzenetricarboxylate) metal-organic framework (MOF), whereas other isostructural monometallic and bimetallic MOFs has no hydrogenation activity. X-ray photoelectron spectroscopy and X-ray absorption experiments identify the oxidation state of Rh in CuRhBTC as +2, which is a Rh oxidation state that has not previously been observed for crystalline MOF metal nodes. These Rh^{2+} sites are active for the catalytic hydrogenation of propylene to propane at room temperature, and the MOF structure stabilizes the Rh^{2+} oxidation state under reaction conditions. Density functional theory calculations suggest a

mechanism in which hydrogen dissociation and propylene adsorption occur at the Rh^{2+} sites.

Based on the activity of Rh^{2+} sites for alkene hydrogenation and known activity of Rh ions for hydroformylation reaction at lower pressures (≤ 1atm), the CuRhBTC was studied as a potential catalyst for ethylene hydroformylation reaction at elevated temperature and pressures. The ethylene hydroformylation studies on monometallic CuBTC, RhBTC, bimetallic CuMBTC(M=Rh, Co, Ru ions), along with Rh-standards: Rh^{3+}/SiO_2, Rh^{2+}/SiO_2, Rh/SiO_2, Rh-Y zeolites showed Rh-containing MOFs along with Rh-standards exhibited activity for ethylene hydroformylation to propanal and diethyl ketone as reaction products, whereas the other monometallic and bimetallic MOFs did not show any activity. The increase in diethyl ketone product with increased Rh concentration suggests that ionic Rh sites are needed for the formation of the coupling product during hydroformylation.

One of the common strategies to achieve the desired activity of supported metal particles is tuning the particle size and interactions between the particle and the support. The growth of metal particles and associated loss of surface area is a major route of catalyst deactivation in heterogeneous catalysis. In our work, propylene hydrogenation activity was studied on small (1-2 nm) Pd particles deposited on different carbon and oxide supports using strong electrostatic adsorption (SEA). The size of the Pd particles was varied by annealing at higher temperatures and was assessed by chemisorption, scanning transmission electron microscopy (STEM), and x-ray diffraction (XRD) measurements. Our study showed that Pd particles deposited by SEA on graphene nanoplatelets (graphitic, oxGN-alfa) have higher activity than small, uniformly sized Pd

particles on silica. We found that the Pd exhibits a particle size effect on SiO_2 and oxGN-Alfa, with smaller particles showing higher activity whereas this effect on oxVXC72 was complicated by carbon decoration.

TABLE OF CONTENTS

LIST OF TABLES

LIST OF FIGURES

LIST OF ABBREVIATIONS

CHAPTER 1

INTRODUCTION

1.1 INTRODUCTION OF CATALYSIS

The term "Catalysis" was used by Berzelius in 1835 to describe reactions that are accelerated by a substance that remain unchanged after the reaction.[1] Paul Sabatier, 1912 Nobel prize winner, introduced the concept designated as "Sabatier principle" and provided a conceptual framework about optimum catalyst.[2] According to this concept the best catalyst should adsorb a reactant on the catalyst surface with intermediate energy: not too weakly that allows the activation but not too strongly to be able to desorb the products.[1] The International Union of Pure and Applied Chemistry (IUPAC) has defined a *catalyst* as " a substance that increases the rate of a reaction without altering the overall standard Gibbs energy change of the reaction". The chemical process of increasing the reaction rate is termed as *catalysis*.[3] Catalysis has appeared as an important area of research since it plays critical roles in many industries including petroleum refining, automotive catalytic converters, production of starting materials for organic synthesis reaction, production of fertilizers, food production, and in pharmaceuticals. Catalysis also helps in developing/designing new environmentally friendly technologies that allow green ways to generate energy in this present world struggling with problems of pollution, global warming.

Catalysis may be categorized into homogeneous and heterogeneous catalysis. Homogeneous catalysis involves the components that are dispersed in the same phase (mostly gaseous/ liquids) as the reactant molecules, whereas heterogeneous catalysis comprises reaction components that are in a different phase. Although homogeneous catalysts exhibit excellent catalytic activities and selectivities, heterogeneous catalysis is preferred over homogenous catalysis due to its ease of preparation, handling, separation of the catalysts from the products. It is also better in terms of stability, low cost, and low

toxicity. Hence, most industrial processes tend to shift towards heterogeneous catalysis. It remains at the core of chemical manufacturing generating global sales of 1.5 trillion US $ every year with 80-90 % of chemical processes relying on the use of catalysts[4] and contributing directly or indirectly to approximately 35% of the world's gross domestic products (GDP).[5] Historically, heterogeneous catalysts have been developed by trial and error. However, the modern catalysts are prepared rationally with the fundamental understanding of catalytic processes with the help of advanced spectroscopy and imaging to investigate catalytic systems under reaction conditions.[6] For example, the development of catalytic converters for automobiles was possible due to a fundamental understanding of reaction kinetics of CO oxidation and reduction of NO_x on Pt single crystals.[7]

Typically, heterogeneous catalysts consist of transition metals present in the form of nanoparticles dispersed on supports to expose the largest surface area possible to the reacting molecules. These metals have great industrial application as they have the ability to activate molecules such as H_2, N_2, O_2, CO including polyatomic molecules containing C-H, C-O, C-N, and C-Cl bonds.[5] Metal oxide, sulfides, nitrides, carbides, phosphates, and phosphides are also employed in selected applications. Taylor, in 1925, suggested that a catalyzed chemical reaction is not catalyzed over the entire solid surface of the catalyst but only at certain "active sites or centers" which could consist of an atom or ensemble of atoms distributed on the surface of the catalyst.[8] Atomic ensemble may become active due to a specific structural arrangement of atoms or due to the electronic properties of metal atoms influencing the adsorption and activation of reactants. The main goal of rational catalyst design and development is to synthesize a catalyst with sustainable activity and selectivity at a low cost. These aspects can be improved by the

tailored design of the catalytic materials with desired structures and dispersion of active sites. Unlike homogeneous catalyst that has extremely well-defined active sites, active sites in heterogeneous catalysis are complex as it mostly involves metal nanoparticles with different facets and their associated defects such as steps, kinks, and reconstruction.[9] These actives sites show dynamic behavior under reaction conditions and change their structures[10,11], composition[12], particle size[13]. Hence the complexity associated with these systems has made the rational design of the catalyst a difficult problem.

One of the common strategies to achieve the desired activity from a catalytic material is adjusting the particle size of the active sites besides tuning its composition, crystallographic structure, and geometry.[14] The activity of supported metal nanoparticle catalysts is largely dependent on the availability of surface sites to participate in the desired reaction which largely hinges on the metal particle sizes. The growth of metal particles and associated loss of surface area is a major route of catalyst deactivation in heterogeneous catalysis.[15] Several methods have been developed over the years for the preparation of metal catalysts. However, among the simplest and least expensive methods to prepare supported metal catalyst is by impregnation, where a porous oxide or carbon supports are soaked into metal precursors solutions such as tetraamine platinum(II) chloride or chloroplatinic acid[16]. The extent of the metal retained by support depends on the precursor-support interaction which could be created via electrostatic adsorption mechanism[17] and remains a basis of strong electrostatic adsorption(SEA) method[18] employed for the catalyst synthesis for the work described in the last chapter in this thesis. This method is known to produce relatively small metal particles with excellent dispersion ideal for catalytic materials.

Recently, Single-atom catalysis (SAC) has become the most active frontier in heterogeneous catalysis as it not only has a lower cost but also higher activity, selectivity, and stability compared to traditional catalysts.[19,20], For example, the Sykes group has demonstrated very small quantities of individual, isolated catalytically active Pd atoms on Cu(111) surface activate hydrogen and facilitate hydrogenation activity of alkenes to alkanes.[21] Although SACs exhibit maximum atom-utilization efficiency and unique properties compared to conventional catalysts, fabrication and maintaining the metal clusters as atomically dispersed sites under synthesis and catalysis conditions are challenging.[22] The main bottlenecks on the SACs are low loading of single atoms (SAs) and lack of scalable synthesis methods. This hinders its practical applications as high-performance catalyst requires a high density of the SAs for abundant active sites.[23] In this regard, the metal-organic frameworks (MOFs) as heterogeneous catalysts present the unique opportunity to systematically modify the geometries, ensemble sizes, and compositions of highly dispersed active sites. MOFs are a new class of hybrid inorganic/organic material consisting of metal nodes of specific geometries connected by organic linkers. MOFs are highly crystalline with exceptionally high porosity ranging from 600–6000 m^2/g surface area. For example, Figure 1.1 shows the structure of the well-studied $Cu_3(BTC)_2$ (BTC^{3-} = benzene-1,3,5-tricarboxylate, abbreviated as CuBTC), also known as HKUST-1(HKUST = Hong Kong University of Science and Technology), in which the M^{2+} ions are arranged in a paddle-wheel configuration ($M_2(O_2C-)_4$).[24] The high porosity of MOF provides a sufficient number of active sites for the catalytic reaction. The thermal and chemical stability of MOFs provides an opportunity for post-synthetic modification and metal complex functionalization that makes it a great platform

for activation of small molecules, catalysis of organic reaction, gas storage, gas separation, biomedical imaging.[25] It also features predictable, controllable, tailorable, and post modifiable pores and cavities with uniform distribution of identical catalytic species reinforced by linkers facilitating the identification of active sites and the study of reaction mechanisms in rational catalyst design.
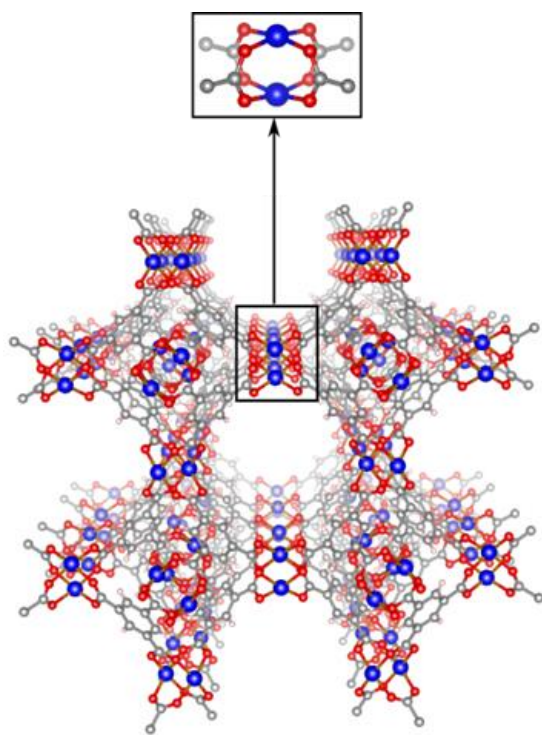
Figure 1.1. The X-ray crystal structures of $M_3(BTC)_2$ MOFs (M = Cu, Ni). Insets show the secondary building units (SBUs) of mono- and heterometallic MOFs. Blue, brown, red, and gray spheres represent M metal, oxygen, and carbon atoms, respectively.

1.2 MOTIVATION

Our research group mainly focuses on understanding surface chemistry on the atomic and molecular levels with the main objective of developing new materials for heterogeneous catalysis. The primary focus of the research discussed here is to

understand the factors and properties of bimetallic MOFs based on the HKUST-1 system for gas-phase hydrogenation and hydroformylation reactions. Although there have been several studies of catalysis on MOF nodes in the solution phase such as hydrogenation, oxidation, epoxidation[26–28], however, there is almost no experimental data on the literature for the gas phase reactions despite the fact that industrial heterogeneous catalysis on MOFs is more economical than homogeneous catalysis. There are few other studies on gas-phase catalysis on MOF reported in the literature, however, these studies involve active sites such as metal complexes or clusters that have been coordinated to the MOF nodes or linkers by post-synthetic modification.[29–31] This approach basically treats MOF as support which makes these systems synthetically more challenging and difficult to control in terms of oxidation states, nucleation, and sintering. Alternatively, metal particles have been deposited inside of MOF pores, but these catalysts still suffer from issues such as sintering and lack of control over geometry and composition of active sites as observed for active sites in the conventional supported metal catalysts.[32] Hence, the investigation discussed here employs metal nodes intrinsic to MOF structure as the catalytically active sites which have several advantages including: a homogeneous distribution of metal nodes of the metal nodes within the framework; a well-defined structure of the metal nodes crystallographically characterized that allows for theoretical investigation of the possible reaction mechanism of catalytic reactions and greatly facilitated the rational catalyst design. Hence, the scientific investigation discussed here is one of the very few fundamental studies of the mechanisms occurring in the gas phase and motivated by the desire to tailor the dispersion, geometry, ensemble size, and composition of the active sites, and to elucidate reaction mechanisms and intermediates

in the catalytic processes occurring at the MOF metal center.

For studies discussed herein, we have chosen to investigate industrially relevant hydrogenation and hydroformylation reactions. This work is one of the first gas-phase reaction studies on bimetallic MOFs that are known to display properties that are different from their monometallic entity.[33,34] All the MOF samples for these studies were synthesized by the Shustova group here at the University of South Carolina(UofSC). Shustova group is well known synthesized variety of MOFs and COFs (covalent -organic frameworks) materials for diverse applications including sustainable energy conversion, sensing, switches, and artificial biomimetic systems.[35–37] The thermally stable HKUST-1(abbreviated as CuBTC) was used as precursor material that displayed stability against air under ambient conditions and after the activation procedure required to generate unsaturated metal sites important for the catalysis.[24] The CuBTC based isostructural bimetallic MOFs: CuRhBTC, CuCoBTC, CuNiBTC, CuFeBTC, CuIrBTC were synthesized by transmetallation process. The idea here was to incorporate the active sites into the MOF nodes that can serve as the isolated sites for specific reactions as shown in Figure 1.2. Different isostructural monometallic MOFs such as CuBTC, NiBTC and, RhBTC were also studied. The incorporation of second metal ions such as Rh^{2+} in the paddlewheel node of CuBTC during the synthesis of $Cu_{3-x}Rh_x(BTC)_2$ MOF (abbreviated CuRhBTC) was reported. The introduction of the Rh ions into the paddlewheel nodes was confirmed by Raman spectroscopy and supported by density functional theory (DFT) calculations performed by the Vogiatizis group at the University of Tennessee, Knoxville. The uniform dispersion of copper and rhodium ions was shown by scanning

8

transmission electron spectroscopy(STEM) and energy-dispersive X-ray spectroscopy(EDX) on a nanometer scale.[38]

In chapter 3, the propylene hydrogenation activity on the isolated metal nodes of bimetallic CuRhBTC was discussed. This study showed the Rh-metal nodes of the crystalline CuRhBTC MOF were active for propylene hydrogenation with Rh^{2+} as an active site prepared by the reduction of post-synthetically incorporated Rh^{3+}. The
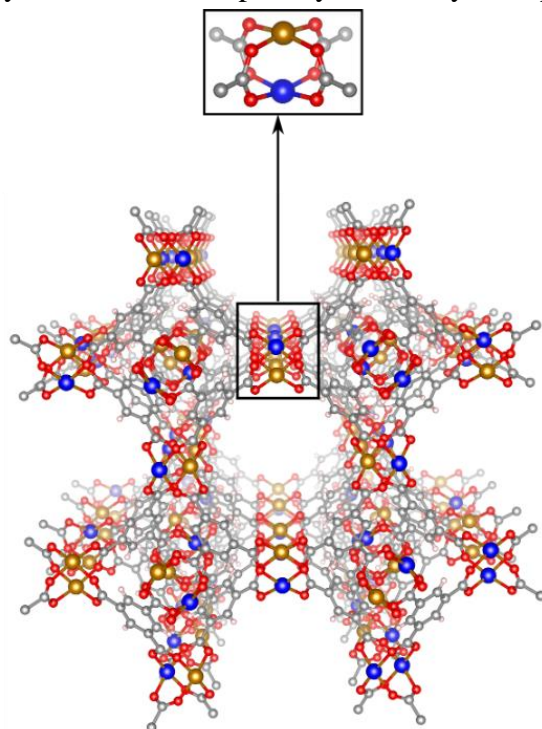
Figure 1.2. Simulated structure for heterometallic $M_{3-x}M'_x(BTC)_2$ (M' = Fe, Co, Ru, Rh, and Ir). Insets show the secondary building units (SBUs) of mono- and heterometallic MOFs. Blue, brown, red, and gray spheres represent M metal, M' metal, oxygen, and carbon atoms, respectively.

CuRhBTC displayed the unique hydrogenation activity of Rh^{2+} in CuBTC at room temperature compared to CuBTC and CuMBTC(M=Co, Fe, Ir, Ru ions) that has no appreciable activity. The Rh^{2+} ions in the bimetallic MOF structure are stable under

reaction conditions and are essential for the reaction pathway according to DFT calculations. The main role of Cu^{2+} ions in the CuRhBTC is believed to be stabilizing the MOF structures and preventing the reduction of incorporated Rh^{2+} into metallic Rh under reaction conditions.

Chapter 4 discusses the hydroformylation activity on Rh-containing MOFs. Hydroformylation is a catalytic conversion of alkene from natural gas and widely available syngas (CO and H_2) widely used industrial process for aldehyde production. These aldehydes are key ingredients for numbers build chemicals used in pharmaceutical, perfume agrochemical, and food additive industries.[39–42] Conventionally, Rh and Co have been extensively employed for the hydroformylation at higher reactant pressures(80-100atm) in homogenous catalysis setup.[39,42]Recent research has been focused on developing heterogeneous catalysts for hydroformylation due to ease of separating catalysts from the products. In addition, the supported Rh ions[43,44] and particles[45] have shown heterogeneous hydroformylation at lower pressures($\leq$ 1atm) at relatively lower temperatures but with lower selectivity compared to homogenous counterparts.[40] Hence, based on the activity of Rh^{2+} sites for alkene hydrogenation and known activity of Rh ions for hydroformylation reaction the CuRhBTC was studied as a potential hydroformylation catalyst where ethylene was used as a probe molecule. The ethylene hydroformylation reactions were also carried out on monometallic CuBTC, RhBTC, bimetallic CuMBTC(M=Rh, Co, Ru ions), along with Rh-standards such as Rh^{3+}/SiO_2, Rh^{2+}/SiO_2, Rh/SiO_2, Rh-Y zeolites. The CuBTC, CuCoBTC, and CuRuBTC did not show any activity for ethylene hydroformylation, whereas the Rh-containing MOFs: CuRhBTC, CuCoRhBTC, and RhBTC along with Rh^{3+} containing Rh-Y zeolite, Rh^{2+},

and $Rh^{3+}/SiO2$ prepared by incipient wetness impregnation exhibited catalytic

hydroformylation of ethylene to propanal. Diethyl ketone was also observed as a reaction

product for Rh-containing MOFs and standards. The increase in diethyl ketone product

with increase Rh concentration strongly suggests that a pair of neighboring Rh sites could

be essential for the formation of the coupling product during hydroformylation. This

study showed the Rh^{2+} sites in the MOF nodes had relative better hydroformylation

activity compared to Rh^{3+}species in Rh-Y zeolite. Some of the Rh-sites in the Rh-

containing MOFs could undergo reduction to metallic Rh particles known to have higher

hydroformylation activity.

The work described in Chapter 5, the investigations of catalytic activity on

carbon-supported Pd particles, was originally motivated by prior work from the Gupton

group at Virginia Commonwealth University(VCU), in which Pd particles on graphitic

supports were found to have unusually high activity for the Suzuki cross-coupling

reaction.[46] To better understand the fundamental properties of Pd on carbon catalysts

compared to oxide supports, propylene hydrogenation was chosen as a simple gas phase

probe reaction. Pd particles were deposited using the technique of strong electrostatic

adsorption (SEA), which is known to produce particles of small sizes (1-2 nm diameter)

on a number of different oxides supports, as well as oxidized carbon. The particle size of

the Pd particles was varied by annealing at higher temperatures and was estimated by

chemisorption, STEM, and XRD measurements. Our results of propylene hydrogenation

demonstrated that Pd particles deposited by SEA on various carbon supports such as

carbon black (non-graphitic, oxVCX72), and graphene nanoplatelets (graphitic, oxGN-

alfa) have higher activity than small, uniformly sized Pd particles on silica. We found that

the Pd exhibits particle size effect on SiO_2 and oxGN-Alfa, whereas this effect on

oxVXC72 was complicated by carbon decoration.

CHAPTER 2

EXPERIMENTAL TECHNIQUES

2.1. CATALYST EVALUATION - FLOW SYSTEM

This reactor system was primarily built in our lab for catalytic evaluation of novel

catalytic materials. All the catalysts for these studies were evaluated in a flow system

using a fixed bed, tubular reactor with ID 0.19" (316 steel) in a single pass. The reactor

was encased in the 1.0" OD jacketed shell with liquid inlet and outlet ports at the bottom

and top of the jacket connected to an ethylene glycol/water recirculating bath to maintain

isothermal behavior. The jacket is also wrapped with heating tape for the operations at

elevated temperatures above 100^oC and controlled by a homebuilt PID temperature

controller. The reactor is also equipped with an ATS 3210 Split Tube Furnace that can

heat the reactor to 700^oC for high-temperature reactions. A thermowell containing a K-

type thermocouple was inserted into the catalyst bed to accurately measure the reaction

temperature to ensure the isothermal behavior of the reaction. The reactor tube also

contains stainless steel Parker ABP1 series back-pressure regulator that enables the

operation at elevated pressures up to 750 psig. The flow rates of different reactants gases

such as H_2, O_2, CO, He, ethylene, propylene were controlled by a series of Brooks 5850I

Mass Flow Controller (MFC) controlled by Hastings model-400 4-channel power supply.

A detailed schematic of the MFCs is shown in Figure 2.1. The flow reactor system is

coupled with the Hewlett Packard 5890 Series II gas chromatograph equipped with

Agilent HP-PLOT/Q (30 m× 0.32mm×20μm) housing a flame-ionization detector (FID)

and a thermal conductivity detector (TCD) for the analysis of the product. All the transfer

lines were heated to ~100°C using heating tapes controlled by variacs. The majority of

feed and product were analyzed every 1-hour using the FID with the help of automatic

injection software from VICI Valco Inc. Three stainless steel 6-port switching valves

(part number, 2L6UWE) from VICI Valco Instrument Inc. were connected to direct the

flow of gas in two different configurations: a) Feed mode, b) Product mode (Figure 2.2 a

and b). These valves were encased in a heated valve enclosure (part number: HVE3) from

VICI Valco Instrument Inc. In the feed mode configuration, the gas flow was analyzed

while bypassing the reactor tube. In contrast, in the product mode configuration, the gas

analysis was carried out after it passes through the reactor tube. The kinetic

measurements and the activation energies at differential conditions were also determined

using the same reactor system. The flow reactor is equipped with a vapor-liquid

equilibrator (VLE) allowing the vapor-phase reaction of volatile liquids. A complete

schematic and image of the flow system are shown in Figures 2.3 and 2.4 respectively.
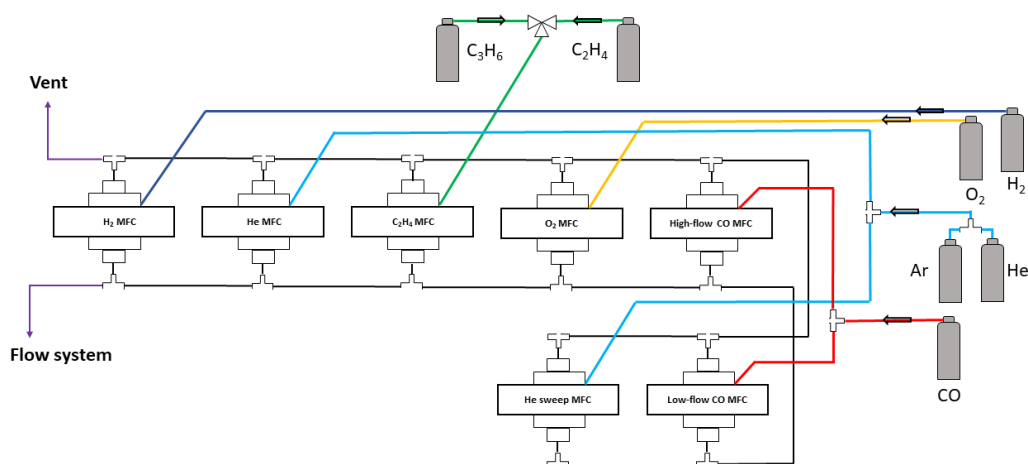
Figure 2.1. Schematic of the gas manifold containing Brooks MFCs.
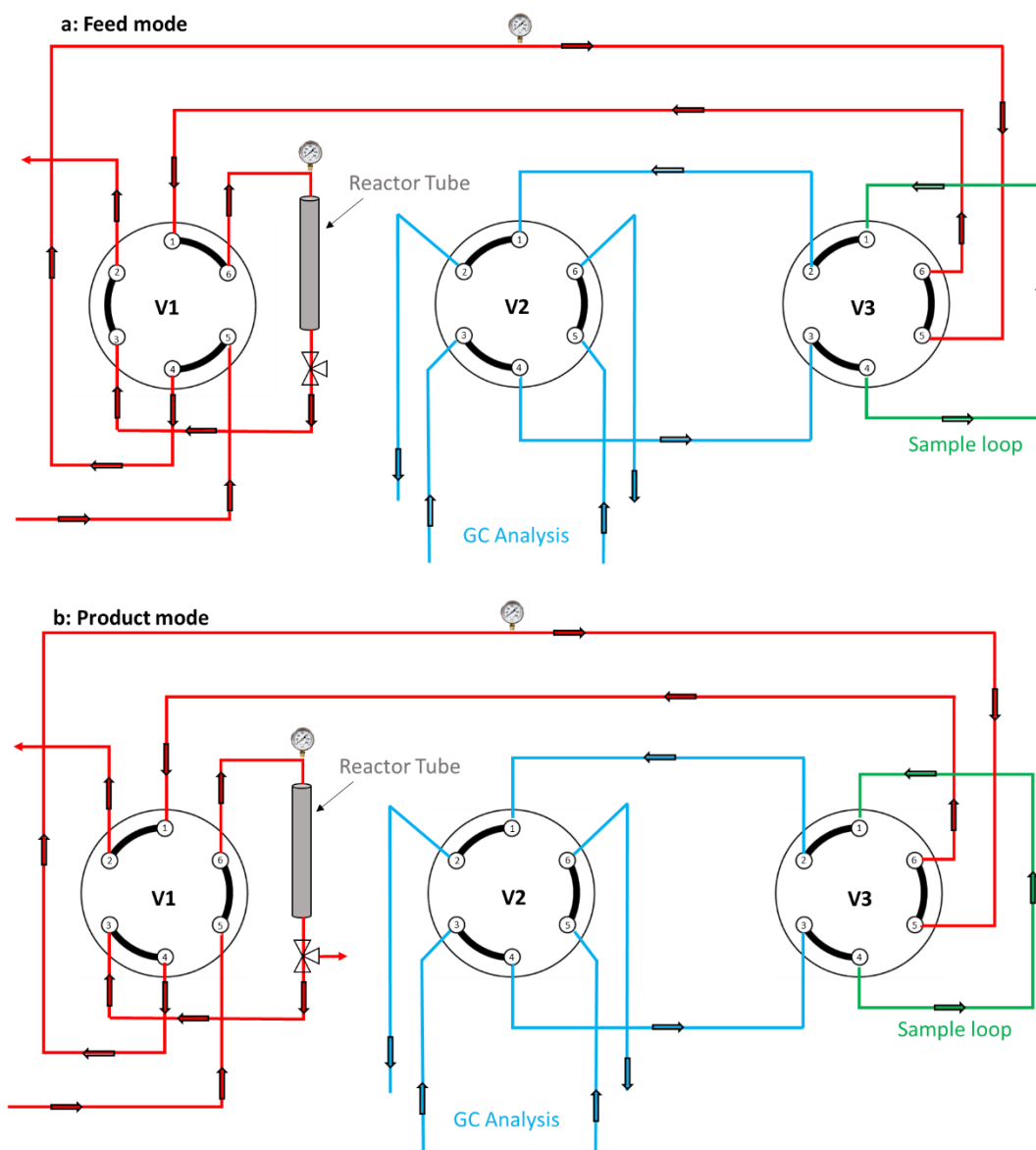
Figure 2.2. Schematic of the 6-post switching valves in a) Feed Mode, b) Product mode.
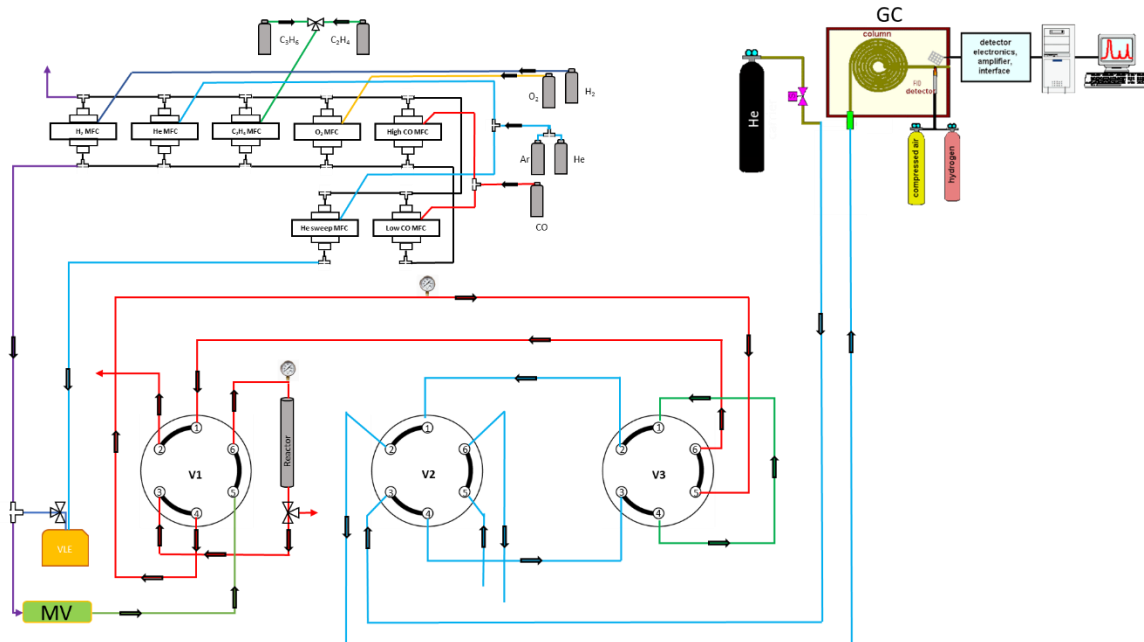
Figure 2.3. Schematic of Flow system coupled with HP 5890 Series II chromatograph

Figure 2.4. An image of a Flow system used for catalyst evaluation

2.2. X-RAY PHOTOELECTRON SPECTROSCOPY (XPS)

X-ray photoelectron spectroscopy (XPS) is one of the standard tools for surface characterization, sometimes also known as electron spectroscopy for chemical analysis (ESCA). It is a powerful technique to measure the elemental composition, empirical formula, chemical, and electronic state of an element in a material. XPS measurements involve the detection of the photoelectrons emitted from the surface under investigation due to irradiation of the sample by X-rays of known energy, typically from an Al or Mg source. The total energy transfer from the X-rays photons to the atom under irradiation
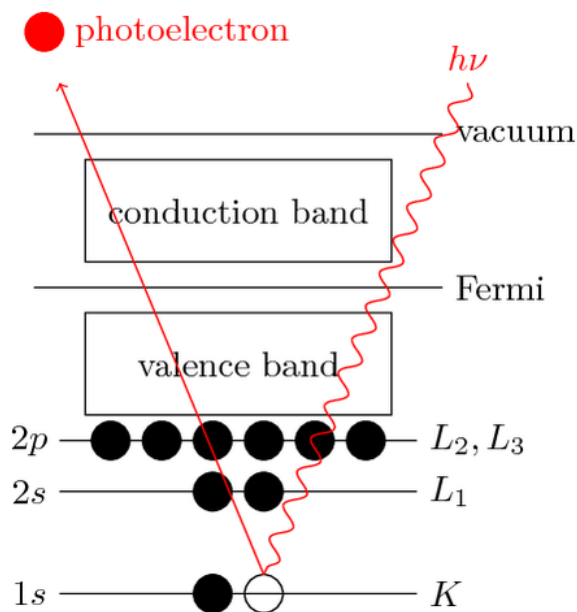
Figure 2.5: Schematic illustration of photoemission process in surface analysis. Adapted for reference 47

could lead to an electron emission, known as a photoelectron. Figure 2.5[47] shows the photoemission process that involves the generation of photoelectrons from the core level by irradiation of incident X-ray of energy (hv).

By detecting the kinetic energy ($E_{kinetic}$, KE) of the emitted electrons, it is possible to identify the surface element and chemical states. With the known energy of X-ray irradiation (E_{photon}), the binding energy ($E_{binding,}$ BE) of each emitted electron can be determined using the photoelectric effect equation 2.1. The detected components can be quantified with the help of peak intensities of XPS spectra.

$$E_{binding} = E_{photon} - (E_{kinetic} + \phi) \qquad equation\ 2.1$$

Here, $E_{photon} = h\nu$ is the energy of the incident photon energy, $E_{kinetic}$ is the detected kinetic energy of the photoelectron, and ø is the work function. The work function is related to the spectrometer for a conducting sample and represents the minimum energy required to eject an electron from the highest occupied level into the vacuum[48]. Figure 2.6 shows the schematic of the equipment and principle of XPS.
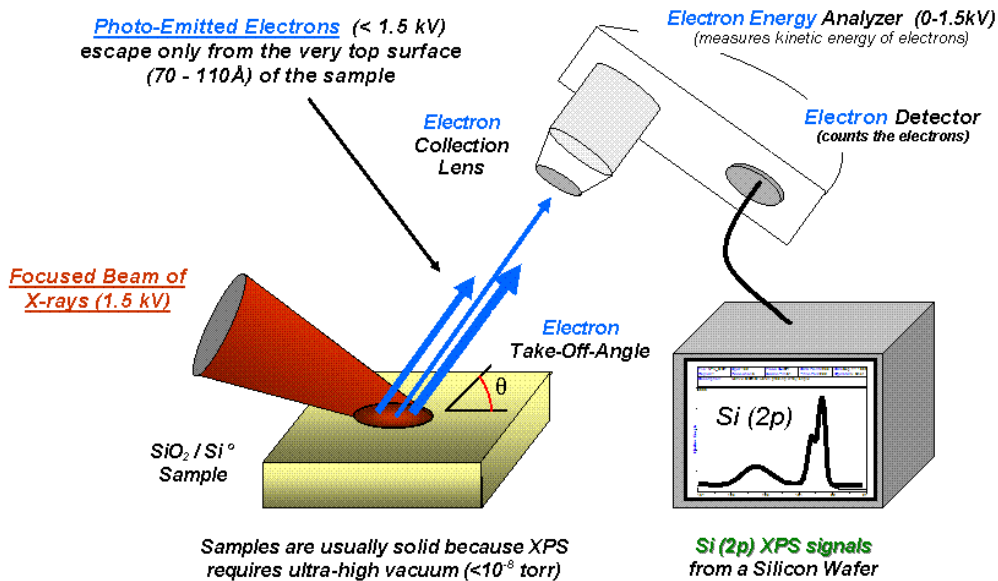
Figure 2.6: Schematic of the equipment and principle of XPS. Adapted for reference 48

19

In this thesis, XPS was mainly used to identify the oxidation state of the MOF species under investigation before and after catalysis. For this we have carried out XPS studies on a Kratos AXIS Ultra DLD system equipped with a monochromatic AlKα source, a hemispherical analyzer, charge neutralizer, catalysis cell, and a load lock chamber for rapid introduction of samples without breaking vacuum; this system has been described in more detail elsewhere.[49]

Ambient pressure XPS(AP-XPS) were carried out in an ultrahigh vacuum (UHV, $<2 \times 10^{-10}$ Torr) chamber equipped with a SPECS GmbH PHOIBOS 150 EP MCD-9 analyzer located at the Chemistry Division of Brookhaven National Laboratory (BNL).[50] The purpose of AP-XPS studies was to be able to investigate MOF powders in-situ under reactant gas pressures ≤ 0.5 Torr and elevated temperatures. The powder samples were pressed onto the aluminum plate and loaded into the analysis chamber under UHV conditions. All XPS data were collected with an Mg Kα source (1253 eV), including the O(1s), C(1s), Rh(3d), and Cu(2p) regions at an energy resolution of 0.2 eV. XPS binding energies were calibrated against the metal Fermi and core-level features of a Ru single-crystal standard and further confirmed with the position of the adventitious hydrocarbon peak.

2.3. INDUCTIVELY COUPLED PLASMA (ICP-AES/MS)

An inductively coupled plasma (ICP) is a type of plasma source produced by energy from electrical currents generated by electromagnetic induction. Inductively coupled plasma (ICP) is an analytical technique used for the detection of trace metals in environmental samples. The plasma used in the spectrochemical analysis is electrically neutral with each positive charge on an ion balanced by a free electron.[51] The ICP

technique gets the element to emit a characteristic wavelength of specific light that can be measured. ICP is often used in conjunction with other analysis techniques such as atomic emission spectroscopy (AES) and Mass spectroscopy (MS) that require the sample to be in an aerosol or gaseous form before the injection into the instrument.

In ICP-AES, plasma is used as the atomization and excitation source. A solid sample is normally dissolved and mixed in water. A plasma source dissociates the dissolved sample onto its constituent atoms or ions, exciting them to a higher energy level. Upon returning to the ground state, the dissociated ions emit the photon of a characteristic wavelength depending on the element that is recorded by an optical spectrometer to provide a quantitative analysis of the sample when calibrated against the standards. It is one of the most common techniques for elemental analysis. Dissolved samples could be analyzed from solutions containing high concentration salt solution to diluted acids solution.[52] The ICP-MS (Mass spectroscopy) is a relatively new technique that combines conventional ICP optical emission sources with a mass spectrometer. The ICP source converts the atoms of the elements in the sample to ions which are then separated and detected by the mass spectrometer. The ICP source in ICP-MS is an argon plasma source and it is extremely sensitive for determination on a wide range of elements. For the work discussed here, the relative concentration of metal ions in the MOFs was determined using a Thermo-Finnigan Element XR inductively coupled plasma-mass spectrometer (ICP-MS) at the University of South Carolina Mass Spectrometer Center. The MOF samples were washed extensively in a solvent at reflux temperature in a Soxhlet extractor to remove any residual Rh ions from MOF pores. The sample was then digested in a mixture of concentrated HCl and HNO_3 acids at 180°C

before the ICP-MS analysis.

Similarly, the mass fraction Rh^{2+} in Rh^{2+}/SiO_2 and Rh^{3+} in Rh^{3+}/SiO_2 used in this

work was analyzed using atomic absorption spectroscopy (AAS). In AAS, the acetylene

flame was used to evaporate the dissolved sample and dissociate the sample into its

component atoms. A hollow cathode lamp is selected based on the element to be

determined. Then the light from a hollow cathode lamp is passed through the cloud of

atoms where atoms of interest absorb the light from the lamp. This absorbance is then

measured by the detector and used to calculate the concentration of the element in the

sample.[53] For this work, a Perkin Elmer AAnalyst 400 was used for atomic absorption

spectroscopy analysis. The Rh^{2+}/SiO_2 was prepared following a procedure mentioned in

the literature[54]. For determination on Rh wt.% loading, the Rh^{2+}/SiO_2 catalyst was

digested in aqua regia solution whereas, for Rh $^{3+}$, the impregnating $RhCl_3$ solution was

analyzed.

2.4. X-RAY POWDER DIFFRACTION (PXRD)

X-ray powder diffraction pattern (PXRD) is a scientific technique for structural

characterization of materials using a monochromatic X-ray on powder or microcrystalline

samples. Bragg's approach to diffraction from the crystal considers a crystal made up of

layers or planes of atoms such that each act as a semi-transparent mirror. When irradiated

with X-rays, some of the X-rays are reflected off a plane with an angle of reflection equal

to the angle of incidence, but the rest are transmitted to be subsequently reflected by

succeeding layers/planes o atoms.[55] When Bragg's law (equation 2.2) is satisfied, the

reflected beams are on-phase and interfere constructively resulting in a diffraction

pattern.

$$2d\sin\varTheta = n/\lambda\ldots\ldots\textit{ Bragg's Law-----Eq. 2.2}$$

Where θ is the angle of incidence of the X-ray, n is an integer, λ is the wavelength, and d is the spacing between atom layers. In principle, a monochromatic beam of X-rays strikes a finely powdered sample that has randomly arranged crystals in every possible orientation to diffract in a pattern characteristic of the structure. Powder diffraction is often more convenient and easier than single-crystal diffraction as it does not require a single crystal to be made and it represents a diffraction pattern of the bulk material compared to a single crystal which does not necessarily represent the overall material. Compounds/materials can be identified using a database of diffraction patterns a most of the material has unique diffraction patterns. The particle size of the powder can also be determined by using the Scherrer formula, which relates the particle size to the peak width. The Scherrer formula is,

$$p = \frac{k\lambda}{\beta Cos\theta}$$

Where, p = true particle size,

k=Scherrer constant (shape factor),

λ= wavelength of Cu Kα radiation,

β= width of diffraction peak given in radians after subtracting instrumental broadening,

θ= Bragg's angle

A powder X-ray diffractometer consists of an X-ray source, a sample stage, a detector, and a way to vary the angle Θ. The X-ray is focused on the sample at an angle Θ, while the detector resides opposite to the source reads the intensity of X-ray at 2Θ

23

away from the source path as shown in Figure 2.7[56]. The incident angle is then increased

over time while the detector angle always remains 2Θ above the source.[57] The detector

position is recorded as 2Θ while the detector records the number of X-rays observed at

each 2Θ. The sample is also rotated to keep the X-tray beam properly focused.
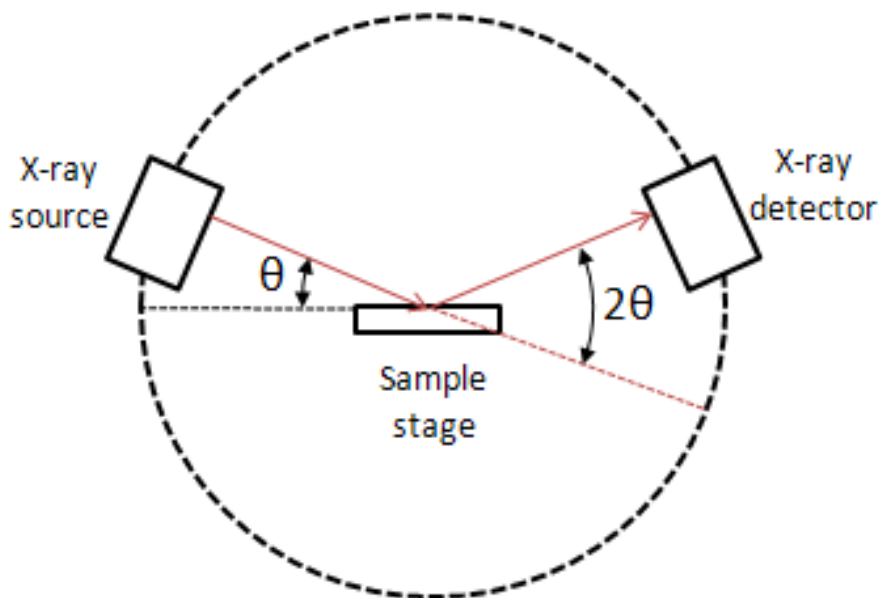
Figure 2.7: Diffraction showing the incoming and diffracted beams that are inclined by an angle theta with respect to the sample surface. Adapted from reference 56.

The crystallinity of as-synthesized and activated MOFs were ensured by PXRD

analysis. PXRD was also performed on post-reaction samples to check the structural

integrity of MOFs after being exposed to reaction conditions as described in Chapters 3

and 4. For this work, powder XRD patterns were recorded on Rigaku Miniflex II

diffractometer with an angular range of 3 to 30° in 2Θ with a step size of 0.02 °,

accelerating voltage, and current of 30kV and 15 mA respectively.

For the work described in chapter 5, particles sizes of the Pd particles on different carbon and oxide supports were measured by X-ray diffraction method using a Rigaku Miniflex II equipped with a D/teX Ultra silicon strip detector. Diffraction patterns were collected over a range of 10-70° 2Θ using Cu-Kα radiation operated with accelerating voltage of 15kV and current of 30mA. About 0.1 g of the sample was placed in Rigaku XRD holders of diameter 20 mm and depth of 0.2 mm. XRD patterns were obtained for all metal-free supports in addition to the supported metal catalysts. A prominent peak at 2Θ = 40° is observed for Pd (111) which was analyzed for the determination of the crystallite size of the nanoparticles. A Fityk 1.3.1 version software was employed for background subtraction and deconvolutions using pseudo-Voigt shapes to take the peak asymmetry into account. The full width at half maximum (FWHM) values was used together with a shape factor of 0.94 in the Scherrer equation to estimate particle size.[58]

2.5. CHEMISORPTION

Chemical adsorption, or chemisorption, is a process resulting from a chemical bond between adsorbate molecules and specific surface locations on the material, known as the active sites. The interaction is much stronger in the case of physical adsorption, or physisorption. Chemisorption is a single layer process occurring on active sites and ceases in the absence of direct contact with the surface, whereas physisorption is a less strong interaction taking place on all surfaces under favorable temperature and pressure conditions.

The chemisorption measurement technique is used to evaluate the physical and chemical properties of materials important for reaction performance. It is one of the most important methods of catalyst characterization used to measure the number of available

active sites in the catalysts and the temperature at which the catalyst becomes active after reduction/oxidation cycles. These measurements can be carried out either in static mode to distinguish between strong or weak active sites or in pulsed chemisorption mode to probe strong active sites only.[59] Either of these chemisorption processes is conducted at a temperature of interest to determine the number of accessible active sites, active surface area, degree of dispersion, and active particle size of heterogeneous catalysts. Hydrogen and carbon monoxide are the two most used probe gases. Oxygen and other gases are also used in suitable cases.

A pulsed chemisorption experiment is carried out at ambient pressure with a flowing gas. After the sample is cleaned in a flowing inert gas, small pulses of reactant gas are injected until the sample is saturated. The quantity of reactant molecules adsorbed by the active sites upon injection is measured by a calibrated thermal conductivity detector (TCD). Typically, the initial injections are chemisorbed completely; however, upon saturation, none of the later injections will be chemisorbed[60]. The number of molecules of gas chemisorbed is directly related to the active surface area of active material.

The quantity of the gas chemisorbed per gram of sample combined with the knowledge of the stoichiometry of the reaction and the quantity of active metal used during the catalyst synthesis is used to calculate the metal dispersion. This information can also be used to calculate the metallic surface area per gram of metal, particle size using the following equations[60,61],

$$PD = 100 \times \left(\frac{V_s \times SF_{Calc}}{SW \times 22414} \right) \times GMW_{Calc}$$

$$SA_{Metallic} = \left(\frac{V_s}{SW_{Metal} \times 22414} \right) \times (SF_{Calc}) \times (6.022 \times 10^{23}) \times SA_{Calc}$$

$$APS = \cfrac{6}{D_{Calc} \times \left(\cfrac{W_S}{GMW_{Calc}}\right) \times (6.022 \times 10^{23}) \times SA_{Calc}}$$

PD = Percent dispersion

D_{calc} = Calculated metal density(g/cm^3)

$SA_{Metallic}$ = Metallic surface area (m^2/g of metal)

APS = Active particle size (nm), hemispherical

V_s = Volume of adsorbed gas (cm^3 at STP)

SF_{Calc} = Stoichiometry factor

W_S = Sample Weight

SA_{Calc} = Calculated specific surface area (per gram of metal)

GMW_{Calc} = Calculated gram molecular weight of the sample(g/g-mole)

For the work described in Chapter 5, pulsed chemisorption was performed to investigate the particle size of the Pd on various catalysts synthesized for the study. The measurements were performed using the AutoChem II 2920 instrument where the number of active Pd-sites and the active particles sizes were determined by chemisorption of oxygen pre-covered hydrogen titration of the Pd catalyst surfaces. The sample was first reduced in 10% H$_2$ at 200°C for 1 hour before Ar- treatment at 200°C for an hr followed by cooling it to 40°C. The sample was then treated with 10% O$_2$/Balance Ar at 40°C for 30 minutes to oxidize Pd to PdO. The sample was then purged with Ar-gas to remove the residual loosely held oxygen molecules from the sample. It was then titrated with pulses 10% hydrogen/ balance-Ar to form water and Pd surfaces with chemisorbed hydrogen. The hydrogen consumption by the sample was detected by a thermal conductivity detector (TCD). The assumed overall stoichiometry is 0.667 Pd:1 H$_2$[62]. Particle sizes were estimated from chemisorption assuming hemispherical geometry. For Pd particles

supported on carbon, Regalbuto *etal*[63] have shown a systematic discrepancy in metal

dispersion and nanoparticle sizes obtained from chemisorption and XRD techniques.

They have hypothesized this discrepancy was due to the formation of a carbon overlayer,

termed as carbon decoration, on the surface of metal nanoparticles during catalysis

synthesis. Hence, an additional particle sizes characterization with Scanning transmission

electron microscopy was considered for this study.

2.6. SCANNING TRANSMISSION ELECTRON MICROSCOPY(STEM)

Scanning transmission electron microscopy (STEM) is a transmission electron

microscope where the images are generated by the electrons passing through a thin

specimen. In STEM, the microscope lenses are adjusted to create a focused electron beam

probe that scans over the sample as shown in Figure 2.8[64]. The rastering of the electron

beam across the sample creates an image suitable for Z-contrast imaging, elemental

mapping by energy-dispersive X-ray spectroscopy (EDS), and electron energy loss
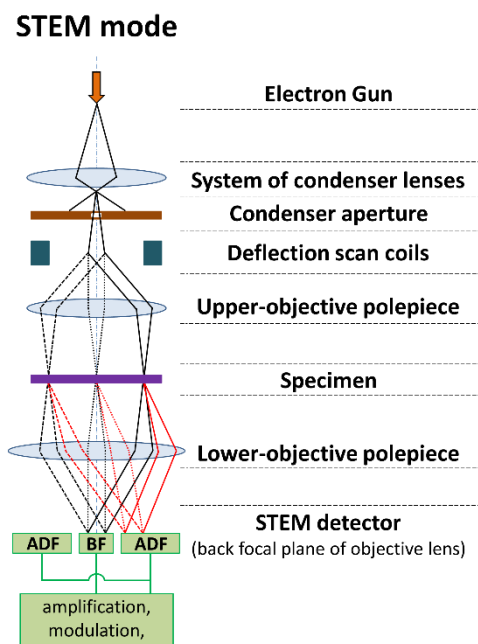
Figure 2.8. Schematic view of STEM.
Adapted from reference 64

28

spectroscopy (EELS). STEM is used to characterize the nanoscale and atomic-scale structure of materials including solar cells[56], batteries[65], semiconductors[66], fuel cells[67], catalysts[68], etc.

For the studies discussed in chapter 5, the aberration-corrected JEOL 2100F scanning transmission electron microscopy (STEM) was used for Z-contrast imaging with a 200 kV field emission gun and a double tilt holder for tilting the sample across a range of angles (±20°). High Angle Annular Dark-Field (HAADF) STEM images were acquired on a Fischione Model 3000 HAADF detector with a camera length such that the inner cut-off angle of the detector was 50 mrad. Sample preparation involved suspending the catalyst in isopropanol and depositing a drop of the suspension onto a holey carbon film attached to a Cu TEM grid. A Digital Micrograph software was used to obtain images and 100-500 particles from each image were counted to get the particle size distributions. The average diameter of the particles was calculated given relations,

Surface average diameter = $D_s = \sum n_i d_i^3 / \sum n_i d_i^2$

Volume average diameter = $D_v = \sum n_i d_i^4 / \sum n_i d_i^3$

where n_i is the number of particles with diameter D_i.

CHAPTER 3

SELECTIVE CATALYTIC CHEMISTRY AT RHODIUM (II) NODES IN

BIMETALLIC METAL-ORGANIC FRAMEWORKS

3.1. INTRODUCTION

The use of crystalline metal-organic frameworks (MOFs) as heterogeneous catalysts provides the unique opportunity to tailor active site geometries and ensemble sizes on the atomic scale. MOFs are crystalline hybrid inorganic/organic materials with structures consisting of metal nodes of specific geometries connected by organic linkers. Furthermore, the high porosity (600–6000 m^2/g surface area)[1] of MOFs provides a sufficient number of highly dispersed active sites for catalytic reactions.

MOFs are reported to be excellent catalysts for a number of reactions in the liquid phase, including hydrogenation, oxidation, and epoxidation.[2–6] However, gas-phase heterogeneous catalysis is preferred over reactions in the liquid phase due to the ease of separating the catalyst from the products in the former case. Given their extraordinarily high surface areas, MOFs have been used as supports for metal particles in gas-phase reactions.[7,8] Similarly, catalytically active metal complexes or clusters have been attached to the MOF nodes by post-synthetic modification.[9–12] In comparison to these catalysts that employ the MOF as a support, the use of metal nodes intrinsic to the MOF structure as the catalytically active sites has several advantages. These include: a homogeneous distribution of the metal nodes within the framework; and a well-defined structure of the metal nodes, which can be fully characterized by crystallography and can be investigated theoretically to predict the possible mechanisms of catalytic transformations.

In this work, we present the first study of gas-phase catalytic activity occurring at the metal nodes of a crystalline MOF and investigate possible reaction mechanisms using density functional theory (DFT) calculations. Specifically, $(Cu_xRh_{1-x})_3(BTC)_2$ (abbreviated CuRhBTC, where BTC_{3-}=benzenetricarboxylate) is found to catalyze

31

propylene hydrogenation to propane with relatively high activity and excellent long-term stability. This bimetallic MOF is prepared via solid-state metathesis using $Cu_3(BTC)_2$ (HKUST-1) as a precursor. To the best of our knowledge, this is the first report of a 2+ oxidation state for isolated Rh ions in a MOF; these Rh^{2+} ions are not stabilized by the presence of Rh-Rh bonds at Rh dimer nodes and are produced through the reduction of post synthetically incorporated Rh^{3+}. This unusual Rh^{2+} oxidation state provides the active sites for the reaction, given that activity increases with Rh concentration. DFT studies were used to model the active Rh^{2+} sites within the CuRhBTC structure and to identify an energetically favorable reaction mechanism in which H_2 dissociation and propylene adsorption occur at isolated Rh^{2+} sites.

3.2. EXPERIMENTAL METHODS

MOF sample preparation before analysis

All MOFs were activated by heating in vacuo on a Schlenk line at the temperatures and times specified in Table 3.1. The purpose of this activation process was to remove solvent and adsorbed water from the undercoordinated metal sites of the MOFs. Powder X-ray diffraction (PXRD) collected before and after activation showed no loss in MOF crystallinity for CuBTC (Appendix A, Figure A.1), CuRhBTC (Figures A.4-A.5), and the other CuMBTCs (Figures A.3, A.6, A.7, and A.8). For the x-ray photoelectron spectroscopy (XPS), Extended X-ray absorption fine structure spectroscopy (EXAFS), X-ray near-edge spectroscopy (XANES), and catalysis experiments, the "as-prepared" MOFs were activated, for the TGA and PXRD experiments, the "as-synthesized" MOFs were unactivated.

Table 3.1. Procedure showing temperature and time for activation of mono- and bimetallic MOFs.

MOFs	Activation Procedure (temperature, time)
$Cu_3(BTC)_2$	$160^{\circ}C$, 48 hours
$Ni_3(BTC)_2$	$120^{\circ}C$, 48 hours
$Cu_{2.82}Ru_{0.18}(BTC)_2$ [CuRu(6%)BTC]	$160^{\circ}C$, 24 hours
$Cu_{2.01}Rh_{0.99}(BTC)_2$[CuRh(33%)BTC]	$160^{\circ}C$, 24 hours
$Cu_{2.46}Rh_{0.54}(BTC)_2$[CuRh(18%)BTC]	$160^{\circ}C$, 24 hours
$Cu_{2.85}Ir_{0.15}(BTC)_2$[CuIr(5%)BTC]	$160^{\circ}C$, 24 hours
$Cu_{2.82}Ni_{0.18}(BTC)_2$[CuNi(6%)BTC]	$120^{\circ}C$, 48 hours
$Cu_{1.5}Co_{1.5}(BTC)_2$[CuCo(50%)BTC]	$120^{\circ}C$, 48 hours

Propylene hydrogenation catalysis

All the MOF catalysts were evaluated for propylene hydrogenation in a 316 stainless steel 0.19" ID packed bed, tubular flow reactor which has been previously described in more detail elsewhere.[13] A jacketed shell around the reactor tube was used to maintain the isothermal temperature of $20^{\circ}C$ that is connected to a recirculation bath containing a coolant mixture of glycol/H_2O. A heating tape wrapped around the body of the reactor was used to achieve the higher temperatures controlled by a homebuilt temperature controller, and the temperature of the reactor was monitored by a thermocouple inserted directly into the catalyst bed. Feed composition was maintained by a series of mass flow controllers (Brooks 5850E series). The feed gas mixture for propylene hydrogenation was 5% C_3H_6/ 20% H_2/balance He at a total flow rate of 100 sccm. The gas analysis was carried out with a Hewlett-Packard 5890 Series II

chromatograph equipped with an HP-PLOT/Q capillary column($30m \times 0.320mm \times 20\mu m$, Agilent) using a flame ionization detector (FID). After removal from the Schlenk line, the activated MOF samples (20.0 mg) were placed in a nitrogen-purged closed vial and immediately introduced into the catalytic reactor. All of the MOF catalysts were re-activated in the reactor by heating under 50 sccm of pure He at 100° C-150°C (details in Table 3.1) for 2-3 hours to remove water and other gases that adsorbed during transfer to the reactor. For the $Rh_2(OAc)_4$ (6.80 mg), $RhCl_3$ (6.44 mg), and incipient wetness Rh^{3+}/SiO_2 (30.0 mg, 1.91 weight % Rh) catalysts, the catalyst weight was chosen in order to match the number of Rh ions (1.85×10^{19}) in the CuRh(33%)BTC sample (20.0 mg), based on MOF weight directly after activation and the assumption that all adsorbates from the undercoordinated sites have been removed in the activated sample. For the activation energy experiments with the $Rh_2(OAc)_4$ and CuRhBTC catalysts and for all experiments with the MOF catalysts, the conversion was less than 15%, with the exception of CuRh(33%)BTC at 50 $^\circ$C, which reached 40% conversion.

 XPS studies

XPS studies were carried out on a Kratos AXIS Ultra DLD system equipped with a monochromatic AlKα source, a hemispherical analyzer, charge neutralizer, catalysis cell, and a load lock chamber for rapid introduction of samples without breaking vacuum; this system has been described in more detail elsewhere.[14] The samples could be directly transferred from the XPS analysis chamber to the catalysis cell without exposure to air. In the catalysis cell, samples were exposed to a flow of pure H_2 at room temperature or 50 °C. The MOF samples were evacuated in the load lock chamber overnight before introduction into the main vacuum chamber for XPS. Since a charge neutralizer was used

to prevent sample charging, binding energies for all samples were corrected by setting the position of the adventitious carbon peak to 284.8 eV.[14] After removal from the Schlenk line, the MOF samples were transferred to a closed glass vial and placed in an aluminum holder that had been heated to the same temperature as the sample.[14] The samples remained in the aluminum holder while being transported to the XPS facility and were still hot when introduced into the load lock chamber.

AP-XPS experiments were carried in an ultrahigh vacuum (UHV, $<2\text{x}10^{-10}$ Torr) chamber equipped with a SPECS GmbH PHOIBOS 150 EP MCD-9 analyzer located at the Chemistry Division of Brookhaven National Laboratory (BNL).[15] The powder catalysts were pressed onto a plate made of aluminum and then loaded into an analysis chamber under UHV conditions. All samples were activated in the analysis chamber in UHV at 150 °C for 1.5 hours. For the in-situ reactivity tests, a reaction mixture of 32 mTorr of H_2 (Praxair) and 8 mTorr of C_3H_6 (Praxair) was used while the sample was at room temperature. All XPS data were collected with a Mg Kα source (1253 eV), including the O(1s), C(1s), Rh(3d), and Cu(2p) regions at an energy resolution of 0.2 eV. XPS binding energies were calibrated against the metal Fermi and core-level features of a Ru single-crystal standard and further confirmed with the position of the adventitious hydrocarbon peak.

EXAFS and XANES studies

X-ray absorption fine structure (XAFS) measurements were performed at the Cu and Rh K-edges. XAFS data were collected in transmission and fluorescence modes at 32° C at the QAS beamline (7-BM) at NSLS-II. For fluorescence measurements, a passivated implanted planar silicon (PIPS) detector (Mirion) was used. Extended XAFS

(EXAFS) spectra were collected by scanning a Si (111) monochromator energy across the absorption edge (from 200 eV below the edge through 1000 eV above the edge). The spectral acquisition time was 5 minutes per scan. Rh and Cu foils measured in reference position simultaneously with the samples were used to calibrate and align the obtained spectra in absolute energy. To improve the signal-to-noise ratio, a total of 25 or 30 scans were collected and averaged for samples containing Rh or Cu, respectively. The samples were prepared in a glove box by finely grinding the powders using a mortar and pestle. Some samples were packed into Kapton capillaries (1.23 mm OD, 1.13 mm ID, and 13 mm long) that were sealed with clay on both ends. For comparison, we also prepared samples by spreading the powders onto adhesive tapes and folding them several times for sufficient thickness for transmission experiments. To minimize harmonics in the incident X-ray beam, a Pt coated mirror was used with a fully tuned Si(111) monochromator for Rh K-edge measurements, and for Cu K-edge measurements, a Rh coated mirror was used with the monochromator detuned by 20%. The ionization chambers were filled with 10% N_2/90% Ar when collecting at the Rh edges. At the Cu K-edges, the ionization chambers were filled with pure N_2 gas for the incident beam detector and 70% N_2/30% Ar for the transmission and reference detectors. The vertical slit size was 1.7 mm, and the horizontal slit size was 4 mm. Rh-containing standard compounds with different oxidation state: (Rh(0), Rh(I): $[Rh_2(CO)_2Cl]_2$; Rh(II): $Rh_2(OAc)_4$; Rh(III): $RhCl_3$) were also measured in transmission mode and used for comparison with the bimetallic $(Cu_xRh_{1-x})_3(BTC)_2$ system.

EXAFS data processing was performed using the Athena and Artemis programs of the Demeter package.[16,17] EXAFS data analysis of Rh and Cu K-edge spectra was

carried out by fitting theoretical EXAFS spectra to the experimental data in r-space; a Hanning window function was applied to the k^2 (or k^3) - weighted data for Fourier transforms. In the first step, a fit of Cu and Rh spectra collected from their respective foils was performed to obtain the values of the amplitude reduction factors S_0^2. The obtained values of S_0^2 for Cu (Rh) foils: 0.85 (0.84), respectively, were subsequently fixed in the fits of the experimental EXAFS data of Cu and Rh edges in the bimetallic $(Cu_xRh_{1-x})_3(BTC)_2$ samples and Rh in the $Rh_2(OAc)_4$ standard compound. The fitting models were constructed using crystallographic data for CuBTC and the $Rh_2(OAc)_4$ dimer structure. Theoretical EXAFS spectra were constructed by using the FEFF6.2 code, which was incorporated in the Artemis program. For the Cu K-edge, fits of EXAFS signals were performed with k^3 weighting in the 3-15 $Å^{-1}$ k-range and 1.1-2.55 $Å$ r-range. Theoretical contributions of Cu-O and Cu-Cu were included in the model. Fits of EXAFS signal were performed with k^3 weighting in the 1.5-15 $Å^{-1}$ k-range and 1.2-2.5 $Å$ r-range. The scattering contributions from Rh-O and Rh-Rh were included.

ICP-MS analysis

Relative concentrations of metal ions in the MOFs were determined using a Thermo-Finnigan Element XR inductively coupled plasma-mass spectrometer (ICP-MS) instrument at the University of South Carolina's Mass Spectrometer Center. MOFs were digested in a mixture of concentrated hydrochloric acid and nitric acid at 180 °C. Before ICP analysis, the MOFs were extensively washed in a solvent at reflux temperature in a Soxhlet extractor to ensure that no residual metal salts remained in the pores of the MOF.

Computational Studies

Unrestricted density functional theory (DFT) computations were performed with the Gaussian 09 program package[18] using the M06-L[19] functional, and the def2-TZVPP
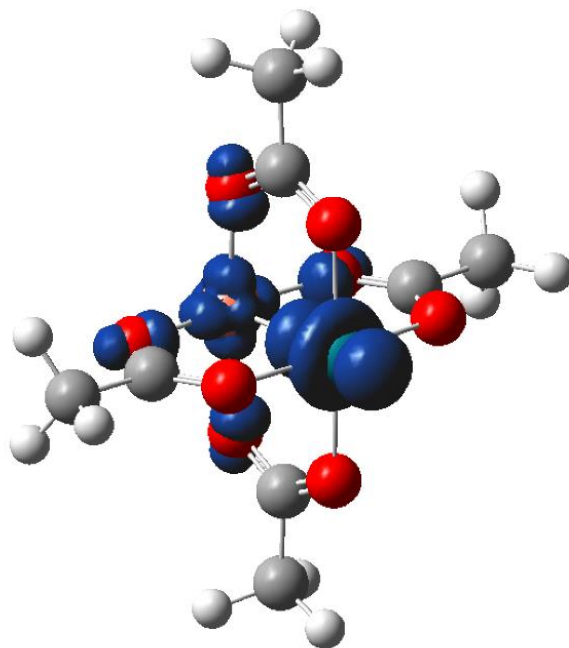
Figure 3.1. The spin density of the triplet state calculated at the M06-L/def2-TZVPP level of theory (isovalue of 0.01 a.u.) for the CuRh heteronuclear node used to model CuRhBTC.

(Cu, Rh atoms) and def2-TZVP (C, O, H atoms)[20] basis sets. All calculations for the CuRh bimetallic node of CuRhBTC were performed for the triplet ground state and compared to the singlet spin state[21]; to decrease the complexity of the calculations, the CuRhBTC MOF structure was modeled as a single paddle-wheel node with four carboxylate ligands that were each terminated by a hydrogen atom as shown in Figure 3.1.

3.3. RESULTS AND DISCUSSION

Propylene hydrogenation experiments were carried out on the monometallic CuBTC and NiBTC MOFs, as well as a variety of Cu-containing bimetallic MOFs
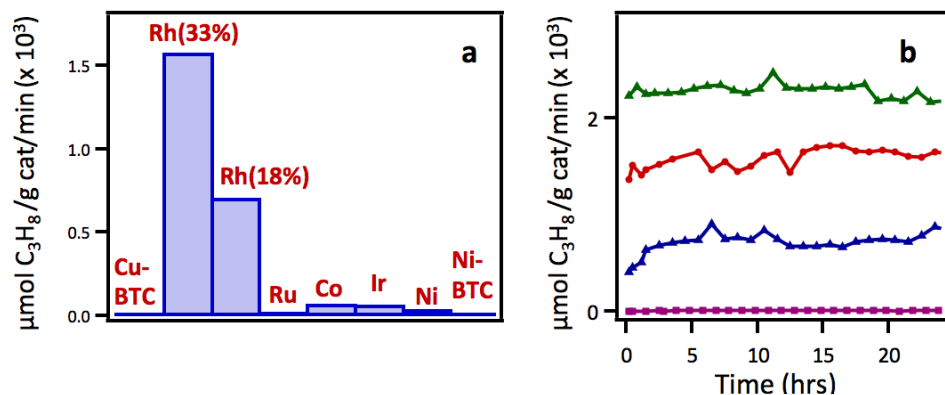
Figure 3.2. a) Average propylene hydrogenation activity for the following CuMBTC and pure MBTC MOFs: CuBTC, CuRh(33%)BTC, CuRh(18%)BTC, CuRu(6%)BTC, CuCo(50%)BTC, CuIr(5%)BTC, CuNi(6%)BTC at 100 °C and NiBTC at 100 °C; and b) activity for propylene hydrogenation as a function of time on stream over CuRhBTC with the following Rh concentrations: 18% Rh at 20 °C (blue triangles) and 50 °C (green triangles); 33% Rh at 20 °C (red circles); and 0% Rh (pure CuBTC) at 20 °C (pink squares). All activities in (a) are at 100 °C unless otherwise specified.

$((Cu_xM_{1-x})_3(BTC)_2)$ where M=Rh, Co, Ni, Ir, and Ru, as shown in Figure 3.2a. Only the

CuRhBTC exhibited significant activity for propane production at 20 °C (~1600 umol/g

catalyst/min for CuRh(33%)BTC). Specifically, the pure CuBTC MOF showed no

activity under the same reaction conditions, indicating that the Cu^{2+} ions are not active

for propylene hydrogenation. Pure NiBTC also had no appreciable hydrogenation

activity. Monometallic RhBTC could not be studied due to its loss of crystallinity upon

exposure to air, and the instability of RhBTC is attributed to the fact that the paddle-

wheel configuration of the metal nodes is highly strained for Rh ions.[22] For all MOF

catalysts, PXRD data were collected immediately after reaction, and catalysts exhibited

the same high crystallinity observed before reaction. The activity of the CuRh(33%)BTC

catalyst is also stable over a 24 period on stream (Figure 3.2b). Moreover, CuRhBTC

with a lower bulk concentration of Rh (18%) has 45% of the activity of the

CuRh(33%)BTC, which indicates that activity scales linearly with Rh concentration and

implies that the Rh ions are the active sites for reaction. At 50 °C, the reaction rate for

CuRh(18%)BTC is 3.2 times higher than at 20 °C and is stable over the entire period on

stream. The apparent activation energy for propylene hydrogenation on CuRhBTC was

determined to be 6.3 kcal/mol based on data collected at 20-50 °C (Figure 3.3a).

Figure 3.3. Determination of apparent activation energy (E_a) for: a) propylene
hydrogenation activity on the CuRhBTC MOF at temperatures between 20 °C
and 50 °C; and b) a plot of ln rate vs. 1/T yielding a slope that corresponds to
E_a=6.3 kJ/mol. Based on the activity of the CuRhBTC at 20 °C, the Rh
concentration is estimated to be ~18%.

X-ray photoelectron spectroscopy (XPS) experiments address the oxidation state

of the Rh ions in CuRhBTC (Figure 3.4). For the as-prepared sample, the Rh($3d_{5/2}$) peak

has a binding energy of 309.2 eV. The spectrum of dirhodium (II) tetraacetate

($Rh_2(OAc)_4$) provides a standard for the relatively uncommon Rh^{2+} oxidation state, which

appears at 308.9 eV for $Rh_2(OAc)_4$ and is similar to the value observed for CuRhBTC.

Furthermore, the Rh(3d) spectra for highly dispersed Rh^{2+} ions prepared from incipient

wetness impregnation of $Rh_2(OAc)_4$ on silica shows identical binding energies and peak

widths to that of CuRhBTC; therefore, the relative broadness of the Rh($3d_{5/2}$) peak for
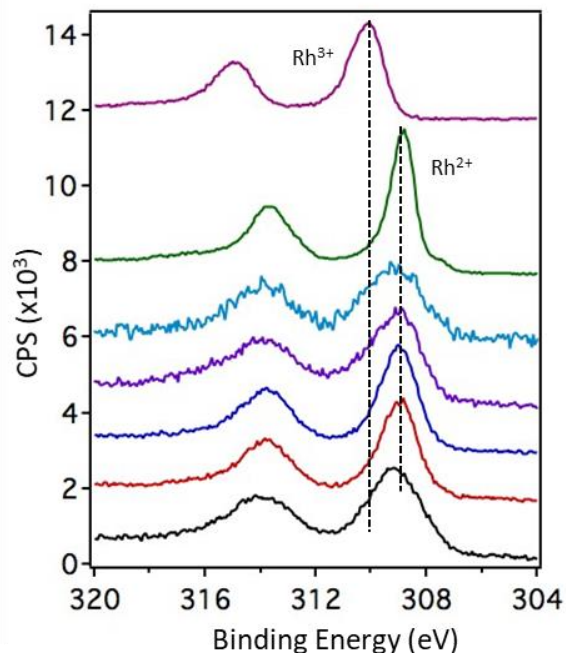
Figure 3.4. X-ray photoelectron spectroscopy data for the Rh(3d) region for the CuRh(33%)BTC MOF: after activation by heating at 160 °C in vacuo for 24 hours (black); after heating in flowing H_2 at room temperature for 2 hours (red); after heating in flowing H_2 at 50 °C for 2 hours (blue); and after propylene hydrogenation at 20 °C and 50 °C in the reactor (purple, MOF catalyst from Figure 3.2). Spectra for a $Rh_2(OAc)_4/SiO_2$ catalyst prepared by incipient wetness impregnation (light blue x7), crystalline $Rh_2(OAc)_4$ (green, x0.5), and $RhCl_3$ (purple, x0.5) are shown for comparison of binding energies.

CuRhBTC cannot be attributed to mixed oxidation states since $Rh_2(OAc)_4/SiO_2$ is equally

broad and contains only Rh^{2+}. In contrast, Rh^{3+} in $RhCl_3$ appears at 310.1 eV, which is

consistent with Rh^{3+} oxidation states reported in the literature,[23] whereas Rh^{1+} is expected

at 308.0-308.4 eV.[23,24] There is no evidence for metallic Rh at 307.0-307.4 eV[23,25] in the

spectrum of CuRhBTC. In addition, the Rh^{2+} ions in CuRhBTC are stable under reducing

conditions since the exposure of CuRhBTC to flowing H_2 at room temperature and 50 °C

results in almost no change in binding energy. The nearly identical Rh(3d) peak shapes

for the as-prepared MOF and the post-reaction catalyst used for the hydrogenation

experiment in Figure 3.2 are also consistent with a stable Rh^{2+} oxidation state during the

reaction.
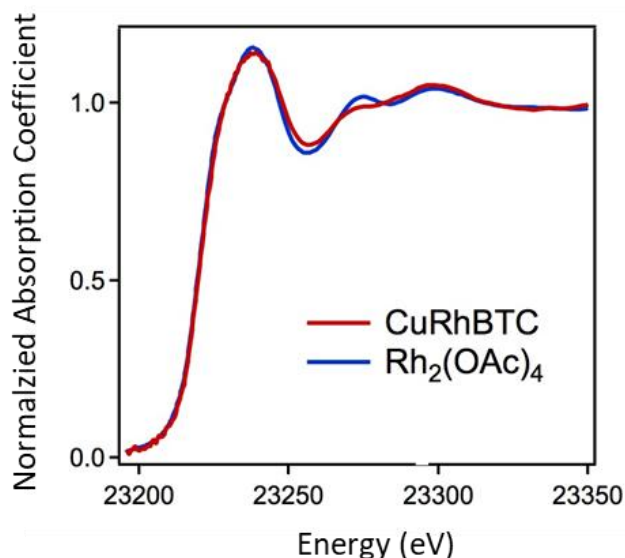
Figure 3.5. Rh-K edge XANES spectra for CuRhBTC and Rh2(OAc)4.

The XANES data provide further evidence for the assignment of the Rh^{2+}

oxidation state in CuRhBTC. As shown in Figure 3.5, the Rh K-edge is nearly identical

for CuRhBTC and the Rh2(OAc)4, which has an oxidation state of +2. In contrast, the Rh

K-edges for RhCl3 and [Rh(I)(CO)2Cl]2 have distinctly different XANES features

compared to those in the CuRhBTC spectrum (Figure 3.6a). The Cu K-edge for

CuRhBTC is identical to that for CuBTC; a comparison with the spectrum of Cu(II)

oxide indicates that the Cu oxidation state in CuRhBTC is consistent with Cu^{2+}, whereas

the Cu(I) oxide and metallic Cu(0) standards exhibit different spectra (Figure 3.6b).
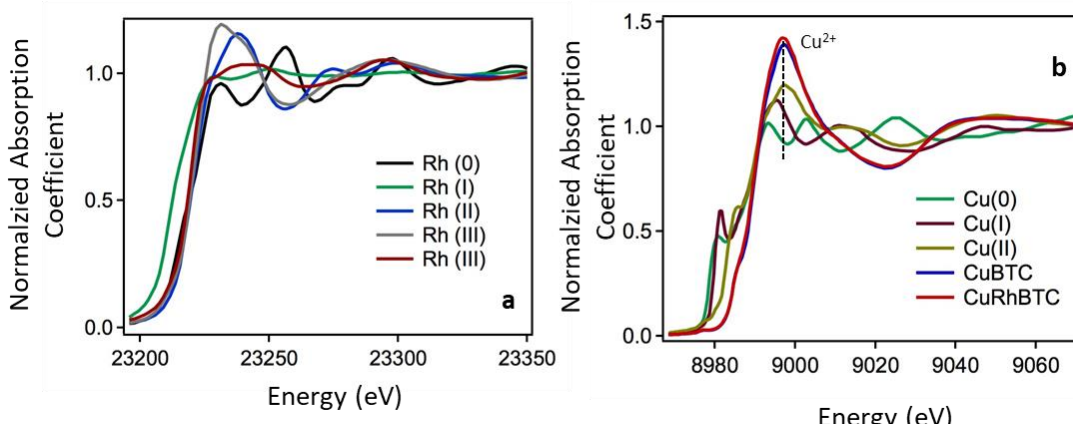
Figure 3.6. XANES spectra of the Rh and Cu standards: a) Rh-K edge XANES data for rhodium (0) foil (black), rhodium (I) dicarbonyl chloride (green), dirhodium (II) tetraacetate (blue), rhodium (III) oxide (grey) and rhodium (III) chloride (burgundy); and b) Cu-K edge XANES data for CuBTC (blue), CuRhBTC (red) and copper oxide standards: copper (0) foil (green), copper (I) oxide (violet) and copper (II) oxide (olive).

Ambient pressure (AP)-XPS studies establish that the Rh oxidation state in CuRhBTC does not change during exposure to the reactant gases or pure H_2. Figure 3.7 shows the Rh(3d) region for the CuRhBTC and this same sample: after activation by heating at 150 °C for 1.5 hours in ultrahigh vacuum (UHV); during exposure to 32 mTorr H_2/8 mTorr propylene at room temperature; and in UHV following the H_2/propylene exposure. The Rh(3d) spectrum collected during exposure to 20 mTorr H_2 is also shown for another CuRhBTC sample that was initially activated at 150 °C in UHV. In all cases, the Rh(3d) spectra exhibit no appreciable change in peak shape or binding energy, implying that the Rh oxidation state remains Rh^{2+} under all conditions, and this behavior is also consistent with the Rh(3d) spectrum of the post-reaction CuRhBTC (Figure 3.4).

Both the XPS and AP-XPS studies demonstrate that the CuRhBTC contains Cu^{2+} as the main species although Cu^{1+} is also present (Figure 3.8: Cu(2p), Cu AES, and C(1s) regions). Previous studies by our group have established that reduction of Cu^{2+} to Cu^{1+} in

pure CuBTC is induced by the combination of X-ray irradiation and heating to remove coordinating solvent molecules.[14] The fact that the post-reaction CuRhBTC exhibits a $Cu(2p_{3/2})$ peak identical to that of the pre-reaction MOF suggests that there is no change in the oxidation state of the Cu ions after propylene hydrogenation (Figure 3.8). Moreover, exposure of CuRhBTC to H_2 at room temperature does not cause a significant reduction of Cu^{2+}. Consequently, there is no direct evidence that reduction of Cu^{2+} plays a role in propylene hydrogenation, particularly since CuBTC, which also contains both Cu^{1+} and Cu^{2+}, is inactive for propylene hydrogenation.
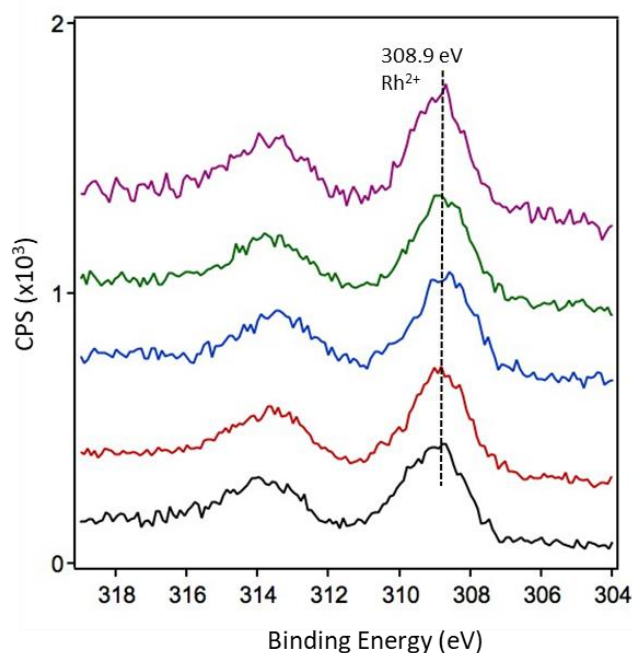
Figure 3.7. X-ray photoelectron spectroscopy data for the Rh(3d) region the CuRhBTC: after pumping down in the UHV chamber (black); after heating at 150 °C in UHV for 1.5 hours (red); during heating in 20mTorr H_2/20 mTorr propylene at room temperature (blue); in UHV after exposure to H_2/propylene (green); and during heating in 20mTorr H_2 at room temperature (pink).
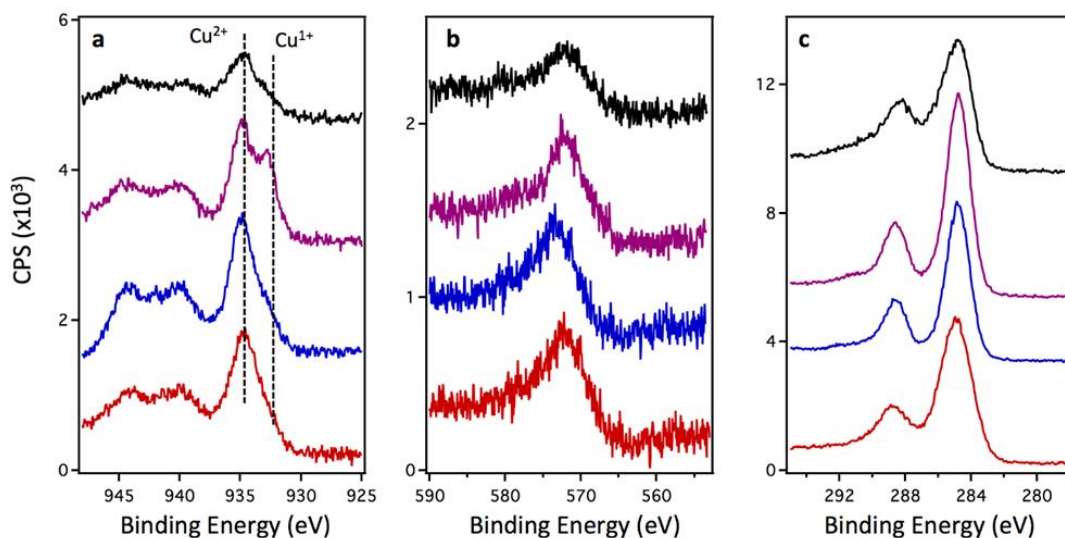
Figure 3.8. X-ray photoelectron spectroscopy data for the CuRh(33%)BTC: as-prepared (red); after exposure to flowing H_2 at room temperature for 2 hours (blue); after heating in flowing H_2 at 50 °C for 2 hours (pink); and the CuRhBTC sample after propylene hydrogenation at 20 °C and 50 °C in the catalytic reactor (black). The following regions are shown: a) Cu(2p); b) Cu(KLL); and c) C(1s). If metallic Cu were present, it should appear as a prominent peak at ~568 eV in the Cu(KLL) spectrum. In (c), the ratio of the adventitious carbon (284.8 eV): MOF carbon (288.7 eV) peaks does not increase for the post-reaction MOF, demonstrating that nonselective decomposition of propylene to atomic carbon (284.8 eV) does not occur during propylene hydrogenation.

To understand the intrinsic activity of the Rh^{2+} site, propylene hydrogenation was also studied on dirhodium (II) tetraacetate ($Rh_2(OAc)_4$); this species served as a molecular model for the pure Rh paddle-wheel node. At 20 °C, crystalline $Rh_2(OAc)_4$ exhibits stable hydrogenation activity (11,000 umol/g cat/min), which confirms that Rh^{2+} ions provide the active sites (Figure 3.9a). The apparent activation energy for the $Rh_2(OAc)_4$ catalyst determined from activity measurements at 0–40 °C is 5.4 kcal/mol (Figure 3.9b), which is a value similar to that of CuRhBTC and suggests a common mechanism. Hydrogenation activity for Rh^{2+} is consistent with reports in the literature for $Rh_2(OAc)_4$,[26] as well as for Rh^{2+} ions in amorphous coordination polymers containing
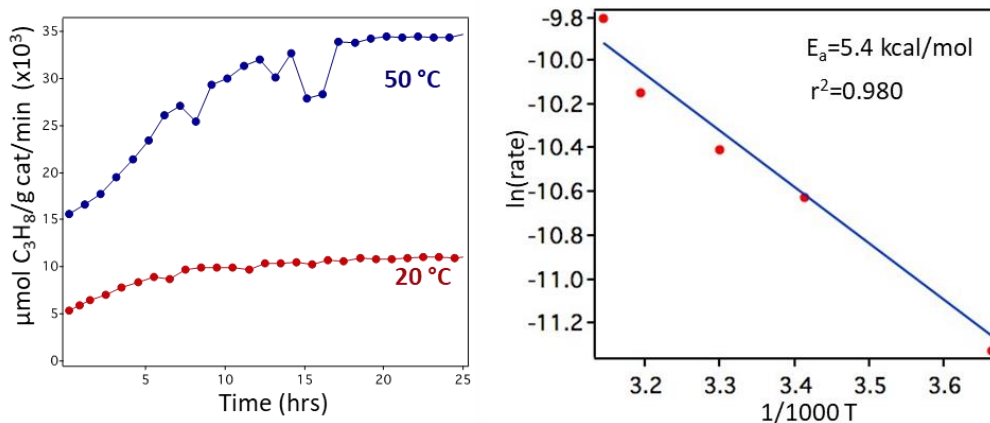
Figure 3.9. a) Activity as a function of time on stream for propylene hydrogenation over $Rh_2(OAc)_4$ at 20 °C (red) and 50 °C (blue). **b)*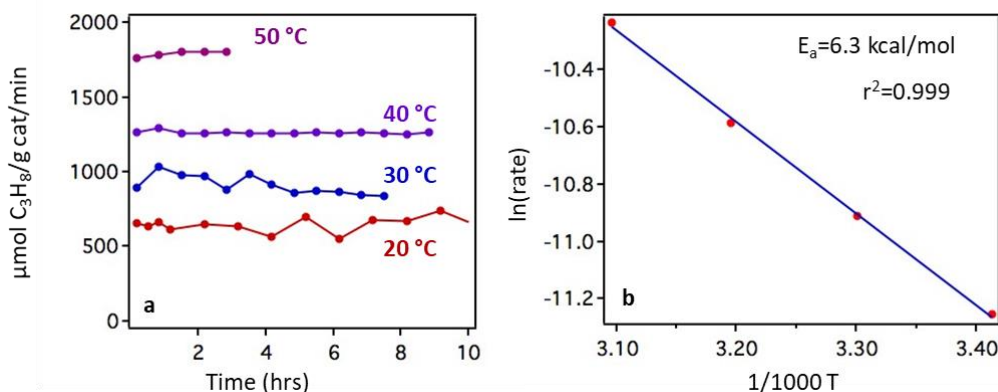* Determination of apparent activation energy (E_a) for propylene hydrogenation activity on $Rh_2(OAc)_4$ at temperatures between 0 °C and 40 °C: a plot of ln rate vs. 1/T yielding a slope that corresponds to E_a=5.4 kcal/mol.

dinuclear rhodium paddle-wheel units.[22,27] However, the Rh^{2+} active site in $Rh_2(OAc)_4$ is unstable under reaction conditions, in contrast to the high stability of Rh^{2+} in CuRhBTC.
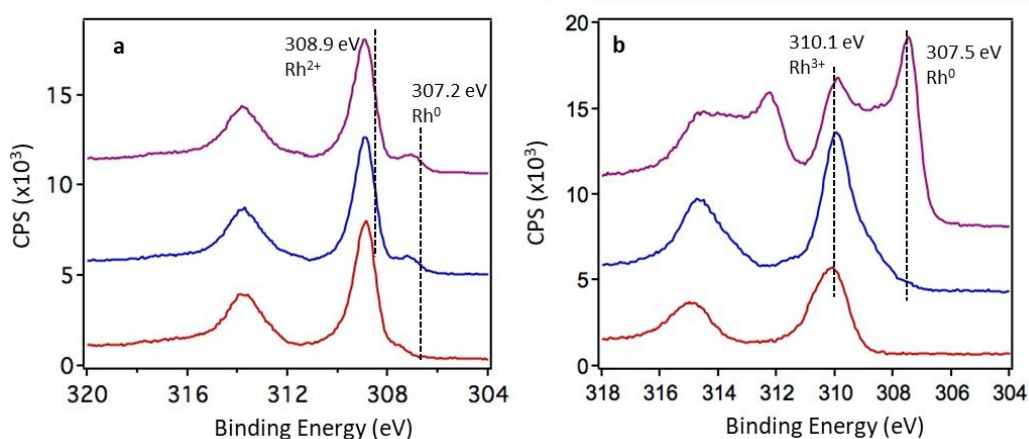
Figure 3.10. XPS data for the Rh(3d) region for: a) $Rh_2(OAc)_4$ and b) $RhCl_3$: as-prepared (red); after exposure to flowing H_2 at room temperature for 2 hours (blue); and after exposure to flowing H_2 at 50 °C for 2 hours (pink).

Specifically, $Rh_2(OAc)_4$ is reduced to metallic Rh after exposure to H_2 at 50 °C (Figure 3.10), and the unstable propylene hydrogenation activity for $Rh_2(OAc)_4$ at 50 °C (Figure

46

3.9a) is attributed to the reduction of Rh^{2+} to metallic Rh, as confirmed by post-reaction XPS and XRD studies.
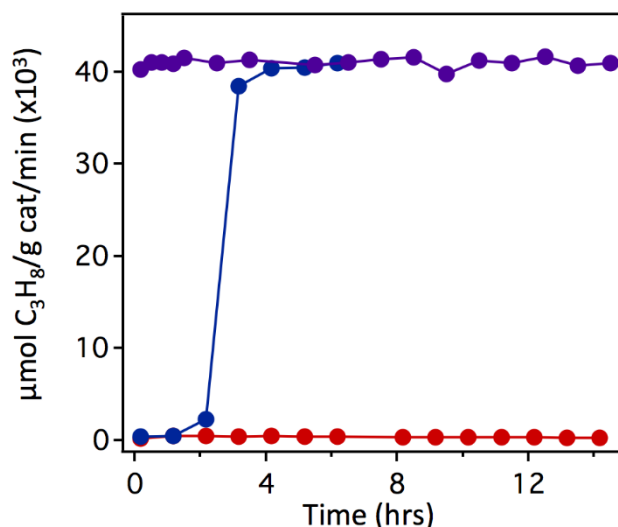
Figure 3.11. Activity as a function of time online for propylene hydrogenation over the $RhCl_3$ catalyst: initially at 20 °C (red); at 50 °C (blue); and after cooling back down to 20 °C (purple). The jump in activity at 50 °C from zero to 100 % conversion is attributed to the reduction of Rh^{3+} to metallic Rh. After returning to 20 °C, the conversion remains at 100% due to the presence of metallic Rh.

Hydrogenation activity of the CuRhBTC cannot be attributed to the presence of residual Rh^{3+} ions retained in the MOF pores after exposure to $RhCl_3$ during ion exchange because $RhCl_3$ itself has no activity for propylene hydrogenation at 20 °C (Figure 3.11). Furthermore, Rh^{3+} becomes reduced at 50 °C under hydrogenation conditions, as demonstrated by the activity data as well as XPS data for $RhCl_3$ exposed to H_2 at 50 °C.

In order to better understand propylene hydrogenation on CuRhBTC, DFT studies were carried out to investigate the reaction mechanism. All calculations were performed with the Gaussian09 program package[18] using the M06-L[19] functional and the def2-TZVPP[20] basis set. The full reaction profile for propylene hydrogenation catalyzed by the bimetallic CuRh node of CuRhBTC is shown in Figure 3.12. The relative energy differences for the intermediates and transition states with respect to the CuRh node and
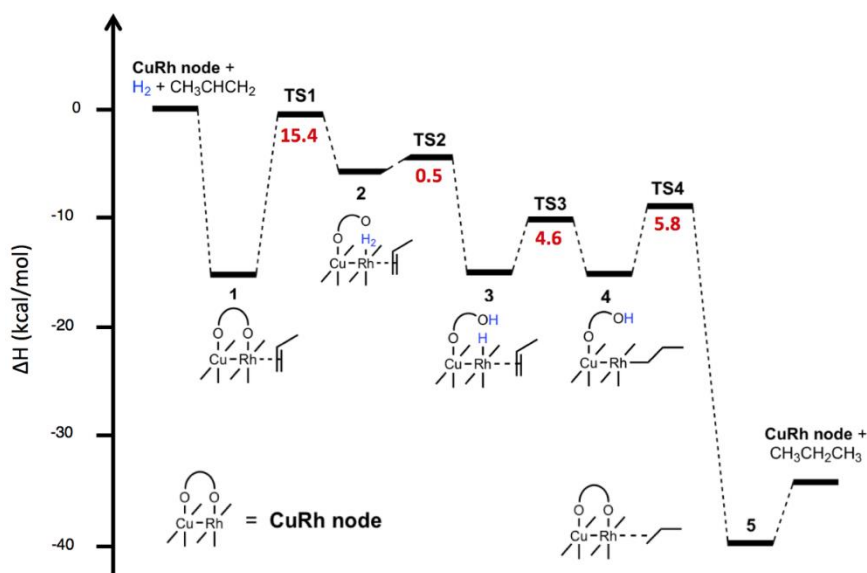
Figure 3.12. Reaction profile of the hydrogenation of propene catalyzed by the bimetallic CuRh node of the MOF.

the reactants, as well as key bond distances that demonstrate the evolution of the reaction could be found elsewhere.[21]

The first step in the reaction mechanism is the coordination of propylene at the open site of the Rh^{2+} cation (intermediate **1**) via π-backbonding; propylene adsorbs more strongly than H_2 at Rh^{2+} sites by ~13 kcal/mol. In intermediate **1**, Rh can be considered as a hexacoordinated metal after accounting for a weak bond with the Cu^{2+} cation, and therefore the mechanism for H_2 dissociation is not obvious. Several possible mechanisms were considered, including H_2 dissociation on pentacoordinated Rh^{2+} and direct H-

transfer to propylene for the formation of a propyl radical. However, the lowest energy

pathway for H_2 dissociation involves cleavage of the Rh-O bond to create a second

vacant site in the coordination sphere of Rh^{2+} for the binding of H_2. Although this step

has relatively high activation energy, the decoordinated oxygen atom facilitates H_2

dissociation in the next step via the formation of OH.[28] Furthermore, the reaction barrier

for H_2 dissociation is only 0.5 kcal/mol (**TS2**) and leads to the thermodynamically more

stable intermediate **3**. After the H_2 bond is cleaved, a Rh monohydride and a hydroxyl

group are formed. Next, the hydrogen atom of the Rh-hydride is transferred to propylene

(**TS3**) to form the Rh-propyl intermediate **4**. Finally, a second hydrogen atom from the

hydroxyl group is transferred to the propyl radical (**TS4**) for the formation of the final

product. The desorption of propane and reformation of the Rh–O bond close the catalytic

cycle. Note that the activation energy barrier for Rh-O bond dissociation (~15 kcal/mol)

is higher than the experimentally measured activation energy of 6.3 kcal/mol. A possible

explanation for this discrepancy is that CuRhBTC serves as a pre-catalyst, where species

2 provides the active sites, and the Rh-O bond is not reformed in the catalytic cycle. In

that case, the addition of hydrogen to adsorbed propyl would be the rate-limiting step,

and the calculated barrier of 5.8 kcal/mol agrees well with the experimental value.

Investigations were also conducted on $Rh_2(OAc)_4$ as a model system for addressing

activity at monometallic Rh^{2+} sites, and a similar mechanism for reaction on $Rh_2(OAc)_4$

was reported. Spin density plots for the CuRh node of CuRhBTC demonstrate the lack of

significant overlap between the half-filled $4d_z$ orbital on Rh^{2+} and the half-filled $3d_{x2-y2}$

on Cu^{2+}. These results suggest minimal electronic interaction between the two metal

centers, but a more detailed investigation of the bimetallic interactions and their role in the reaction is the topic of an ongoing study.

3.4. CONCLUSION

In summary, this study represents the first report of gas-phase catalysis at the metal nodes of a crystalline MOF, as well as the first report of Rh^{2+} MOF nodes prepared via the reduction of post synthetically incorporated Rh^{3+}. Propylene hydrogenation activity at room temperature is observed for CuRhBTC, whereas CuBTC itself and CuMBTC (M = Co, Ir, Ni, Ru ions) have no appreciable activity, thus illustrating the unique hydrogenation activity of Rh^{2+} in the CuBTC framework. The Rh^{2+} ions in the bimetallic MOF structure are stable under reaction conditions for up to 24 hours and are essential for the reaction pathways, as demonstrated by DFT calculations. The main role of the Cu ions in CuRhBTC is believed to be the stabilization of the MOF framework, which prevents incorporated Rh^{2+} from becoming reduced to metallic Rh under reaction conditions. This work provides a fundamental understanding of the rational design of MOF catalysts, which exhibit the exceptionally high selectivity typically associated with homogeneous catalysts but are more stable under reaction conditions than their molecular analogs.

ACKNOWLEDGMENTS

3.5. REFERENCES

1. Wang, C., Liu, D. & Lin, W. Metal-organic frameworks as a tunable platform for designing functional molecular materials. *J. Am. Chem. Soc.* **135**, 13222–13234 (2013).

2. Bhasin, M. M., McCain, J. H., Vora, B. V., Imai, T. & Pujadó, P. R. Dehydrogenation and oxydehydrogenation of paraffins to olefins. *Appl. Catal. A Gen.* **221**, 397–419 (2001).

3. Beier, M. J. *et al.* Aerobic Epoxidation of Olefins Catalyzed by the Cobalt-Based Metal-Organic Framework STA-12(Co). *Chem. - Eur. J.* **18**, 887 (2012).

4. Furukawa, H., Cordova, K. E., O'Keeffe, M. & Yaghi, O. M. The Chemistry and Applications of Metal-Organic Frameworks. *Science (80-.).* **341**, 1230444 (2013).

5. Miniussi, E. *et al.* Non-local effects on oxygen-induced surface core level shifts of Re(0001). *J. Phys. Chem. C* **116**, 23297–23307 (2012).

6. Ji, P. F. *et al.* Single-Site Cobalt Catalysts at New Zr12(μ3-O)8(μ3-OH)8(μ2-OH)6 Metal-Organic Framework Nodes for Highly Active Hydrogenation of Nitroarenes, Nitriles, and Isocyanides. *J. Am. Chem. Soc.* **139**, 7004 (2017).

7. Drake, T., Ji, P. F. & Lin, W. B. Site Isolation in Metal-Organic Frameworks Enables Novel Transition Metal Catalysis. *Acc. Chem. Res.* **51**, 2129 (2018).

8. Zhao, M. *et al.* Metal-organic frameworks as selectivity regulators for hydrogenation reactions. *Nature* **539**, 76–80 (2016).

9. Islamoglu, T. *et al.* Postsynthetic Tuning of Metal-Organic Frameworks for Targeted Applications. *Acc. Chem. Res.* **50**, 805 (2017).

10. Yang, D. *et al.* Tuning Zr6 Metal-Organic Framework (MOF) Nodes as Catalyst Supports: Site Densities and Electron-Donor Properties Influence Molecular Iridium Complexes as Ethylene Conversion Catalysts. *ACS Catal.* **6**, 235–247 (2016).

11. Otake, K. I. *et al.* Single-Atom-Based Vanadium Oxide Catalysts Supported on Metal Organic Frameworks: Selective Alcohol Oxidation and Structure Activity Relationship. *J. Am. Chem. Soc.* **140**, 8652 (2018).

12. Li, Z. *et al.* Sintering-Resistant Single-Site Nickel Catalyst Supported by Metal-Organic Framework. *J. Am. Chem. Soc.* **138**, 1977–1982 (2016).

13. Zhang, Y., Diao, W., Williams, C. T. & Monnier, J. R. Selective hydrogenation of acetylene in excess ethylene using Ag- and Au-Pd/SiO2 bimetallic catalysts prepared by electroless deposition. *Appl. Catal. A Gen.* **469**, 419–426 (2014).

14. Duke, A. S. *et al.* Active Sites in Copper-Based Metal-Organic Frameworks: Understanding Substrate Dynamics, Redox Processes, and Valence-Band Structure. *J. Phys. Chem. C* **119**, 27457–27466 (2015).

15. Palomino, R. M. *et al.* Interfaces in heterogeneous catalytic reactions: Ambient pressure XPS as a tool to unravel surface chemistry. *J. Electron Spectros. Relat. Phenomena* **221**, 28–43 (2017).

16. Newville, M. IFEFFIT: Interactive XAFS analysis and FEFF fitting. *J. Synchrotron Radiat.* **8**, 322–324 (2001).

17. Ravel, B. & Newville, M. ATHENA, ARTEMIS, HEPHAESTUS: Data analysis for X-ray absorption spectroscopy using IFEFFIT. *J. Synchrotron Radiat.* **12**, 537–541 (2005).

18. Frisch, M. J. *et al.* G16_C01. Gaussian 16, Revision C.01, Gaussian, Inc., Wallin (2016).

19. Zhao, Y. & Truhlar, D. G. The M06 suite of density functionals for main group thermochemistry, thermochemical kinetics, noncovalent interactions, excited states, and transition elements: Two new functionals and systematic testing of four M06-class functionals and 12 other function. *Theor. Chem. Acc.* **120**, 215–241 (2008).

20. Weigend, F. & Ahlrichs, R. Balanced basis sets of split valence, triple zeta valence and quadruple zeta valence quality for H to Rn: Design and assessment of accuracy. *Phys. Chem. Chem. Phys.* **7**, 3297–3305 (2005).

21. Shakya, D. M. *et al.* Heterogeneous Catalysis Hot Paper Selective Catalytic Chemistry at Rhodium (II) Nodes in Bimetallic Metal – Organic Frameworks Angewandte. **29208**, 16533–16537 (2019).

22. Nickerl, G., Stoeck, U., Burkhardt, U., Senkovska, I. & Kaskel, S. A catalytically active porous coordination polymer based on a dinuclear rhodium paddle-wheel unit. *J. Mater. Chem. A* **2**, 144–148 (2014).

23. Lang, R. *et al.* Hydroformylation of Olefins by a Rhodium Single-Atom Catalyst with Activity Comparable to RhCl(PPh3)3. *Angew. Chemie - Int. Ed.* **55**, 16054–16058 (2016).

24. Zhou, X. S. *et al.* Self-assembly of a Rh(I) complex on Au(111) surfaces and its electrocatalytic activity toward the hydrogen evolution reaction. *Langmuir* **23**, 6819–6826 (2007).

25. Wagner, C. D., Riggs, W. M., Davis, L. E. & Moulder, J. F. *Handbook of X-ray Photoelectron Spectroscopy*. (1979).

26. Hui, B. C. Y., Teo, W. K. & Rempel, G. L. Activation of Hydrogen by Bridged Transition Metal Carboxylates. Rhodium(II) Acetate Catalyzed Hydrogenation of Olefins. *Inorg. Chem.* **12**, 757–762 (1973).

27. Sato, T. *et al.* Novel microporous rhodium(II) carboxylate polymer complexes containing metalloporphyrin: Syntheses and catalytic performances in hydrogenation of olefins. *J. Catal.* **232**, 186–198 (2005).

28. Szécsényi, Á. *et al.* Breaking Linear Scaling Relationships with Secondary Interactions in Confined Space: A Case Study of Methane Oxidation by Fe/ZSM-5 Zeolite. *ACS Catal.* **9**, 9276–9284 (2019).

CHAPTER 4

HYDROFORMYLATION STUDIES ON CURHBTC AND RHBTC METAL-

ORGANIC FRAMEWORK

4.1. INTRODUCTION

The ability to tailor active sites for specific reactions has long been a goal for the rational design of superior heterogeneous catalysts. For conventional heterogeneous catalysts consisting of supported metal particles, it is impossible to completely control changes in the active sites due to particle sintering,[1,2] as well as changes in surface structure and composition during exposure to reaction conditions at elevated temperatures and pressures.[3–5] The use of metal-organic frameworks (MOFs) as heterogeneous catalysts presents the unique opportunity to systematically modify the geometries, ensemble sizes, and compositions of highly dispersed active sites. MOFs are a new class of hybrid inorganic/organic materials that are highly crystalline, with structures consisting of metal nodes of specific geometries connected by organic linkers. For example, the structure of the well-studied $Cu_3(BTC)_2$ (BTC^{3-} = benzene-1,3,5-tricarboxylate, abbreviated as CuBTC), also known as HKUST-1, in which the M^{2+} ions are arranged in a paddle-wheel configuration ($M_2(O_2C-)_4$).[6] The high porosity of the MOFs ensures a sufficient number of active sites for catalytic reactions (600–6000 m^2/g surface area), and it is also possible to adjust the pore sizes and distance between metal nodes through the choice of the organic linker.

The highly dispersed nature of the active metal sites in MOFs presents the possibility of controlling selectivity through catalysis at single isolated sites. Recent studies in the literature have demonstrated that single-site catalysts have different properties compared to catalysts with larger ensembles, and this unique behavior can be used to alter both activity and selectivity of the reaction.[7–12] For example, work by the Sykes group has shown for hydrogenation reactions, single atoms of Pd isolated in a

Cu(111) surface retain high activity for H_2 dissociation but also improve hydrocarbon desorption, thus facilitating hydrogenation of alkenes.[3,13] Small, isolated ensembles of metal atoms are ideal for hydrogenation reactions because larger ensembles catalyze undesired side reactions such as coking and hydrogenolysis.[14–16] Moreover, recent studies have reported that supported single-site metal atoms or ions have excellent activities and selectivities for a number of different reactions, including hydroformylation[17], hydrogenation,[18–20], and water-gas shift.[20–22]

Bimetallic MOFs provide a well-controlled platform for understanding how multifunctional active sites can be systematically introduced into the MOF structure. Bimetallic surfaces have shown great promise for the development of new catalytic systems, given that bimetallics are known to exhibit properties that are distinctly different from the single metal constituents.[23–26] Specifically the presence of the second metal can provide different activity than the first metal resulting in a bifunctional catalyst.[27–31] Furthermore, the ensemble of active sites may be altered by the addition of a second metal,[32,33], or electronic interactions between two metals can also give rise to different chemical activities and selectivities.[34–42] For the conventional supported metal particle catalysts, it can be difficult to separate the combined effects of electronic interactions and changes in ensemble size. In contrast, for MOFs, the monometallic and bimetallic frameworks can be isostructural, and therefore the effects of adding a second metal can be decoupled from geometric changes.

Gas-phase catalysis has a significant economic advantage over solution-phase catalysis, given that separation processes are not necessary to isolate the catalyst from the products in gas phase reactions. Although MOFs are reported to be excellent catalysts

57

for a number of reactions in the liquid phase, including hydrogenation, oxidation, and epoxidation of alkenes,[43–49] there have been few studies of gas-phase catalysis with MOFs. Furthermore, there have been no previous reports of gas-phase catalysis on bimetallic MOFs in which both metals play a distinct and critical role in the reaction. Our work on gas-phase hydrogenation of propylene to propane on the $Cu_{3-x}Rh_x(BTC)_2$ MOF
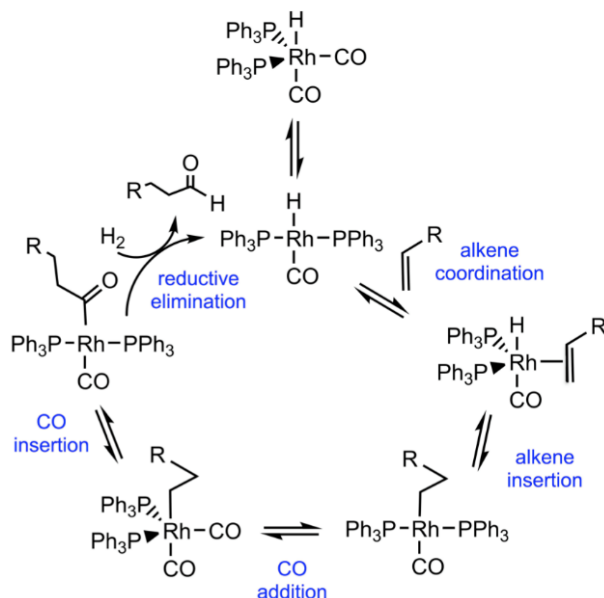
Figure 4.1. Mechanism for alkene hydroformylation with Wilkinson's catalyst. Adapted from reference 57.

(abbreviated CuRhBTC) was the first to report gas-phase catalytic activity at nodes of a crystalline MOF.[50] Other studies have demonstrated activity in the gas phase on MOF frameworks; however, the active sites were species selectively deposited at the metal nodes,[51–53] which makes these systems synthetically more challenging to prepare and difficult to control in terms of oxidations states, nucleation sites, and sintering. In other cases, metal particles have been deposited in the MOF pores,[54,55] but these catalysts still suffer from the lack of control over the geometry and composition of the active sites, as also observed with conventional supported metal particles catalysts.

58

The hydroformylation reaction is the preferred industrial route for the synthesis of aldehydes from CO, H_2, and alkenes,[56–58] and is also the most widely used reaction in homogeneous catalysis.[59,60] Conversion of alkenes from natural gas into aldehydes using readily available syngas (CO, H_2) is an attractive process, given that the global production of aldehydes is over 10 million tons/year.[56,61] Aldehydes are intermediates in the synthesis of bulk chemicals such as alcohols, esters, and carboxylic acids, and also have direct applications in the pharmaceutical and perfume industries, agrochemicals, flavorings, and food additives.[56,59,62]The mechanism for homogenous hydroformylation is shown in Figure 4.1. The first step is alkene adsorption accompanied by dissociation of H_2, and the second step involves the insertion of CO into the alkyl intermediate to form an acyl species. Hydrogenation of the acyl intermediate then produces the aldehyde. Although several transition metals have activity for hydroformylation, Rh and Co are preferred catalysts for industrial hydroformylation reactions.[59] The disadvantage of homogeneous reactions is the cost of separating the catalyst from the products, and therefore hydroformylation via heterogeneous catalysis has distinct economic benefits.[63] Furthermore, high pressures of reactant gases (80–100 atm), particularly H_2, are required for homogeneous hydroformylation.[57] In contrast, heterogeneous hydroformylation on supported Rh ions[64–66] or metal particles can be carried out at pressures $\leq$ 1 atm and moderate temperatures of ~150 °C.[64,65] The disadvantage of the heterogeneous catalysts consisting of supported Rh particles or Rh ions is the lower selectivities for aldehydes over alkanes[64,67] compared to homogeneous catalysts, in which selectivities often exceed 90%.[56,62] However, recent studies of single-atom Rh catalysts supported on ZnO reported activity and selectivity comparable to the homogenous catalysts, which have selectivities

of 99%.[56] Rh single-atom catalysts on CoO also exhibit excellent selectivity toward the aldehyde (94%) as well as high activities (TON = 2065/hr).[62] CuRhBTC was identified as a potential catalyst with dispersed Rh ions at the MOF nodes that would possess the high activity for hydroformylation exhibited by supported metal ions, as well as excellent selectivity to aldehydes reported for the single-site catalysts. Ethylene hydroformylation was chosen as the probe reaction since it is a simple alkene and the rate of hydroformylation of ethylene is higher compared to larger alkenes.

In the work reported here, the CuRhBTC MOF has shown activity for catalytic hydroformylation of ethylene to the desired product propanal although some ethane is also formed in the reaction. Other Rh-based catalysts such as RhBTC, Rh^0, Rh^{3+}, and Rh^{2+} on SiO_2 and the Rh-Y zeolite were studied under the same reaction conditions for comparison. Furthermore, other bimetallic CuMBTC (M=Co, Ru) MOFs were also investigated.

4.2. EXPERIMENTAL METHODS

Sample preparation before analysis

All the MOF samples for this study were dried in air or in N_2 flow for 90 mins at room temperature to drive out the solvents such as ethanol or methanol before the catalytic evaluation, X-ray photoelectron spectroscopy (XPS), and powder x-ray diffraction (PXRD) experiments. The Rh^{3+}/SiO_2 was synthesized by incipient wetness impregnation or dry impregnation method. The pore volume Aerosil 300 silica with a specific surface area of 300 ± 30 m^2/g from Evonik was measured experimentally using deionized water (2.3605 cm^3/g, DI H_2O, 18.1 MΩ.cm). The aqueous solution was prepared by dissolving 26.4 mg of $RhCl_3.3H_2O$ (Engelhard and Oakwood Chemicals) in

1800 μls of DI H_2O which was then added to 1000mg of silica to prepare a 1.1 % Rh^{3+}/SiO_2 catalyst. The wt.% loading of the catalyst was determined by an ICP-AAS (inductively coupled plasma- atomic absorption spectroscopy) analysis of the impregnating solution. The sample was then dried in a He environment for 24 hrs and stored in a closed vial. The 1.51% Rh^{2+}/SiO_2 was prepared by the method described elsewhere[68] using the $Rh_2(OAc)_4$(Strem Chemicals Inc.) precursor and Aerosil 300 silica (Evonik, specific surface area=300 ± 30 m^2/g) support. A 21.5mg of $Rh_2(OAc)_4$ precursor and 500mg of silica were slurried in dried and deoxygenated n-pentane (Fisher, 99%) at room temperature, the solvent was removed by evacuation for a day, leaving all the rhodium on the support. The mass fraction of Rh^{2+}in the Rh^{2+}/SiO_2 sample was determined by dissolving Rh^{2+} in freshly prepared aqua regia (HCl:HNO_3 = 3:1) and analyzing the solution by ICP-AAS.[68] The Rh-Y zeolite was prepared by the process adapted from literature.[65]

Ethylene hydroformylation catalysis

All the catalysts for this work were evaluated in a 0.19" ID stainless steel (316 stainless steel) packed bed, tubular flow reactor.[69] The lower temperatures (20°C-80°C) of the reactor was maintained by using a jacketed shell connected to a recirculation bath circulating coolant mixture of glycol/H_2O and the higher temperatures(100°C -200°C) was achieved by using heating tape wrapped around the reactor body controlled by homebuilt PID controller. The temperature of the reactor was monitored by using a thermocouple inserted in the catalyst bed. The reactor pressure was maintained using a back-pressure regulator from Parker (part number: ABP1ST52BP4) that can hold pressure up to 500 psi. The feed composition during the experiment was maintained by

Brooks 5850E series mass flow controllers. The appropriate conditions of temperature,

pressure, feed gas composition were chosen to optimize activity and selectivity for

propanal while minimizing MOF decomposition. A typical feed gas composition for

ethylene hydroformylation was C_2H_4:H_2:CO=22:22:2 with a total flow rate of 46 sccm.

Before the evaluation, MOF catalysts were dried in air or in N_2 flow for 90 mins to

remove the majority of the ethanol/methanol from the MOF samples. The standard 2%

Rh/SiO_2 was reduced at 300°C for 2 hrs in 100% H_2(100sccm) prior to the

hydroformylation. The reactor effluent stream containing unreacted reactant and products

was sampled and analyzed by a Hewlett-Packard 5890 Series II chromatograph equipped

with an HP-PLOT/Q (30 m× 0.32mm×20μm) capillary column using a flame ionization

detector(FID) and the GC signal were calibrated using proper standards. All the transfer

lines and online gas chromatograph(GC) were heated to ~100°C using heating tapes. The

rates of product formation(μmoles/g metal-sec) were calculated using the metal weight

loading obtained from ICP measurements.

X-ray Photoelectron Spectroscopy (XPS)

Metal oxidation states in the MOFs were characterized by XPS before and after

exposure to hydrogenation and hydroformylation conditions, as well as before and after

incorporation of the second metal. XPS studies on the MOF powders were conducted at

UofSC's XPS facility using a Kratos AXIS Ultra XPS system. This instrument is

equipped with a monochromatic X-ray source and multichannel hemispherical analyzer

capable of high-energy resolution (0.5 eV).[6] A charge neutralization system allowed XPS

experiments to be conducted on the insulating MOF powders. Since a charge neutralizer

was used to prevent sample charging, binding energies for all samples were corrected by

setting the position of the adventitious carbon peak to 284.8 eV. Furthermore, a catalysis

cell directly attached to the XPS chamber allowed the sample to be treated at a high

temperature (80 °C) in H_2/CO at 3 atm, and samples were transferred from the catalysis

cell to the XPS chamber without exposure to air. The air-dried MOF samples were

evacuated in the load lock chamber overnight before introduction into the main vacuum

chamber for XPS. This sample was then transferred to a catalysis chamber and exposed

to hydroformylation feed composed of ethylene, H_2, and CO, and the total pressure and

temperature of the catalysis cell were maintained at 3 atm at 80°C respectively for 24

hours. The sample was then transferred back to the vacuum chamber for XPS

measurement where the Rh(3d) region was collected first to minimize possible reduction

due to X-ray exposure. The curve fitting analysis for XPS spectra was performed using

CasaXPS software using a combination of Gaussian and Lorentzian line shapes and a

Shirley baseline. After the XPS experiment, the samples were also analyzed with PXRD

to investigate changes in the crystallinity of the MOF.

4.3. RESULTS AND DISCUSSION

Based on the activity of Rh sites for alkene hydrogenation[69] and known activity

for Rh ions for hydroformylation[64–66], CuRhBTC was studied as a potential MOF catalyst

for ethylene hydrogenation reaction. CuRhBTC with different concentrations 25% Rh

[CuRh(25)BTC] and 36% Rh [CuRh(36)BTC] was studied in addition to monometallic

RhBTC and CuBTC MOFs. It should be noted that the RhBTC is much less crystalline

compared to CuRhBTC based on the PXRD pattern. Other bimetallic CuMBTC MOFs

(M= Co, Ru) were also investigated. A commercial 2% Rh/SiO_2, (Engelhard), 1.1 %

Rh^{3+}/SiO_2 prepared by wet impregnation, 1.5% Rh^{2+}/SiO_2[68], 1.9% Rh-Y zeolite[64] were
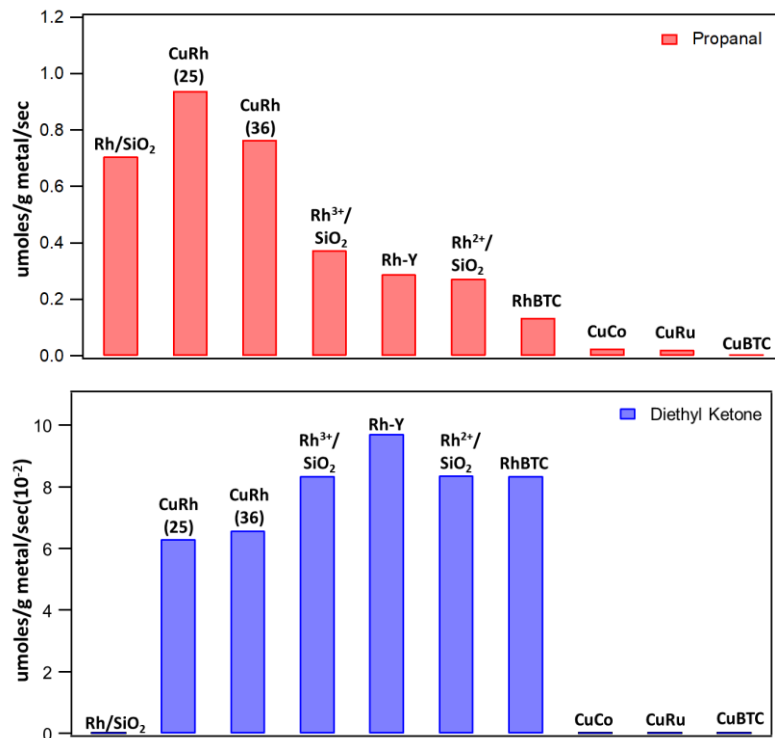
Figure 4.2. Hydroformylation yields for various catalysts: propanal(top); and diethyl ketone(bottom) production.

also investigated for hydroformylation reaction as standard catalysts. The CuRhBTC and

RhBTC MOFs exhibited activity for the catalytic hydroformylation of ethylene to
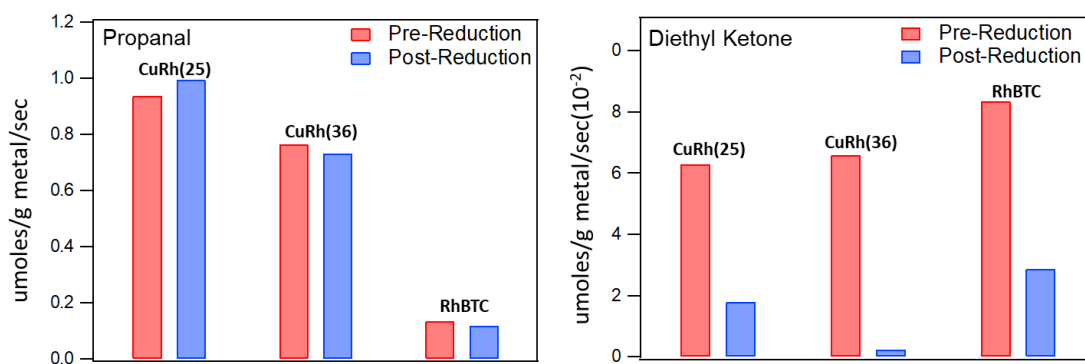
Figure 4.3. Hydroformylation yields: propanal(left) and diethyl ketone(right) comparison for various Rh-containing MOFs after reduction. *Reduction: Under hydroformylation feed: 22 SCCM C_2H_4+ 22 SCCM H_2+2 SCCM CO, at 80°C and 9 atm.
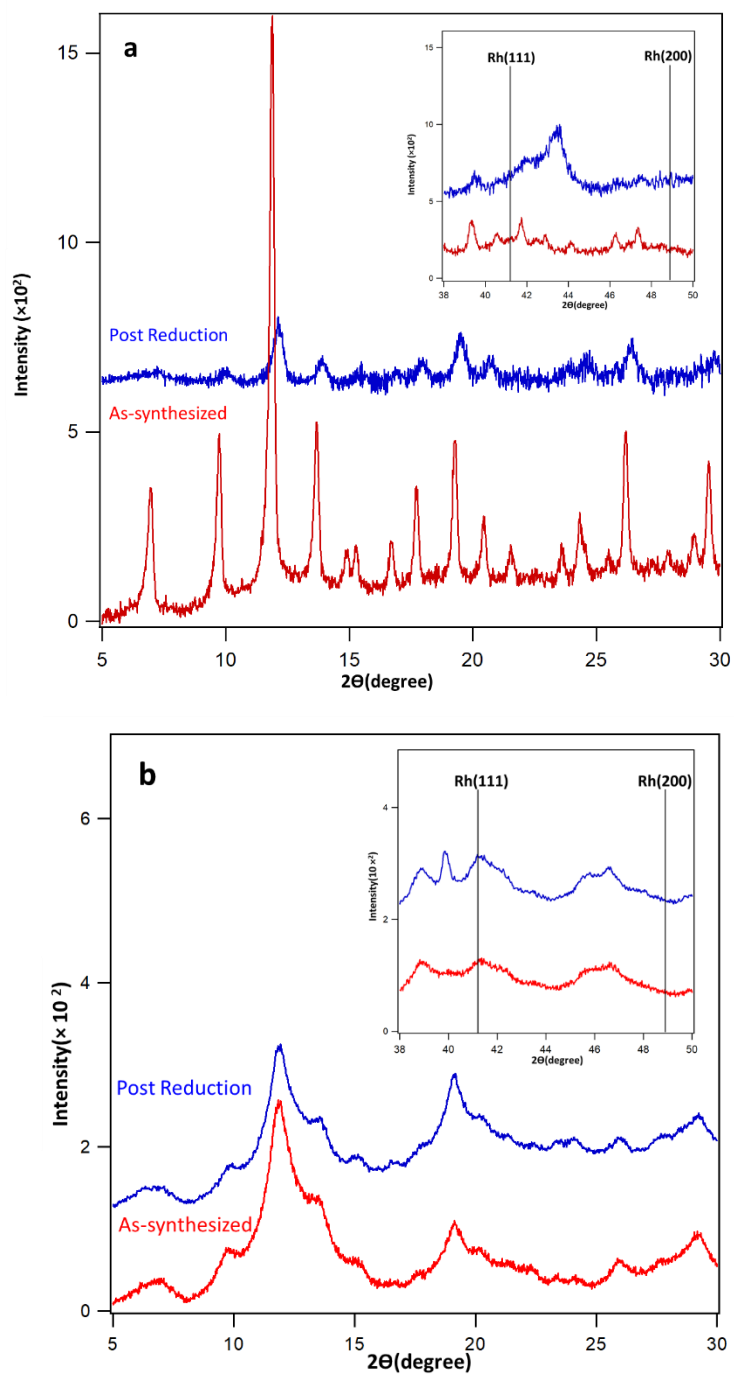
Figure 4.4. PXRD spectra of as-synthesized(red) and post-reduction a) CuRhBTC, b) RhBTC. *Reduction: Under hydroformylation feed: 22 SCCM C_2H_4+ 22 SCCM H_2+2 SCCM CO, at 80°C and 9 atm.

propanal. In contrast to the activity observed for the Rh-containing MBTCs MOFs, pure

CuBTC, CuRuBTC, and CuCoBTC had no hydroformylation activity and did not

produce significant quantities of propanal above the baseline activity under these reaction conditions. Figure 4.2 shows the average rate of propanal formation (umol/g metal/min) over a period of 24 hours at a reaction temperature of 80 °C and 3 atm of pressure with a feed of 22:22:2 sccm (ethylene:H_2:CO). The propanal yields were comparable for the two CuRhBTCs, but propanal formation was surprisingly lower on pure RhBTC. Diethyl
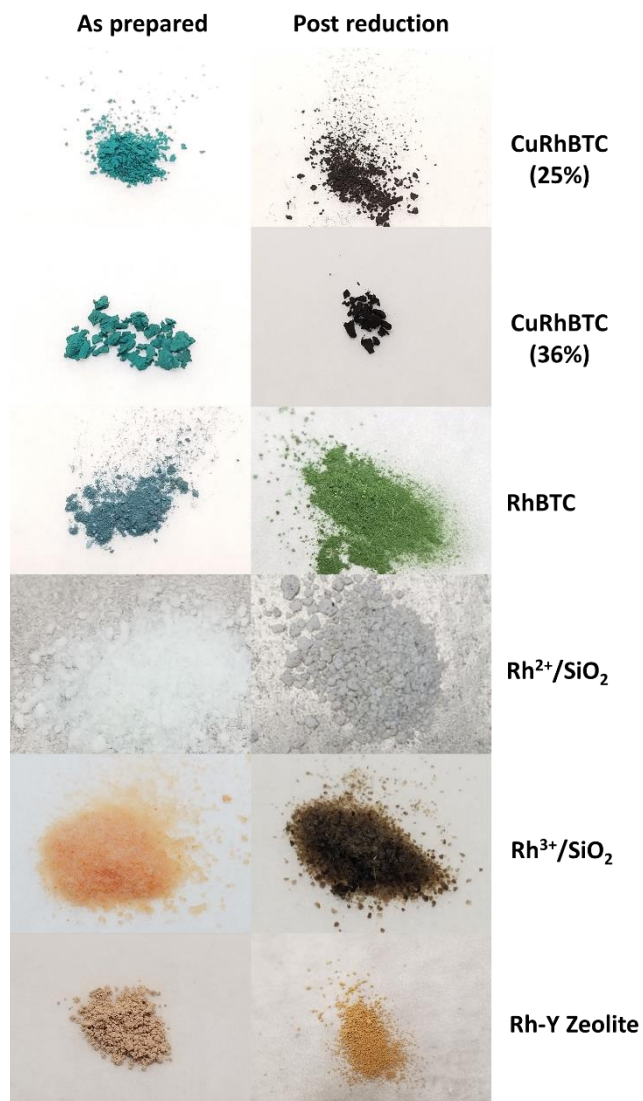
Figure 4.5. Images of as-prepared samples (left) and after reduction(right).

ketone was also observed as a reaction product on the Rh-containing MOFs (Figure 4.2). The production of diethyl ketone increased with Rh concentration, suggesting that a pair

of neighboring Rh sites may be necessary to form this coupling product. However, the

formation of diethyl ketone decreased substantially once the Rh-containing MOFs were

reduced to metallic Rh as shown in Figure 4.3. These Rh-containing MOFs: RhBTC,

CuRh(25)BTC, and CuRh(36)BTC were intentionally reduced to metallic Rh under

hydroformylation reaction condition at 80°C and 9 atm pressure and was confirmed by

changes in their color (Figure 4.5) of the samples and PXRD patterns where broad peaks

corresponding to metallic Rh(111) and Rh(200) start to appear as shown in Figure 4.4 .

Hydrogenation to ethane was a competing reaction pathway with a selectivity of ~50%

on CuRhBTC. For the metallic Rh/SiO$_2$, only propanal was observed as a product with no
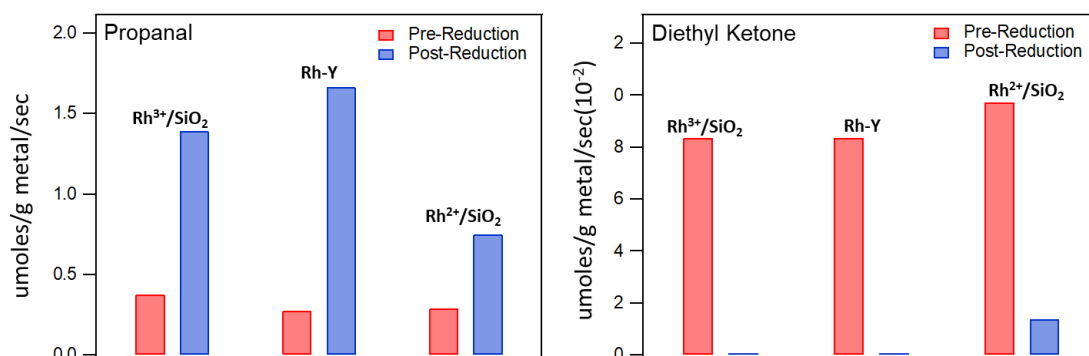
Figure 4.6. Hydroformylation yields: Propanal(left) and Diethyl ketone(right)
comparison for various Rh catalysts after reduction. *Reduction: Rh^{3+}, Rh^{2+}/
SiO$_2$, under hydrogenation feed: 22 SCCM C$_2$H$_4$+ 22 SCCM H$_2$, at 50°C and
80°C, Rh-Y zeolite, under hydroformylation feed: 22 SCCM C$_2$H$_4$+ 22 SCCM
H$_2$+2 SCCM CO, at 150°C and 3 atm.

diethyl ketone or ethane formation (Figure 4.2). The rate of propanal formation for

commercial 2% Rh/SiO$_2$ was observed to be 0.74 ± 0.04 μmoles/g Rh/sec which was

comparable to what we have observed for Rh-containing MOFs. The Rh-Y zeolite,

which was prepared from Rh^{3+} exchange into a Na-Y zeolite, produced both propanal and

diethyl ketone as well as ethane. Similarly, the Rh^{3+}/SiO$_2$ and Rh^{2+}/ SiO$_2$ catalyst formed

propanal, diethyl ketone, and ethane in low yields (Figure 4.2), but the rate of propanal

formation increased after reduction to metallic Rh (Figure 4.6). Here the Rh^{2+}/SiO_2 and

Rh^{3+}/SiO_2 samples were intentionally reduced by subjecting them to hydrogenation

conditions at 80°C and 50°C (Feed, C_2H_4:H_2=22:22) respectively as described in our

previous work.[50] Similarly, Rh-Y zeolite was reduced under hydroformylation conditions

at 150°C and 3 atm pressure. In all cases, the rate of propanal production was much lower

than on the Rh-MOFs; while these catalysts have lower weight loadings of Rh compared

to CuRhBTC and RhBTC.

Metal oxidation states in the MOFs were characterized by XPS before and after

exposure to hydroformylation conditions, as well as before and after incorporation of the

second metal. Our earlier X-ray photoelectron spectroscopy studies[69] on CuRhBTC

showed the oxidation state of the Rh ion in the CuRhBTC was 2+ with $Rh(3d_{5/2})$ peak
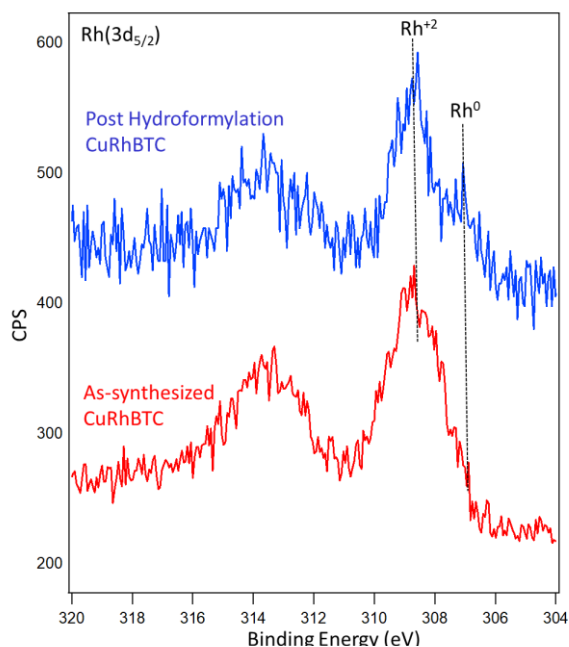
Figure 4.7. XPS spectra of the Rh(3d) region for as-synthesized CuRhBTC(after evacuation) and after ethylene hydroformylation at 80°C and 3 atm pressure.

appearing at binding energy 309.2 eV consistent with Rh^{2+} in standard $Rh_2(OAc)_4$ with a
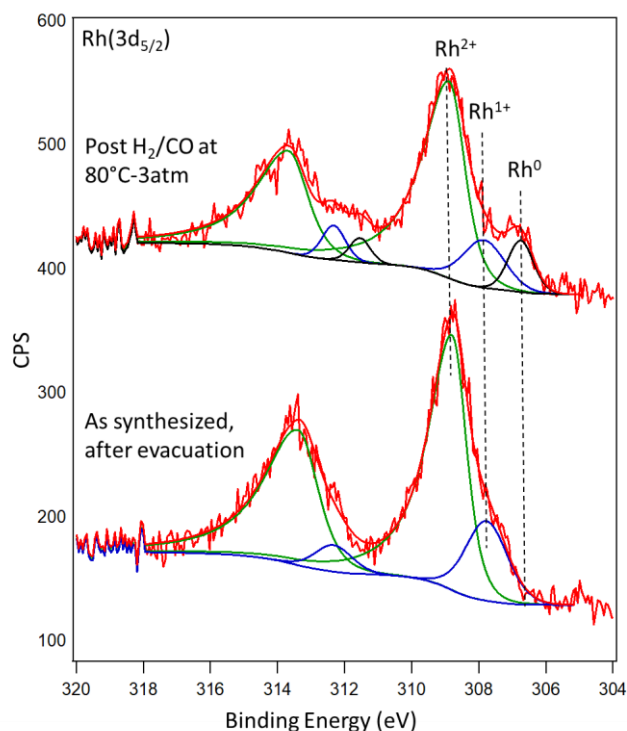
Figure 4.8. Pseudo in-situ X-ray photoelectron spectroscopy data for the Rh(3d) region for as- synthesized CuRhBTC after evacuation (bottom), after CO/H$_2$ at 80°C and 3 atm for 24 hrs in catalysis cell without exposure to atmosphere (top, ex-situ XPS)

peak at 308.9 eV. The X-ray Absorption Near-Edge Structure (XANES) studies provide

further evidence of the assignment of Rh^{2+} oxidation state in the CuRhBTC since the Rh

K-edge is nearly identical for CuRhBTC and the $Rh_2(OAc)_4$ which has the Rh in

oxidation state 2+. [50] Furthermore, there is no evidence of metallic Rh at 307.0- 307.4 eV

in the pre-reaction CuRhBTC spectrum. However, post-reaction XPS analysis of the

CuRhBTC catalyst shows the presence of metallic Rh. A metallic Rh peak with a binding

energy ~307eV appeared along with the Rh^{2+} species at 309 eV (Figure 4.7) during the

ex-situ XPS investigation of a post-reaction CuRhBTC catalyst transferred from the

69

reactor to the XPS chamber in air. Another XPS experiment was carried out in which the air-dried CuRhBTC was exposed to H_2/CO at 80 C and 3 atm in a gas cell attached to the UHV chamber, and XPS was carried out without exposure to air (Figure 4.8). The pre-reaction Rh(3d) spectrum showed peaks: the main feature at 308.8 eV from Rh2+ and a smaller feature at 307.9 eV from Rh^{1+}; the Rh^{1+} oxidation state has also been observed in RhBTC by Fischer and coworkers and was attributed to defects in the structure.[70,71]After the treatment in the gas cell, a metallic Rh feature with at 306.8 eV was observed, which is consistent with the ex-situ XPS result for post-reaction CuRhBTC.

Powder X-ray diffraction (PXRD) investigations were carried out on MOF samples before and after hydroformylation reaction to address the changes in crystallinity of the MOF and changes in Rh oxidation state during a reaction. The PXRD collected on
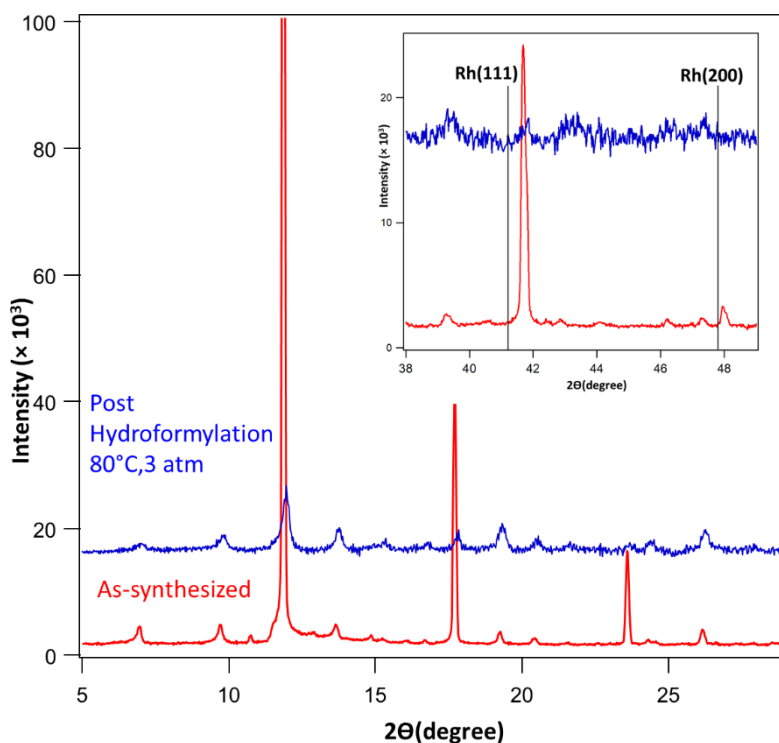
Figure 4.9. PXRD pattern of CuRhBTC before and after hydroformylation at 3 atm pressure and at 80°C.

the CuRhBTC after the hydroformylation at 3 atm and 80°C showed slight changes in the peak pattern which is indicative of the MOF decomposition and onset of metallic Rh formation at 3 atm and 80°C under reaction conditions (Figure 4.9). However, after exposure to a more reducing condition of 9 atm of feed gas pressure at 80°C, the post-reaction PXRD of RhBTC and CuRhBTC showed reduced metallic Rh (Figure 4.5), that led to increased propanal production, but decreased diethyl ketone formation at 80C and 3atm (Figure 4.6).

These studies show that CuRhBTC and RhBTC catalyzes hydroformylation of ethylene to propanal and diethyl ketone, but there are several challenges in using these MOFs as hydroformylation catalysts. The highly reducing conditions required for hydroformylation will convert the metal nodes to metallic species at elevated temperatures and pressures, and therefore reaction temperatures should be kept below 100°C; at these temperatures, the activity is lower and poisoning by CO is a significant problem. The Rh^{2+} oxidation state in the CuRhBTC is not known for hydroformylation activity, which is facilitated by the cycling between Rh^{3+} and Rh^{1+} in homogeneous catalysts. Since hydroformylation requires three sites for alkene, CO, and hydrogen adsorption, the paddle-wheel node geometry in MBTC systems is not ideal, given that each metal ion has only one open adsorption site; it should be noted that hydroformylation might still be possible because a neighboring open site is provided in the dimer paddle-wheel configuration and dissociation of a metal-oxygen bond could provide another open site, as proposed in the hydrogenation mechanism at the paddle-wheel node in our previous studies.

4.4. CONCLUSION

Based on the known activity of Rh sites for alkene hydrogenation and hydroformylation, CuRhBTC was identified as a potential catalyst for hydroformylation reaction with ethylene as a probe molecule. Ethylene hydroformylation was also studied on several other catalysts including monometallic CuBTC, RhBTC, bimetallic CuCoBTC, CuRuBTC, Rh-Y zeolite, Rh^{3+}, Rh^{2+} and Rh^0/SiO$_2$. The CuBTC, CuCoBTC, and CuRuBTC did not show any activity for ethylene hydroformylation, whereas the Rh-containing MOFs: CuRhBTC, RhBTC along with Rh^{3+} containing Rh-Y zeolite, Rh^{2+}, and Rh^{3+}/SiO$_2$ prepared by incipient wetness impregnation exhibited catalytic hydroformylation of ethylene to propanal. Diethyl ketone was also observed as a reaction product for Rh-containing catalysts, such as Rh^{3+}/SiO$_2$, Rh^{2+}/SiO$_2$, Rh-Y zeolite including Rh-containing MOFs suggesting Rh-ions in CuRhBTC and RhBTC could be active for ethylene hydroformylation producing propanal and diethyl ketone. The increased production of diethyl ketone with Rh concentration suggests that a pair of neighboring Rh sites could facilitate the formation of this coupling product. The formation of some metallic Rh particles in CuRhBTC and RhBTC, confirmed by XPS, suggests that some of the metal nodes get reduced under hydroformylation conditions.

their collaboration in MOF synthesis and characterization. Thank you to Prof. John Monnier and Dr. Greg Tate for their help in synthesizing Rh catalysts and ICP measurements. We also acknowledge the UofSC's XPS user facility and Dr. Stavros Karakolos for his contribution at the facility.

4.5. REFERENCES:

1. Henry, C. R. Surface studies of supported model catalysts. *Surf. Sci. Rep.* **31**, 231–325 (1998).

2. Campbell, C. T. Ultrathin metal films and particles on oxide surfaces: structural, electronic and chemisorptive properties. *Surf. Sci. Rep.* **27**, 1–111 (1997).

3. Kyriakou, G. *et al.* Isolated metal atom geometries as a strategy for selective heterogeneous hydrogenations. *Science* **335**, 1209–1212 (2012).

4. Feng, T. *et al.* Reaction-Driven Restructuring of Rh-Pd and Pt-Pd Core-Shell Nanoparticles. *Science (80-.).* **322**, 932–934 (2008).

5. Nerlov, J., Sckerl, S., Wambach, J. & Chorkendorff, I. Methanol synthesis from CO2, CO and H2 over Cu(100) and Cu(100) modified by Ni and Co. *Appl. Catal. A Gen.* **191**, 97–109 (2000).

6. Duke, A. S. *et al.* Active Sites in Copper-Based Metal-Organic Frameworks: Understanding Substrate Dynamics, Redox Processes, and Valence-Band Structure. *J. Phys. Chem. C* **119**, 27457–27466 (2015).

7. Grazia, M. *et al.* Identification of single-site gold catalysis in acetylene hydrochlorination. *Science (80-.).* **355**, 1399–1403 (2017).

8. Liu, L. & Corma, A. Metal Catalysts for Heterogeneous Catalysis: From Single Atoms to Nanoclusters and Nanoparticles. *Chem. Rev.* **118**, 4981–5079 (2018).

9. Qiao, B. *et al.* Single-atom catalysis of CO oxidation using Pt1/FeOx. *Nat. Chem.* **3**, 634–641 (2011).

10. Zhou, Y. *et al.* Dual-Metal Interbonding as the Chemical Facilitator for Single-Atom Dispersions. *Adv. Mater.* **32**, 2003484 (2020).

11. Wang, A., Li, J. & Zhang, T. Heterogeneous single-atom catalysis. *Nat. Rev. Chem.* **2**, 65–81 (2018).

12. Giannakakis, G., Flytzani-Stephanopoulos, M. & Sykes, E. C. H. Single-Atom Alloys as a Reductionist Approach to the Rational Design of Heterogeneous Catalysts. *Acc. Chem. Res.* **52**, 237–247 (2019).

13. Kyriakou, G. *et al.* Heterogeneous Hydrogenations. **335**, 1209–1213 (2012).

14. Réocreux, R. *et al.* Controlling Hydrocarbon (De)Hydrogenation Pathways with Bifunctional PtCu Single-Atom Alloys. *J. Phys. Chem. Lett.* **11**, 8751–8757 (2020).

15. Marcinkowski, M. D. *et al.* Pt/Cu single-atom alloys as coke-resistant catalysts for efficient C–H activation. *Nat. Chem.* **10**, 325–332 (2018).

16. Kesmodel, L. L., Dubois, L. H. & Somorjai, G. A. LEED analysis of acetylene and ethylene chemisorption on the Pt(111) surface: Evidence for ethylidyne formation. *J. Chem. Phys.* **70**, 2180–2188 (1979).

17. Amsler, J. *et al.* Prospects of Heterogeneous Hydroformylation with Supported Single Atom Catalysts. *J. Am. Chem. Soc.* **142**, 5087–5096 (2020).

18. Babucci, M. *et al.* Tuning the Selectivity of Single-Site Supported Metal Catalysts with Ionic Liquids. *ACS Catal.* **7**, 6969–6972 (2017).

19. Yang, X.-F. *et al.* Single-Atom Catalysts: A New Frontier in Heterogeneous Catalysis. *Acc. Chem. Res.* **46**, 1740–1748 (2013).

20. Serna, P. & Gates, B. C. Molecular metal catalysts on supports: organometallic chemistry meets surface science. *Acc. Chem. Res.* **47**, 2612–2620 (2014).

21. Chen, Y. *et al.* Single-Atom Catalysts: Synthetic Strategies and Electrochemical Applications. *Joule* **2**, 1242–1264 (2018).

22. Flytzani-Stephanopoulos, M. Gold atoms stabilized on various supports catalyze the water-gas shift reaction. *Acc. Chem. Res.* **47**, 783–792 (2014).

23. Sinfelt, J. H. Catalysis by alloys and bimetallic clusters. *Preprints* **21**, 350–352 (1976).

24. Chen, J. G., Menning, C. A. & Zellner, M. B. Monolayer bimetallic surfaces: Experimental and theoretical studies of trends in electronic and chemical properties. *Surf. Sci. Rep.* **63**, 201–254 (2008).

25. Rodriguez, J. Physical and chemical properties of bimetallic surfaces. *Surf. Sci. Rep.* **24**, 223–287 (1996).

26. Campbell, C. T. Bimetallic Surface Chemistry. *Annu. Rev. Phys. Chem.* **41**, 775–837 (1990).

27. Gasteiger, H. A., Markovic, N., Ross, P. N. & Cairns, E. J. Methanol electrooxidation on well-characterized platinum-ruthenium bulk alloys. *J. Phys. Chem.* **97**, 12020–12029 (1993).

28. Wasmus, S. & Küver, A. Methanol oxidation and direct methanol fuel cells: a selective review1In honour of Professor W. Vielstich on the occasion of his 75th birthday and in appreciation of his contributions to electrochemistry as well as fuel cell development.1. *J. Electroanal. Chem.* **461**, 14–31 (1999).

29. Kabbabi, A. *et al.* In situ FTIRS study of the electrocatalytic oxidation of carbon monoxide and methanol at platinum–ruthenium bulk alloy electrodes. *J. Electroanal. Chem.* **444**, 41–53 (1998).

30. Granger, P., Lecomte, J. J., Dathy, C., Leclercq, L. & Leclercq, G. Kinetics of the CO+NO Reaction over Rhodium and Platinum–Rhodium on Alumina: II. Effect of Rh Incorporation to Pt. *J. Catal.* **175**, 194–203 (1998).

31. Park, J. B., Ratliff, J. S., Ma, S. & Chen, D. A. Understanding the Reactivity of Oxide-Supported Bimetallic Clusters: Reaction of NO with CO on TiO2(110)-Supported Pt−Rh Clusters. *J. Phys. Chem. C* **111**, 2165–2176 (2007).

32. Mingshu, C., Dheeraj, K., Cheol-Woo, Y. & Wayne, G. D. The Promotional Effect of Gold in Catalysis by Palladium-Gold. *Science (80-.).* **310**, 291–293 (2005).

33. Molenbroek, A. M., Nørskov, J. K. & Clausen, B. S. Structure and Reactivity of Ni−Au Nanoparticle Catalysts. *J. Phys. Chem. B* **105**, 5450–5458 (2001).

34. Rodriguez, J. A. & Goodman, D. W. The nature of the metal-metal bond in bimetallic surfaces. *Science (80-.).* **257**, 897–903 (1992).

35. Kołodziej, J. J. *et al.* Ultrathin metals films on W(221): Structure, electronic properties and reactivity. *Prog. Surf. Sci.* **59**, 117–134 (1998).

36. Rodriguez, J. A. & Goodman, D. W. Surface science studies of the electronic and chemical properties of bimetallic systems. *J. Phys. Chem.* **95**, 4196–4206 (1991).

37. Watwe, R. M., Cortright, R. D., Mavrikakis, M., Nørskov, J. K. & Dumesic, J. A. Density functional theory studies of the adsorption of ethylene and oxygen on Pt(111) and Pt3Sn(111). *J. Chem. Phys.* **114**, 4663–4668 (2001).

38. Zhou, W. P. *et al.* Improving electrocatalysts for O2 reduction by fine-tuning the Pt-support interaction: Pt monolayer on the surfaces of a Pd3Fe(111) single-crystal alloy. *J. Am. Chem. Soc.* **131**, 12755–12762 (2009).

39. Kitchin, J. R., Nørskov, J. K., Barteau, M. A. & Chen, J. G. Role of strain and ligand effects in the modification of the electronic and chemical Properties of bimetallic surfaces. *Phys. Rev. Lett.* **93**, (2004).

40. Kitchin, J. R., Nørskov, J. K., Barteau, M. A. & Chen, J. G. Modification of the surface electronic and chemical properties of Pt(111) by subsurface 3d transition metals. *J. Chem. Phys.* **120**, 10240–10246 (2004).

41. Schlapka, A., Lischka, M., Groß, A., Käsberger, U. & Jakob, P. Surface strain versus substrate interaction in heteroepitaxial metal layers: Pt on Ru(0001). *Phys. Rev. Lett.* **91**, 016101/1-016101/4 (2003).

42. Maroun, F., Ozanam, F., Magnussen, O. M. & Behm, R. J. The role of atomic ensembles in the reactivity of bimetallic electrocatalysts. *Science (80-.).* **293**, 1811–1814 (2001).

43. Kozachuk, O. *et al.* Multifunctional, defect-engineered metal-organic frameworks with ruthenium centers: Sorption and catalytic properties. *Angew. Chemie - Int. Ed.* **53**, 7058–7062 (2014).

44. Lee, J. *et al.* Metal-organic framework materials as catalysts. *Chem. Soc. Rev.* **38**, 1450–1459 (2009).

45. Beier, M. J. *et al.* Aerobic Epoxidation of Olefins Catalyzed by the Cobalt-Based Metal-Organic Framework STA-12(Co). *Chem. - Eur. J.* **18**, 887 (2012).

46. Furukawa, H., Cordova, K. E., O'Keeffe, M. & Yaghi, O. M. The chemistry and applications of metal-organic frameworks. *Science (80-.).* **341**, (2013).

47. Lalonde, M. *et al.* Transmetalation: Routes to metal exchange within metal-organic frameworks. *J. Mater. Chem. A* **1**, 5453–5468 (2013).

48. Chughtai, A. H., Ahmad, N., Younus, H. A., Laypkov, A. & Verpoort, F. Metal-Organic Frameworks: Versatile Heterogeneous Catalysts for Efficient Catalytic Organic Transformations. *Chem. Soc. Rev.* **44**, 6804 (2015).

49. Leus, K., Liu, Y. & Voort, P. Van Der. Metal-Organic Frameworks as Selective or Chiral Oxidation Catalysts Metal-Organic Frameworks as Selective or Chiral Oxidation. **4940**, (2017).

50. Shakya, D. M. *et al.* Selective Catalytic Chemistry at Rhodium(II) Nodes in Bimetallic Metal-Organic Frameworks. *Angew. Chem., Int. Ed.* **58**, 16533 (2019).

51. Li, Z. *et al.* Sintering-Resistant Single-Site Nickel Catalyst Supported by Metal-Organic Framework. *J. Am. Chem. Soc.* **138**, 1977–1982 (2016).

52. Liu, J. *et al.* Beyond the Active Site: Tuning the Activity and Selectivity of a Metal-Organic Framework-Supported Ni Catalyst for Ethylene Dimerization. *J. Am. Chem. Soc.* **140**, 11174 (2018).

53. Otake, K. I. *et al.* Single-Atom-Based Vanadium Oxide Catalysts Supported on Metal Organic Frameworks: Selective Alcohol Oxidation and Structure Activity Relationship. *J. Am. Chem. Soc.* **140**, 8652 (2018).

54. Drake, T., Ji, P. F. & Lin, W. B. Site Isolation in Metal-Organic Frameworks Enables Novel Transition Metal Catalysis. *Acc. Chem. Res.* **51**, 2129 (2018).

55. Zhao, M. *et al.* Metal-organic frameworks as selectivity regulators for hydrogenation reactions. *Nature* **539**, 76–80 (2016).

56. Lang, R. *et al.* Hydroformylation of Olefins by a Rhodium Single-Atom Catalyst with Activity Comparable to RhCl(PPh3)3. *Angew. Chemie - Int. Ed.* **55**, 16054–16058 (2016).

57. Kumar, M., Chaudhari, R. V., Subramaniam, B. & Jackson, T. A. Ligand effects on the regioselectivity of rhodium-catalyzed hydroformylation: Density functional calculations illuminate the role of long-range noncovalent interactions. *Organometallics* **33**, 4183–4191 (2014).

58. Jörke, A., Seidel-Morgenstern, A. & Hamel, C. Rhodium-BiPhePhos catalyzed hydroformylation studied by operando FTIR spectroscopy: Catalyst activation and rate determining step. *J. Mol. Catal. A Chem.* **426**, 10–14 (2017).

59. Vilches-herrera, M. & Domke, L. Isomerization − Hydroformylation Tandem Reactions. (2014).

60. Wu, X. F. *et al.* Transition-metal-catalyzed carbonylation reactions of olefins and alkynes: A personal account. *Acc. Chem. Res.* **47**, 1041–1053 (2014).

61. Hebrard, F. & Kalck, P. Cobalt-catalyzed hydroformylation of alkenes: Generation and recycling of the carbonyl species, and catalytic cycle. *Chem. Rev.* **109**, 4272–4282 (2009).

62. Wang, L. *et al.* Atomic-level insights in optimizing reaction paths for hydroformylation reaction over Rh/CoO single-atom catalyst. *Nat. Commun.* **7**, 14036 (2016).

63. Cole-Hamilton, D. J. Homogeneous catalysis - New approaches to catalyst separation, recovery, and recycling. *Science (80-.).* **299**, 1702–1706 (2003).

64. Arai, H. & Tominaga, H. Hydroformylation and hydrogenation of olefins over rhodium zeolite catalyst. *J. Catal.* **75**, 188–189 (1982).

65. Takahashi, N. & Kobayashi, M. Comparison of ethylene with propylene hydroformylation over a Rh-Y zeolite catalyst under atmospheric pressure. *J. Catal.* **85**, 89–97 (1984).

66. Kim, T. *et al.* Gas-phase hydroformylation of propene over silica-supported PPh 3-modified rhodium catalysts. *Top. Catal.* **54**, 299–307 (2011).

67. Takahashi, N., Matsuo, H. & Kobayashi, M. Kinetics and mechanism of ethylene hydroformylation over Rh-Y zeolite under atmospheric pressure. *J. Chem. Soc. Faraday Trans. 1 Phys. Chem. Condens. Phases* **80**, 629–634 (1984).

68. Yang, D., Xu, P., Guan, E., Browning, N. D. & Gates, B. C. Rhodium pair-sites on magnesium oxide: Synthesis, characterization, and catalysis of ethylene hydrogenation. *J. Catal.* **338**, 12–20 (2016).

69. Shakya, D. M. *et al.* Heterogeneous Catalysis Hot Paper Selective Catalytic Chemistry at Rhodium (II) Nodes in Bimetallic Metal – Organic Frameworks Angewandte. **29208**, 16533–16537 (2019).

70. Heinz, W. R. *et al.* Thermal Defect Engineering of Precious Group Metal-Organic Frameworks: A Case Study on Ru/Rh-HKUST-1 Analogues. *ACS Appl. Mater. Interfaces* **12**, 40635–40647 (2020).

71. Fischer, R. A. Dalton Transactions. **48**, (2019).

CHAPTER 5

PARTICLE SIZE EFFECT IN THE PROPYLENE HYDROGENATION OVER

CARBON-SUPPORTED PALLADIUM CATALYST PREPARED BY STRONG

ELECTROSTATIC ADSORPTION

5.1. INTRODUCTION

Palladium-catalyzed reactions are desirable for many industrial processes,[1] based on their atom economy, cost savings, and synthetic utility. Catalytic hydrogenation reactions[2–4] and cross-coupling reactions[5] are among the most widely used chemical transformations. Recently, the Gupton group has shown that microwaved Pd particles on graphene nanoplatelets have superior activity in the Suzuki cross-coupling reaction compared to Pd on conventional carbon supports and oxides.[6,7] To better understand the fundamental properties of Pd on carbon catalysts compared to oxide supports, propylene hydrogenation was chosen as a simple gas phase probe reaction. [6,8] The strong electrostatic adsorption (SEA) method has been used to generate high-quality solid-supported metal catalysts, including Pd, Cu, Co, Ru, Ni, and Pt on silica, Pt on activated carbon, carbon black, and graphitic carbon.[9,10] The Pd particles were deposited on a variety of supports using the strong electrostatic adsorption (SEA) method known to synthesize supported catalysts with small metal nanoparticles and excellent metal dispersion. Our recent results of propylene hydrogenation demonstrated that Pd particles deposited by SEA on various carbon supports such as carbon black(non-graphitic), and graphene nanoplatelets(graphitic) have higher activity than small, uniformly sized Pd particles on silica.

The activity of supported metal nanoparticle catalysts is largely dependent on the availability of surface sites to participate in the desired reaction. A range of important industrial processes uses supported catalysts, and their performance strongly hinges on the metal particle size, as in Co and Fe for Fisher-Tropsch synthesis[11–13], Pd, and Pt for various hydrogenation and oxidation reactions[14,15], and Ag for ethylene epoxidation[16]. The catalyst activity is often influenced by the size and structure of the metal particles

below ~20nm.[17] The various surface facets exhibit a changing fraction of different adsorption sites, such as edges, corners, steps, and kinks than terraces sites at flat surfaces in the crucial size range of 2- 10 nm.[11,14] Smaller particles, having a higher surface-to-volume ratio, have higher dispersion and more metal surface sites, which generally translates to higher activity per mass of metal.[10]
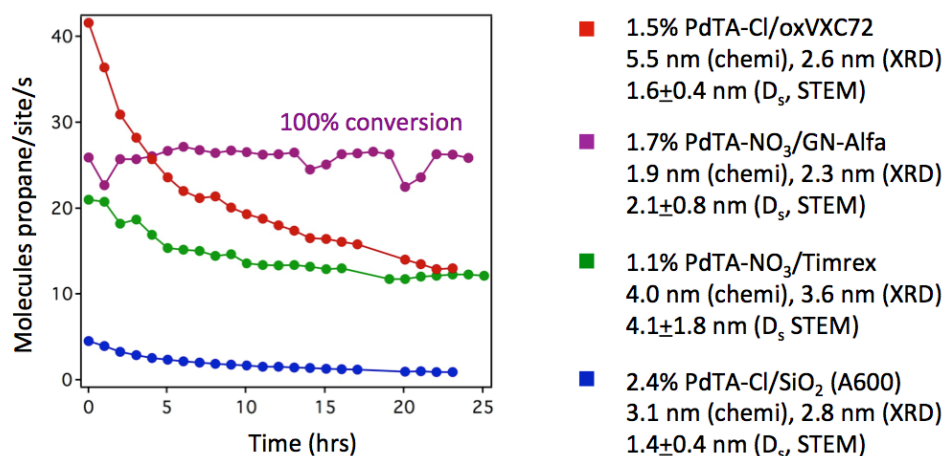
Figure 5.1. Propylene hydrogenation on supported Pd particles. The cationic precursor and supports are indicated in the legend. Reaction conditions were 2% propylene/10% H_2/balance He at 483 sccm total flow and -5 °C.

Here, our studies of propylene hydrogenation on Pd particles supported on a variety of supports, including graphene nanoplatelets, carbon black, graphitic carbon, and silica have demonstrated that the Pd/graphene catalyst has unusually high activity. Originally, the cationic SEA precursor [Pd $(NH_3)_4$]Cl_2, (PdTA-Cl) was used for adsorption of Pd particles under basic conditions. As shown in Figure 5.1, the activity of the catalyst synthesized from the PdTA-Cl precursor on silica (Aerosil 600) is substantially lower than that for the same precursor on oxidized VXC72(oxVXC72), which is an oxidized carbon black. Furthermore, the activity of the PdTA-NO3/Timrex,

which is a graphitic carbon support, was also higher than on silica. The PdTA-NO$_3$/GN-Alfa has exceptionally high activity with a conversion of 100%. The GN-Alfa support consists of high surface area (~420 m^2/g) graphene nanoplatelets and is also the support that the Gupton group found to have high activity for the Suzuki coupling reaction on supported Pd particles. However, it is difficult to directly compare the activities of these catalysts due to the varying particle sizes, different metal precursors, and the presence of residual chloride. Therefore, experiments were undertaken to prepare chlorine-free particles of different sizes on three supports: oxidized graphene nanoplatelets (oxGN-Alfa, surface area ~420 m^2/g), oxidized VXC72 (oxVXC72), and silica (OX50). The VXC72 and GN-Alfa supports were oxidized by treatment in nitric acid at 90 °C; this treatment adds oxygen functionality to the surface and results in a lowering of the point of zero charge to a range suitable for the chlorine-free cationic [Pd (NH$_3$)$_4$](NO$_3$)$_2$ (PdTA-NO$_3$) precursor for SEA adsorption under basic conditions. Larger particles were prepared by annealing the catalysts to different temperatures for 4 hours in a helium environment.[18,19]

5.2. EXPERIMENTAL METHODS
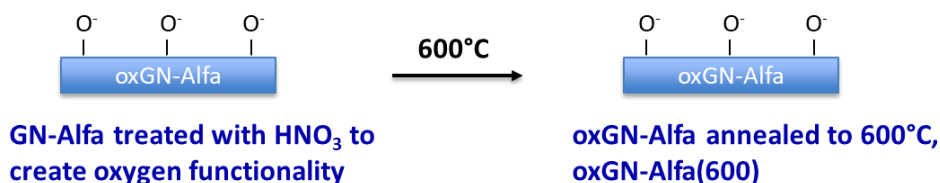
Figure 5.2: Preparation oxGN-Alfa (600) support.

Supports for Catalyst Preparation

Commercially available carbon and silica were used as supports for this study. VXC72, a carbon black, was purchased from Cabot Corporation and graphene nanoplatelets (GN-Alfa) was purchased from Alfa Aesar. These carbon supports were oxidized by boiling in

nitric acid (>70%) at 90 °C for 3 hours followed by cooling it at room temperature as shown in Figure 5.2. The mixture was then filtered and washed with deionized (DI) water until the pH of the washing solutions reached that of DI water and followed by drying overnight at room temperature. The resulting oxidized VXC72(oxVXC72) and oxidized GN-Alfa(oxGN-Alfa) were then pre-annealed to 600°C, the maximum temperature to be used for catalyst synthesis for these supports and referred to as oxVXC72(600) and oxGN-Alfa (600) respectively. Non-porous silica support (OX50), was purchased from Aerosil and pre-annealed to 800°C, the maximum temperature to be used for catalyst synthesis for this support and referred to as OX50(800). The maximum temperatures for support pretreatments were determined based on the maximum temperature the support can tolerate without losing any surface area. The BET surface areas of the non-annealed and annealed supports were then determined from nitrogen adsorption-desorption isotherms with a Micromeritics 2020 ASAP instrument. The point of zero charge (PZC) was determined by measuring the initial and final pH of a series of thick slurries at high surface loadings which generally gives a wide plateau over which the final pH remains constant even as the initial pH changes.[20] The method for determining the PZC and choosing the right precursor for SEA can be found in the literature.[8]

Preparation of catalysts

SEA[8,21] was used to prepare the catalysts. Based on the SEA protocol, the PZCs of the annealed and non-annealed supports were first determined as shown in Table 5.1, followed by electrostatic adsorption. The cationic Pd precursor was selected due to the low PZC of the supports. A non-chloride cationic precursor, tetraamminepalladium(II) nitrate (PdTA(Pd(NH$_3$)$_4$)NO$_3$, Sigma-Aldrich 99.999%) was used. The precursors were

contacted with the supports for 1 hr. at the optimal pH of adsorption used for silica and oxidized carbons[22], followed by filtration, overnight ambient air drying, and oven drying in static air at 120°C for 16 hrs. The dried catalysts were then, reduced at 180°C in a flowing 10% H_2 + balance He for 1 hr. with a ramp rate of 2.5°C/min.

Table 5.1. PZC of the unannealed and annealed carbon

Support	Annealing Temperature	PZC	Surface area(m^2/g)
VXC-72	None	8.2	230 m^2/g
oxVXC-72	None	2.5	230 m^2/g
oxVXC-72	600 °C	5.3	230 m^2/g
GN-Alfa	None	4.2	500m^2/g
GN-Alfa	600 °C	8.0	-
GN-Alfa	500 °C	7.9	-
GN-Alfa	400 °C	5.0	-
oxGN-Alfa	None	1.3	-
oxGN-Alfa	600 °C	6.2	-

Synthesis of catalysts with varying particle size

As mentioned earlier, larger particles were prepared by annealing the catalysts to different temperatures for 4 hours in a helium environment (Figure 5.3). Before metal deposition, the supports were pre-annealed to 800 °C for silica and 600 °C for carbon supports; these were the maximum temperatures used in the annealing experiments to form larger particles, and this treatment ensured that no further changes in the support occurred in the annealing of the catalysts. The VXC72 and GN-Alfa supports were

oxidized by heating at 90 °C in HNO_3 to decrease the PZC value to a range suitable for SEA with a cationic precursor at basic pH. For example, the GN-Alfa support was pre-annealed to 600 °C (referred to as oxGN-Alfa (600)) for 4 hours in a helium atmosphere. The PZC of the support increased to 6.2 after annealing (as shown in Table 5.1), and subsequent SEA with PdTA-NO_3 at a pH of 11 resulted in a low weight loading of 0.1%. Given the high activity of the Pd on GN-Alfa catalysts, this low weight loading has the advantage of allowing conditions for low conversion (<15%) to be achieved. To produce particles of different sizes via annealing, the catalysts were heated for 4 hours in He to the following temperatures for OX50 (600, 700, and 800 °C) and for oxVXC72, oxGN-
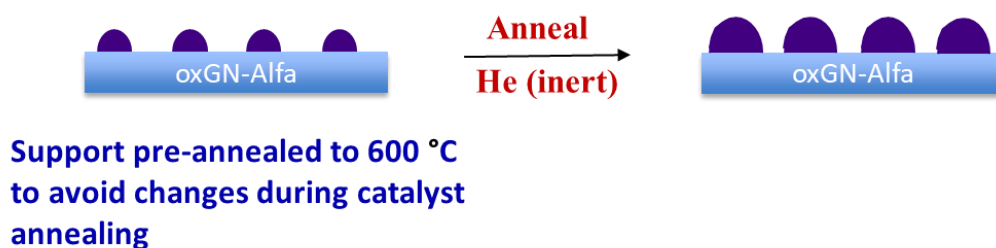
Figure 5.3. Schematic showing preparation catalyst with varying particle sizes by annealing

Alfa (400, 500, and 600 °C). OxVXC72 and oxGN-Alfa cannot be annealed to the higher temperatures due to the change in PZC, but in general larger transition metal clusters can be formed on carbon compared to oxides due to the longer diffusion lengths on carbon.[23]

Catalyst Characterization

X-Ray Diffraction (XRD):

A Rigaku Miniflex-II equipped with a D/teX Ultra silicon strip detector was used to perform powder XRD on the supported Pt particles. Diffraction patterns were recorded over a range of 10°–80° 2Θ using Cu-Kα radiation (k = 1.5406 Å) that was operated at 30

mA and 15 kV[24]. XRD patterns were obtained for all annealed, non-annealed supports and catalysts. Fityk 0.9.8 version software[25] was employed for background subtraction and deconvolutions using pseudo-Voigt shapes to take the peak asymmetry into account. The full width at half maximum (FWHM) values together with a shape factor of 0.94 were used in the Scherrer equation to estimate particle size. More details on the peak fitting using the Fityk software can be found elsewhere[26].

Scanning Transmission Electron Microscopy (STEM)

The aberration-corrected JEOL 2100F scanning transmission electron microscopy (STEM) was used for Z-contrast imaging with a 200 kV field emission gun and a double tilt holder for tilting the sample across a range of angles ($\pm20°$). High Angle Annular Dark-Field (HAADF) STEM images were acquired on a Fischione Model 3000 HAADF detector with a camera length such that the inner cut-off angle of the detector was 50 mrad. Sample preparation involved suspending the catalyst in isopropanol and depositing a drop of the suspension onto a holey carbon film attached to a Cu TEM grid. The images were recorded using Digital Micrograph software and particle size distributions were obtained by counting 100-500 particles on each sample. The number average diameter $D_n= \sum n_i d_i^2/ \sum n_i d_i$, the surface average diameter $D_s= \sum n_i d_i^3/ \sum n_i d_i^2$, and the volume average diameter $D_v= \sum n_i d_i^4/ \sum n_i d_i^3$ were calculated where n_i is the number of particles with diameter d_i. [18]

Chemisorption

Pulse chemisorption of the samples was performed using the Micromeritics AutoChem 2020. The process involved hydrogen titration of oxygen pre-covered Pd surfaces. A pretreatment step included drying at 120°C followed by a reduction in 10%

hydrogen at 200°C. The catalyst was then contacted with 10% oxygen in helium at 40°C for 30 min to oxidize the surface Pd to PdO. Then, it was titrated with pulsed 10% hydrogen in argon to form water and surface Pd with chemisorbed hydrogen. The assumed overall stoichiometry is 0.667 Pd:1 H_2 [27]. Particle sizes were estimated from chemisorption assuming hemispherical geometry. Since chemisorption is a surface technique, it is compared to surface average STEM sizes, whereas XRD is the volume /bulk technique and is compared to the volume average STEM sizes[18].

Catalyst Evaluation

Catalysts were evaluated in a 0.19" ID packed bed, tubular flow reactor (316 stainless steel), which has been previously described in more detail elsewhere.[28] The temperature of the reactor is controlled using a jacketed shell, which is connected to a recirculation bath containing glycol/H_2O as a coolant to maintain isothermal conditions at -5°C. Higher temperatures were achieved using heating tape wrapped around the body of the reactor, and the temperature of the reactor was monitored by a thermocouple inserted directly into the catalyst bed. All gas flows were maintained by mass flow controllers (Brooks 5850E series). The feed gas mixture for propylene hydrogenation was 5% C_3H_6/ 20% H_2/balance He at a total flow rate of 100 sccm. Gas analysis was carried out with a Hewlett-Packard 5890 Series II chromatograph equipped with an HP-PLOT/Q capillary column using a flame ionization detector(FID). All of the Pd/carbon and Pd /oxide samples were evaluated for propylene hydrogenation. The reactor was typically loaded with 0.005 g of catalyst diluted with 0.025 g of alumina support to form a catalyst bed that was supported on glass wool in the middle of the reactor. All the catalysts were pre-treated/reduced at 200°C for 1 hr in 10% H_2/balance He before cooling down to -5°C for

catalyst evaluation. The feed stream of the catalyst screening consisted of 5% C_3H_6, 20% H_2, balance He at a total flow rate of 100 sccm. Typically, reaction feed and products were evaluated every 1 hr using an automated, online Hewlett-Packard 5890 Series II gas chromatograph using a flame-ionization detector (FID). These catalysts exhibited high initial activities and underwent varying degrees of deactivation for several first hours online. Therefore all the reaction data reported here were based on the stable catalyst performance after 15 to 20 hrs online to eliminate transient behavior.

5.3. RESULTS AND DISCUSSION
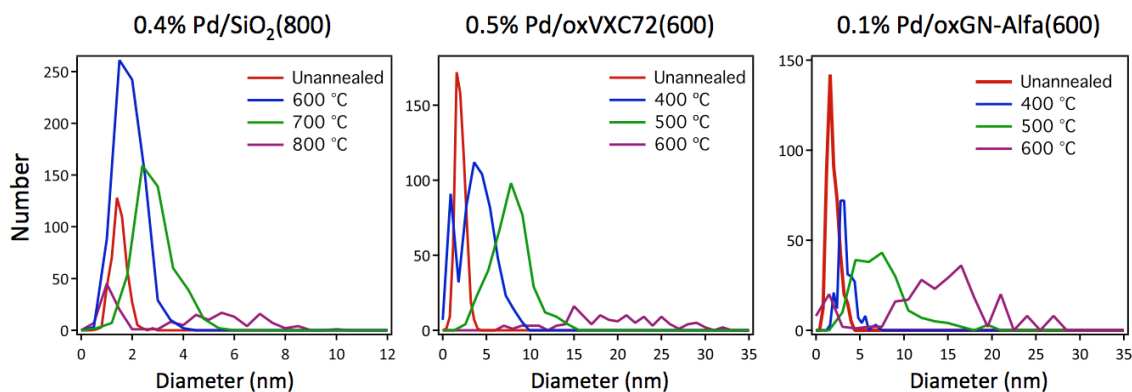
Figure 5.4. STEM particle distributions for Pd on the pre-annealed SiO_2, oxVXC72 and oxGN-Alfa supports after annealing the catalysts to various temperatures in a helium environment.

Figure 5.4 reports STEM particle distributions for Pd on the pre-annealed SiO_2, oxVXC72 and oxGN-Alfa supports after annealing the catalysts to various temperatures in a helium environment. On silica, the unannealed catalyst shows the smallest sizes with the narrowest distribution (D_s=1.8$\pm$0.3 nm). Annealing to 600 °C increases the particle size to 2.6$\pm$0.6 nm, but the distribution remains relatively narrow. The Pd/SiO$_2$ catalyst was heated to 600 °C to achieve particle sizes comparable to those on the unannealed carbon supports (2.5 nm), but the size distribution remains uniform. After heating to 700

°C, the average particle size increases to 3.7±0.8 nm while maintaining the narrow

distribution. At 800 °C, significantly larger particles are formed (6.2±3.3 nm), but the

distribution becomes bimodal with very small particles (<2 nm) coexisting with larger

ones. It should be noted that that the particles smaller than 4 nm account for only 5% of

the total surface area. Representative STEM images and corresponding particle size

distribution of unannealed Pd/ Silica and that annealed at 800 °C are shown in Figure 5.5.

On the two carbon supports, the average particle size for the unannealed catalyst

is slightly larger at 2.5-2.6 nm, but the distributions are still relatively narrow (0.6-0.8 nm

standard deviation). In the case of Pd on oxGN-Alfa, annealing to only 400 °C results in
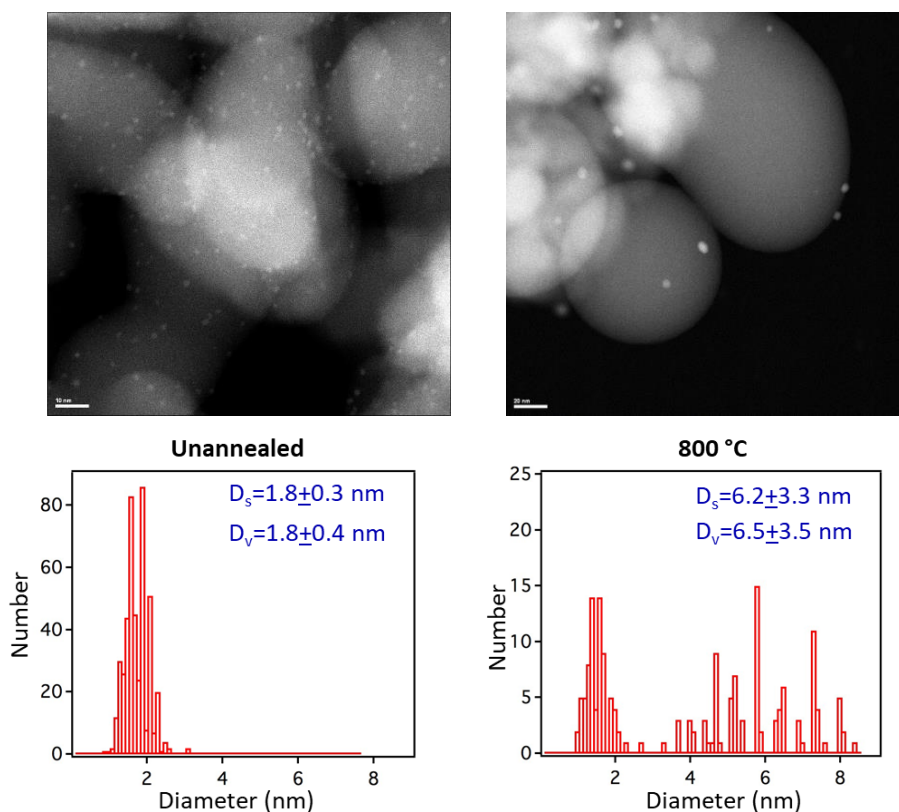
Figure 5.5 Representative STEM images of unannealed(left) and 800°C annealed(right) 0.4% Pd/SiO$_2$(OX50) and their corresponding size distribution.

significantly larger particle size (4.2±1.1 nm), and annealing to 500 °C increases the
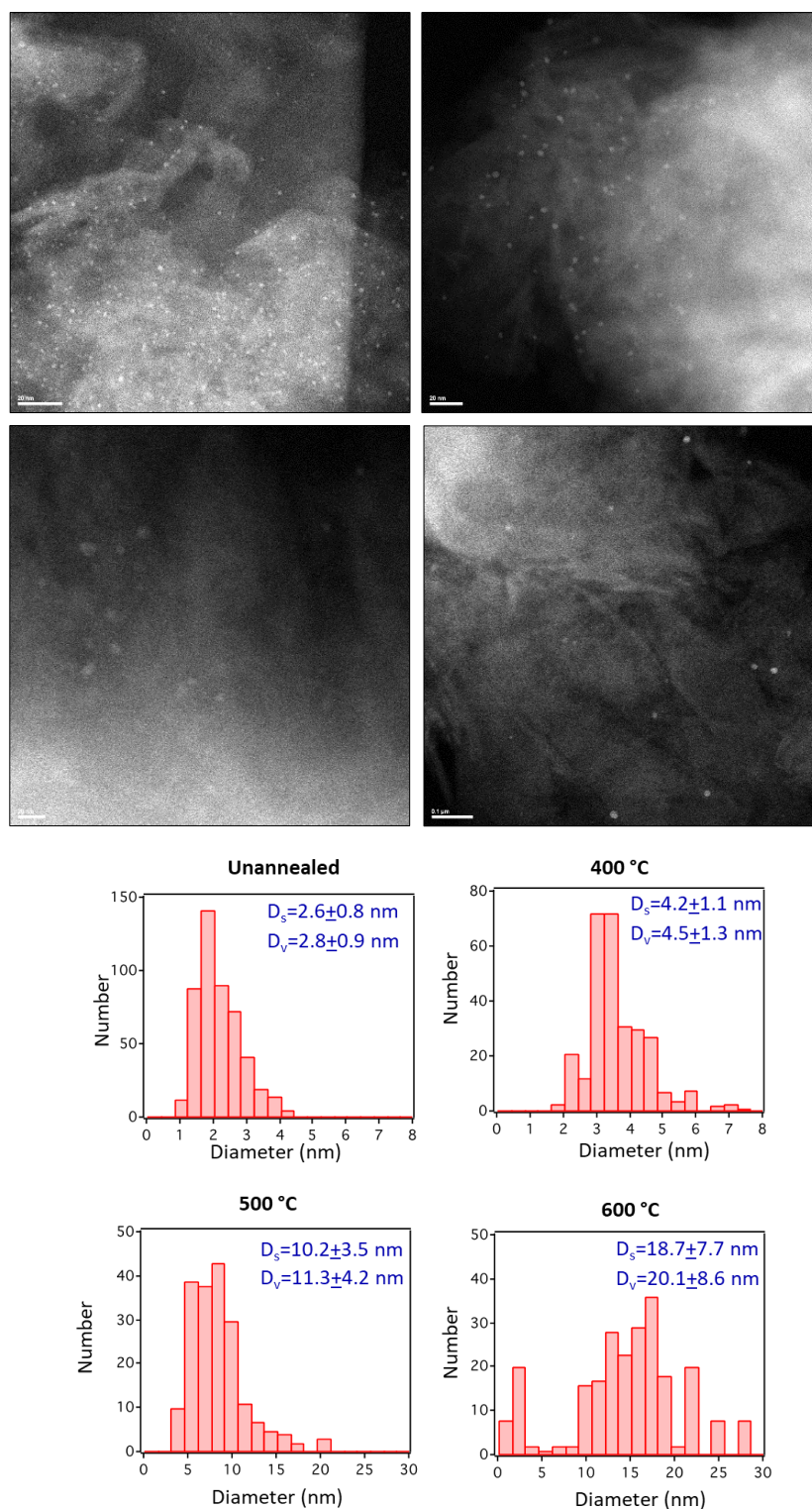
Figure 5.6 Representative STEM images and corresponding particle size distribution of Pd/oxGN-Alfa(600): unannealed(top left),annelaed at temperatures 400°C (top right), 500°C (bottom left) and 600 °C (bottom right).

average particle size to the much larger value of 10.2$\pm$3.5 nm; in both cases, the

distributions are still reasonably narrow. After heating to 600 °C, the average particle

size increases to 18.7±7.7 nm, and the distribution becomes broad and bimodal. Figure

5.6 shows representative STEM images and corresponding particle size distributions of

unannealed Pd/ oxGN-Alfa catalysts and that are annealed at temperatures of 400 °C, 500

°C, and 600 °C. For Pd on oxVXC72, large particles (5.7±2.4 nm) with a broad size

distribution are produced after annealing to the lowest temperature of 400 °C. At 500 °C

the average size increases to 9.8±2.5 nm and at 600 °C, almost exclusively large particles

>15 nm in diameter are observed with 80% of the surface area attributed to particles

greater than 20 nm. Figure 5.7 shows representative STEM images and corresponding

particle size distribution of unannealed Pd/oxVXC72 and that annealed at 600 °C.
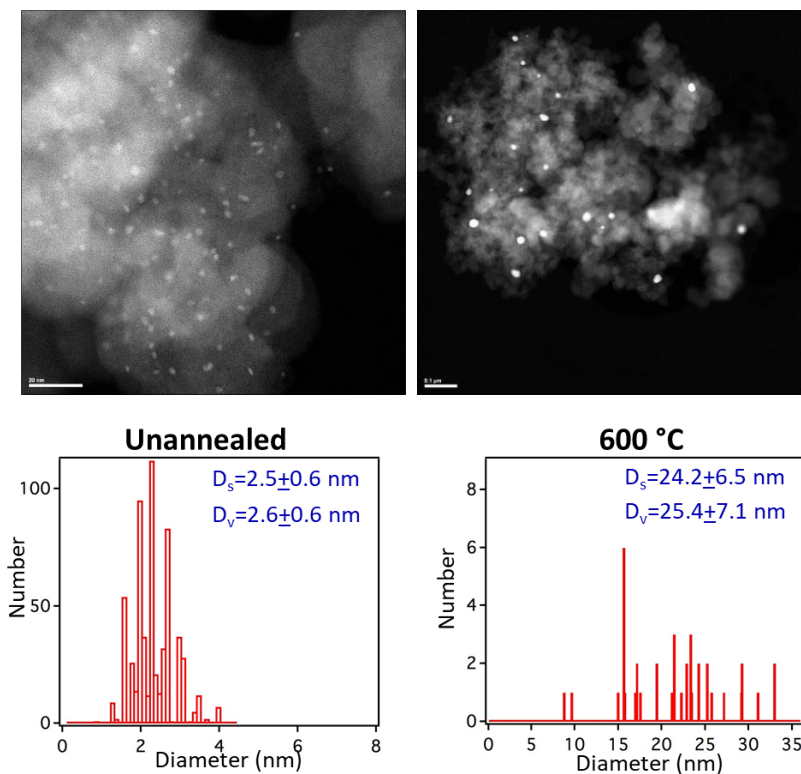
Figure 5.7 STEM images and corresponding particle size distribution of Pd/oxVXC72(600): unannealed(left),annelaed at temperatures 600 °C (right).

Size estimates for chemisorption, XRD, and STEM are summarized in Table 5.2. The chemisorption sizes after carbon burn-off are shown in parenthesis. A comparison of particle sizes determined from STEM and chemisorption measurements demonstrate that the surfaces of the unannealed Pd particles on oxVXC72 and oxGN-Alfa appear to be decorated by carbon species (Figure 5.8). The chemisorption experiments were carried out by first reducing the catalyst in H_2 at 200 °C, followed by exposure to O_2 at 40 °C and then titrating with H_2 at 40 °C. Similarly, on oxGN-Alfa, the chemisorption particle size was 5.4 nm with the STEM particle size at 2.6±0.8 nm. After the catalysts are subjected to a treatment in 10% O_2 at 300 °C for 1 hour, the chemisorption particle sizes for both Pd/C catalysts decreased substantially, and these values become more consistent with the STEM particle sizes. Thus, it appears that the decorating carbon species can be burned off in O_2.[10,29] In contrast, the Pd/SiO_2 particles, which cannot be decorated by carbon, have almost identical chemisorption and STEM particles sizes.
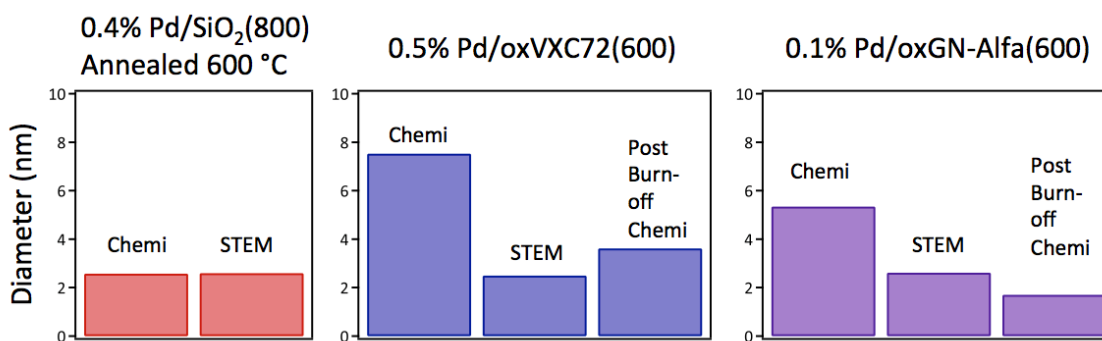
**Figure 5.8.** Comparison of chemisorption and STEM diameters for the unannealed catalysts on the different supports.

Propylene hydrogenation was studied under the following conditions: 5% propylene/20% H_2/balance He, -5 °C, 100 sccm total flow, 0.625-5.00 mg catalyst mixed with alumina support (30 mg total), and ~24-hour reaction time. The mass of the catalyst was adjusted to keep the conversion below 20%.

Figure 5.9a shows the rate of product formation/g Pd as a function of time online for the PdTA-NO$_3$/SiO$_2$ (OX50) catalysts annealed to various temperatures. The unannealed catalyst had high initial activity, which dropped by 45% over the first 10 hours but was stable after that. All the other catalysts had lower activities that decreased with annealing

Table 5.2. Particle sizes for Pd particles on various pre-annealed supports estimated by Chemisorption, XRD and STEM measurements. Chemisorption diameters are after carbon burnoff are shown in parenthesis.

Precursor	Support	weight loading (%)	Annealing temperature (°C)	Chemi diameter (nm)	XRD diameter (nm)	STEM diameter (nm)
PdTA-NO$_3$	SiO$_2$ (OX50)	0.39	none	1.1	<1.5	1.8$\pm$0.3 (D$_s$) 1.8+0.4 (D$_v$)
PdTA-NO$_3$	SiO$_2$ (OX50)	0.39	600	2.6	<1.5	2.6$\pm$0.6 (D$_s$) 2.7+0.7 (D$_v$)
PdTA-NO$_3$	SiO$_2$ (OX50)	0.39	700	4.5	3.4	3.7$\pm$0.8 (D$_s$) 3.8+0.9 (D$_v$)
PdTA-NO$_3$	SiO$_2$ (OX50)	0.39	800	7.2	5.5	6.2$\pm$3.3 (D$_s$) 6.5+3.5 (D$_v$)
PdTA-NO$_3$	oxidized VXC72	0.50	none	7.6	1.6	2.5$\pm$ 0.6(D$_s$) 2.6$\pm$0.6 (D$_v$)
PdTA-NO$_3$	oxidized VXC72	0.50	400	9.9	3.0	5.7$\pm$2.4 (D$_s$) 6.1$\pm$2.7 (D$_v$)
PdTA-NO$_3$	oxidized VXC72	0.50	500	17.7	7.9	9.8$\pm$2.5 (D$_s$) 10.3$\pm$2.8 (D$_v$)
PdTA-NO$_3$	oxidized VXC72	0.50	600	42.5	14.7	24.2$\pm$6.5 (D$_s$) 25.4$\pm$7.1 (D$_v$)
PdTA-NO$_3$	oxidized GN-Alfa	0.10	none	5.4 (1.7)	---	2.6$\pm$0.8 (D$_s$) 2.8+0.9 (D$_v$)
PdTA-NO$_3$	oxidized GN-Alfa	0.10	400	3.5 (3.1)	---	4.2$\pm$1.1 (D$_s$) 4.5+1.3 (D$_v$)
PdTA-NO$_3$	oxidized GN-Alfa	0.10	500	7.7 (6.0)	---	10.2$\pm$3.5 (D$_s$) 11.3+4.2 (D$_v$)
PdTA-NO$_3$	oxidized GN-Alfa	0.10	600	31.2	---	18.7$\pm$7.7 (D$_s$) 20.1+8.6 (D$_v$)

temperature and were relatively stable over time. The conversion for the unannealed catalyst was over 40% initially but decreased to around 20% by 24 hours, whereas the conversions for the annealed catalysts were much lower (<15%) (Figure 5.9b).

To determine turnover frequencies (TOF), the reaction rates were normalized by dividing by the number of active sites calculated from chemisorption, STEM, and XRD data. In the chemisorption experiments, the catalyst was reduced at 200 °C for 1 hr in H_2, exposed to O_2 at 40 °C, and then titrated with H_2 at 40 °C. XRD surface areas were determined from the weight loading and the assumption that all particles have a hemispherical particle shape with the average particle diameter determined by XRD.

Figure 5.9. Hydrogenation activity for PdTA-NO$_3$/SiO$_2$ (OX50) annealed to various temperatures: a) rate/g Pd; b) conversion; and TOFs calculated using number of surface sites determined by: c) chemisorption; d) STEM; and e) XRD.

STEM surface areas were calculated from the weight loading, diameter measurements for individual clusters, and the assumption of hemispherical particle size.

For Pd/OX50, plots of TOF vs. time online for all these surface area calculations are shown in Figure 5.9c. For the TOFs normalized by chemisorption data, the unannealed surface has the highest average TOF of 24 s^{-1} after 24 hours; this value drops to 14-18s^{-1} for the 600 °C and 700 °C-annealed catalysts, which have activities are within experimental

error of each other. The average TOF for the 800 °C-annealed catalysts is further decreased to 9.7 s^{-1}, thus indicating a clear reduction in TOF with increasing particle size. The STEM-normalized TOF data (Figure 5.9d) also demonstrate the following: the unannealed catalyst has the highest TOF; the TOFs for the 600 °C- and 700 °C-annealed catalysts are decreased but similar to each other, and the TOF for the 800 °C-annealed catalysts is the lowest. Similar results are observed for the XRD-normalized TOFs although particle diameters were below the detection limit for the unannealed and 400 °C-annealed catalysts (Figure 5.9e).

Figure 5.10. Hydrogenation activity for PdTA-NO$_3$/oxVXC72 annealed to various temperatures: a) rate/g Pd; b) conversion; and TOFs calculated using number of surface sites determined by: c) chemisorption; d) STEM; and e) XRD.

The reaction rates/g Pd are also shown for the oxVXC72-supported Pd catalysts (Figure 5.10a). The unannealed and 400 °C-annealed have almost identical initial activities, but the unannealed catalyst deactivates more quickly than the 400 °C-annealed, which has the highest activity after 24 hours. The 500 °C- and 600 °C-annealed catalysts

exhibit activities that decrease with increasing particle size, but there is almost no loss of activity over time, unlike the catalysts annealed to lower temperatures. Conversions for all these catalysts were less than 15%, as shown in Figure 5.10b. After correcting the activity for the number of surface sites from chemisorption, the TOFs as a function of time online (Figure 5.10c) illustrate that these values are nearly identical for the unannealed and 800 °C-annealed catalysts and somewhat higher for the catalysts annealed to intermediate temperatures. The same general trends are observed for the activities corrected by the STEM and XRD surface sites (Figure 5.10d,e). A possible
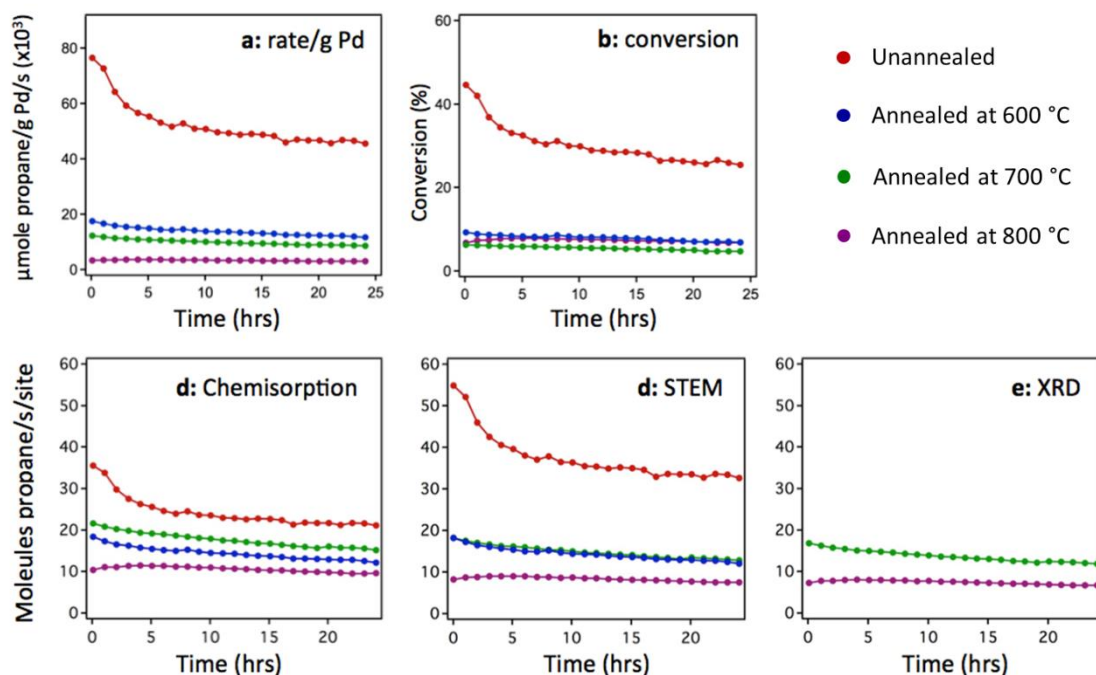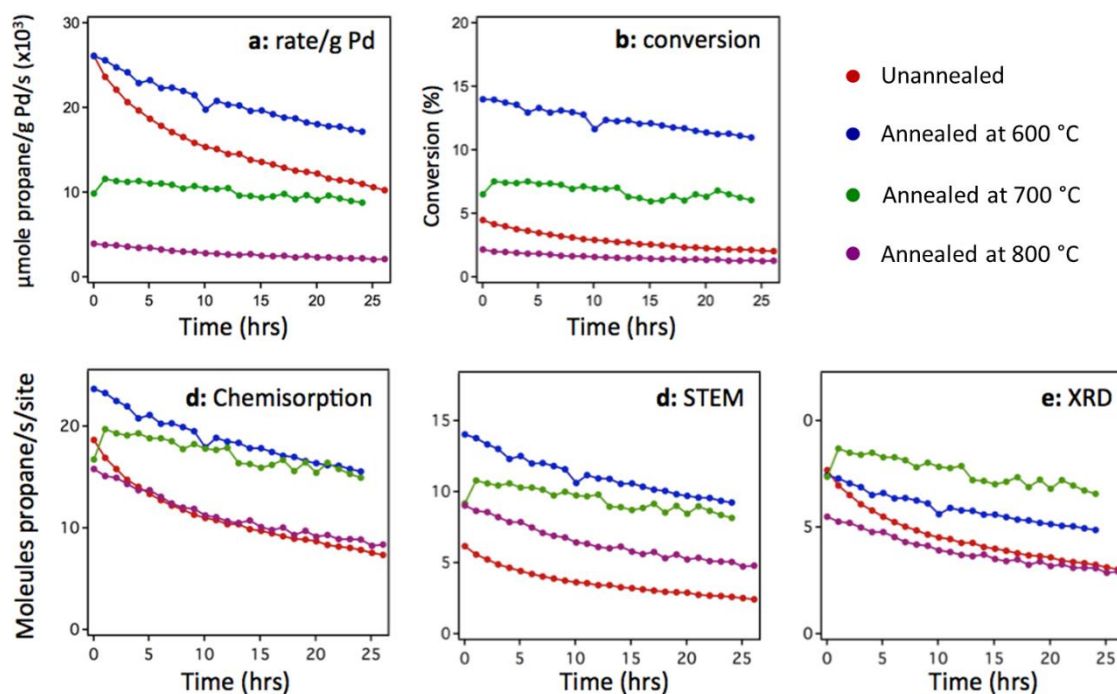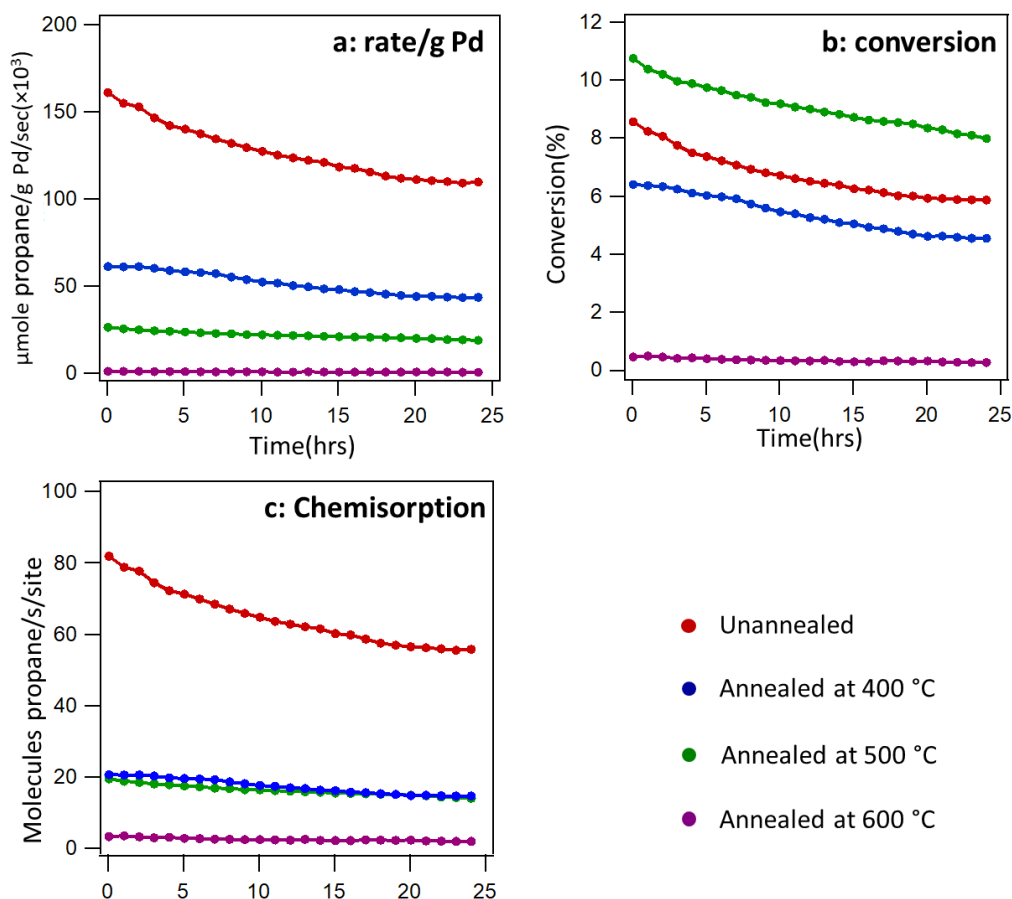

Figure 5.11. Hydrogenation activity for PdTA-NO$_3$/oxGN-alfa annealed to various temperatures: a) rate/g Pd; b) conversion; and TOFs calculated using number of surface sites determined by: c) chemisorption.

explanation for this behavior is that for the small Pd particles, some fraction of the active, undercoordinated sites are passivated by carbon atoms from the support. The passivation effect is lower for the intermediate-sized clusters, thus resulting in slightly higher activity at 400 °C. For the larger particles, the TOFs decrease with particle size since the large particles have fewer undercoordinated sites. The TOF data normalized by STEM and XRD surface sites show the same general trend in that the 400 °C- and 500 °C-annealed catalysts have slightly higher activity than the unannealed, whereas the 600 °C-annealed catalysts have TOFs more comparable to the unannealed catalyst.

The reaction rates/g Pd are shown for the oxGN-Alfa supported Pd catalysts (Figure 5.11a). The unannealed catalyst had significantly high activity compared to 400, 500, and 600 °C annealed catalysts but the unannealed catalyst deactivated more quickly than
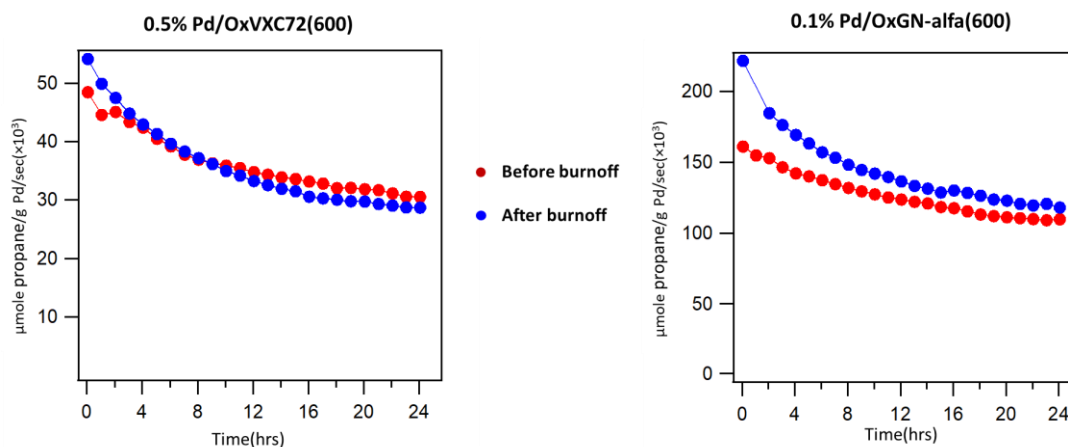
Figure 5.12. Propylene hydrogenation activity for unannealed Pd/oxVXC72 and Pd/oxGN-Alfa catalysts before and after carbon burn off. Reactions conditions were 5% propylene/20% H_2/balance He at 100 sccm and -5 °C.

annealed catalysts, however, it had highest activity after 24 hours. The 400°C, 500°C- and 600°C-annealed catalysts exhibit activities that decrease with increasing particle size, but there is almost no loss of activity over time, unlike the unannealed catalyst. Conversions for all these catalysts were less than 11%, as shown in Figure 5.11b. After

correcting the activity for the number of surface sites from chemisorption, the TOFs as a function of time online (Figure 5.11c) illustrate that the TOF for the unannealed catalyst was 82 s^{-1} which decreased to 56 s^{-1} after 24 hrs with an average TOF of 65 s^{-1}; this value was significantly higher compared to catalysts annealed to higher temperatures. This value drops to 16-17 s^{-1} for the 600 °C and 700 °C-annealed catalysts respectively. The average TOF for the 800 °C-annealed catalyst is further decreased to 2.4 s^{-1}, thus indicating a clear reduction in TOF with increasing particle size.

Propylene hydrogenation activity was examined as a function of time on stream for the catalysts before and after carbon burn-off (Figure 5.12). Surprisingly, on both oxVXC72 and oxGN-Alfa, there is very little difference in activity (μmol propane/g Pd/s) for the catalysts before and after burnoff, even though that the number of chemisorption active sites increases after burn-off by a factor of 2 for oxVXC72 and a factor of 3 for oxGN-Alfa. A possible explanation for this is that the activity of the Pd particles is dominated by active sites that are not blocked by the decorating carbon. For example, the decorating carbon may reside at terrace sites, which are not as active for propylene
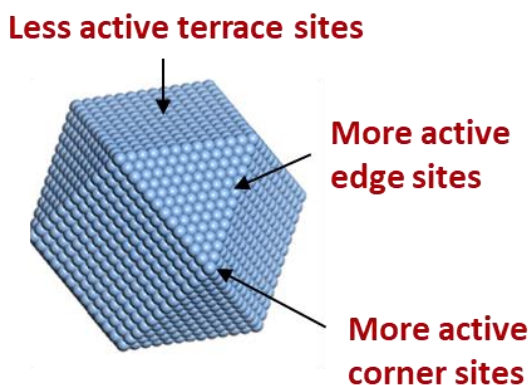
Figure 5.13. Depiction of Pd particle showing most active edge and corner sites and less active terrace sites.

hydrogenation compared to step and edge sites as shown in Figure 5.13. Figure 5.14 represents propylene hydrogenation activity for the Pd-particles of different sizes on the three different supports. On the SiO_2 support, there is a marked decrease in activity with increasing particle size; this suggests that that the step and edge defect sites, which comprise a greater fraction of the surface of small particles, are the more active sites (Figure 5.14a).

For the Pd/oxGN-Alfa catalyst, the activity for the unannealed 2.5 nm particles is surprisingly high and comparable to that of the smallest Pd/SiO$_2$ particles. The activity of this catalyst also decreases sharply with increasing particles size. In contrast, the Pd/oxVXC72 catalyst does not show the same decrease in activity with particle size. However, it should be noted that the Pd/oxVXC72 catalysts have extensive carbon
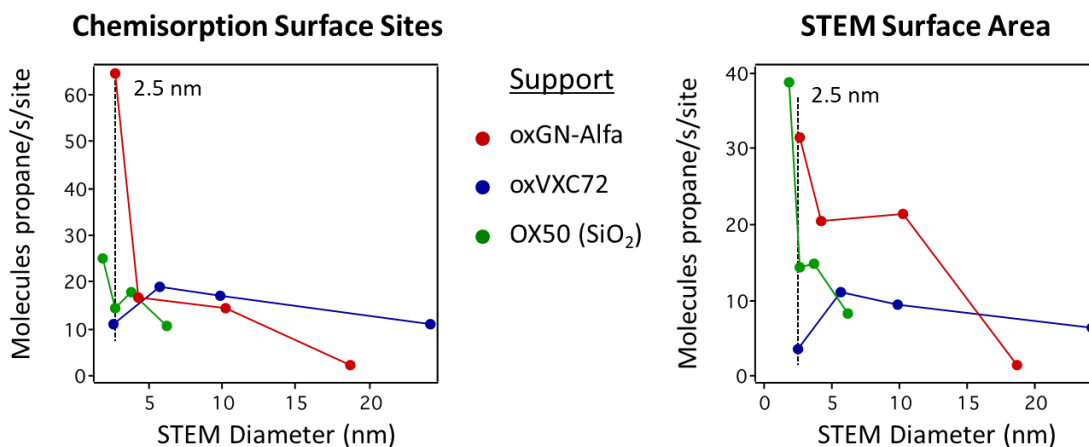
Figure 5.14. Propylene hydrogenation activity as a function of STM particle size for Pd particles on oxGN-Alfa, oxVXC72 and OX50. Reactions conditions were 5% propylene/20% H$_2$/balance He at 100 sccm and -5 °C.

decoration for particles of all sizes, whereas the carbon decoration on Pd/oxGN-Alfa is significant only on the smallest particles. For particles of the same 2.5 nm size, the activity is greatest for the Pd/GN-Alfa catalyst. To account for the loss in activity due to

carbon decoration, the activity per chemisorption site was also plotted in Figure 5.14. In this case, the activity of the 2.5 nm particles is still highest on the Pd/GN-Alfa support, and the Pd/SiO$_2$ and Pd/oxVXC72 have comparable activity per surface Pd atom. The larger particles on both carbon supports have similar activity except for the catalysts annealed to the highest temperature, where the size distributions are the broadest and it is difficult to fully represent particles sizes with an average value. One possible explanation for the enhanced activity of Pd/oxGN-Alfa is that hydrogen intercalated in the graphene nanoplatelets could provide an additional supply of hydrogen.[30] A detailed H$_2$-TPD (temperature-programmed desorption) investigations as described by Rupprechter *etal*[30] on different Pd catalysts including Pd/GN-Alfa and GN-Alfa supports are underway to show if the GN-Alfa could intercalate hydrogen that could act as a source of additional hydrogen during propylene hydrogenation.

5.4 CONCLUSION

Pd particles were deposited on silica, oxGN-Alfa, and oxVXC72 supports by SEA where the particles sizes were varied by annealing at different temperatures. The changes in the particle's sizes after the annealing were estimated by chemisorption, XRD, and STEM measurements. The propylene hydrogenation reaction was studied on these catalysts. We found that propylene hydrogenation on Pd exhibits a particle size effect on SiO$_2$ and oxGN-Alfa supports, with greater activity observed on the smaller particles. This behavior is most pronounced for the Pd/SiO$_2$ catalysts, which are not complicated by carbon decoration effects. On both carbon supports, the Pd particles are decorated by carbon from the support, based on the larger chemisorption particle sizes that decrease to approximately the same values as the STEM particle sizes after a carbon burnoff

treatment. Since carbon decoration is most significant on the oxVXC72 support, this catalyst does not exhibit a clear decrease in activity with particle size. For particles of the same 2.5 nm size on the three supports, the catalytic activity is markedly higher for Pd on GN-Alfa, indicating that the graphene nanoplatelets promote Pd hydrogenation activity.

ACKNOWLEDGEMENTS

5.5. REFERENCES

1. Schlummer, B. & Scholz, U. Palladium-catalyzed C-N and C-O coupling - A practical guide from an industrial vantage point. *Adv. Synth. Catal.* **346**, 1599–1626 (2004).

2. Adams, B. D. & Chen, A. The role of palladium in a hydrogen economy. *Mater. Today* **14**, 282–289 (2011).

3. Teschner, D. *et al.* Understanding palladium hydrogenation catalysts: When the nature of the reactive molecule controls the nature of the catalyst active phase. *Angew. Chemie - Int. Ed.* **47**, 9274–9278 (2008).

4. Borodziński, A. & Bond, G. C. Selective hydrogenation of ethyne in ethene-rich streams on palladium catalysts. Part 1. Effect of changes to the catalyst during reaction. *Catal. Rev. - Sci. Eng.* **48**, 91–144 (2006).

5. Buchwald, S. L., Mauger, C., Mignani, G. & Scholz, U. Industrial-scale palladium-catalyzed coupling of aryl halides and amines - A personal account. *Adv. Synth. Catal.* **348**, 23–39 (2006).

6. Gilliland, S. E. *et al.* Electrostatic adsorption-microwave synthesis of palladium nanoparticles on graphene for improved cross-coupling activity. *Appl. Catal. A Gen.* **550**, 168–175 (2018).

7. Brinkley, K. W., Burkholder, M., Siamaki, A. R., Belecki, K. & Gupton, B. F. The continuous synthesis and application of graphene supported palladium nanoparticles: A highly effective catalyst for Suzuki-Miyaura cross-coupling reactions. *Green Process. Synth.* **4**, 241–246 (2015).

8. Regalbuto, J. *Strong Electrostatic Adsorption of Metals onto Catalyst Supports*. *Catalyst Preparation* (2006). doi:10.1201/9781420006506.ch13

9. Hao, X., Barnes, S. & Regalbuto, J. R. A0020fundamental study of Pt impregnation of carbon: Adsorption equilibrium and particle synthesis. *J. Catal.* **279**, 48–65 (2011).

10. Tengco, J. M. M., Lugo-José, Y. K., Monnier, J. R. & Regalbuto, J. R. Chemisorption-XRD particle size discrepancy of carbon supported palladium: Carbon decoration of Pd? *Catal. Today* **246**, 9–14 (2015).

11.   Van Helden, P., Ciobîcə, I. M. & Coetzer, R. L. J. The size-dependent site composition of FCC cobalt nanocrystals. *Catal. Today* **261**, 48–59 (2016).

12.   Torres Galvis, H. M. *et al.* Iron particle size effects for direct production of lower olefins from synthesis gas. *J. Am. Chem. Soc.* **134**, 16207–16215 (2012).

13.   Den Breejen, J. P. *et al.* On the origin of the cobalt particle size effects in Fischer-Tropsch catalysis. *J. Am. Chem. Soc.* **131**, 7197–7203 (2009).

14.   Beerthuis, R. *et al.* Particle size effects in copper-catalyzed hydrogenation of ethyl acetate. *J. Catal.* **388**, 30–37 (2020).

15.   Durndell, L. J. *et al.* Selectivity control in Pt-catalyzed cinnamaldehyde hydrogenation. *Sci. Rep.* **5**, 1–9 (2015).

16.   van den Reijen, J. E. *et al.* Preparation and particle size effects of Ag/A-Al2O3 catalysts for ethylene epoxidation. *J. Catal.* **356**, 65–74 (2017).

17.   van Santen, R. A. Insensitive Catalytic Relationships. *Acc. Chem. Res.* **42**, 57–66 (2009).

18.   Datye, A. K., Xu, Q., Kharas, K. C. & McCarty, J. M. Particle size distributions in heterogeneous catalysts: What do they tell us about the sintering mechanism? *Catal. Today* **111**, 59–67 (2006).

19.   Hansen, T. W., Delariva, A. T., Challa, S. R. & Datye, A. K. Sintering of catalytic nanoparticles: Particle migration or ostwald ripening? *Acc. Chem. Res.* **46**, 1720–1730 (2013).

20.   Park, Jaehyeon and Ragabulto, J. R. REGALBUTO J.R.; PARK J. 1994.pdf. *Journal of Colloid and Interface Science* **175**, 239–252 (1995).

21.   Brunelle, J. P. Preparation of catalysts by metallic complex adsorption on mineral oxides: . *Pure Appl. Chem.* **50**, 1211–1229 (1978).

22.   Cho, H. R. & Regalbuto, J. R. The rational synthesis of Pt-Pd bimetallic catalysts by electrostatic adsorption. *Catal. Today* **246**, 143–153 (2015).

23.   Galhenage, R. P. *et al.* Platinum-ruthenium bimetallic clusters on graphite: A comparison of vapor deposition and electroless deposition methods. *Phys. Chem. Chem. Phys.* **17**, 28354–28363 (2015).

24. O'Connell, K. & Regalbuto, J. R. High Sensitivity Silicon Slit Detectors for 1 nm Powder XRD Size Detection Limit. *Catal. Letters* **145**, 777–783 (2015).

25. Wojdyr, M. Fityk: A general-purpose peak fitting program. *J. Appl. Crystallogr.* **43**, 1126–1128 (2010).

26. Banerjee, R., Liu, Q., Tengco, J. M. M. & Regalbuto, J. R. Detection of Ambient Oxidation of Ultrasmall Supported Platinum Nanoparticles with Benchtop Powder X-Ray Diffraction. *Catal. Letters* **147**, 1754–1764 (2017).

27. Benson, J. E. & Boudart, M. Hydrogen-oxygen titration method for the measurement of supported platinum surface areas. *J. Catal.* **4**, 704–710 (1965).

28. Zhang, Y., Diao, W., Williams, C. T. & Monnier, J. R. Selective hydrogenation of acetylene in excess ethylene using Ag- and Au-Pd/SiO2 bimetallic catalysts prepared by electroless deposition. *Appl. Catal. A Gen.* **469**, 419–426 (2014).

29. Banerjee, R. & Regalbuto, J. R. Rectifying the chemisorption – XRD discrepancy of carbon supported Pd: Residual chloride and/or carbon decoration. *Appl. Catal. A Gen.* **595**, 117504 (2020).

30. Dobrezberger, K. *et al.* Hydrogenation on Palladium Nanoparticles Supported by Graphene Nanoplatelets. (2020). doi:10.1021/acs.jpcc.0c06636

REFERENCES

1. Védrine, J. C. Applied Catalysis A : General Revisiting active sites in heterogeneous catalysis : Their structure and their dynamic behaviour. *"Applied Catal. A, Gen.* **474**, 40–50 (2014).

2. Medford, A. J. *et al.* From the Sabatier principle to a predictive theory of transition-metal heterogeneous catalysis. *J. Catal.* **328**, 36–42 (2015).

3. Fechete, I., Wang, Y. & Védrine, J. C. The past, present and future of heterogeneous catalysis. *Catal. Today* **189**, 2–27 (2012).

4. Max, J. H. Chemical Science Promoting heterogeneous catalysis beyond catalyst design. 1456–1468 (2020). doi:10.1039/c9sc05947d

5. Thermodynamics, K. V., Centers, A., Cycles, C., Ma, Z. & Zaera, F. Heterogeneous Catalysis by Metals. *Encycl. Inorg. Bioinorg. Chem.* 1–16 (2014). doi:10.1002/9781119951438.eibc0079.pub2

6. Friend, C. M. & Xu, B. Heterogeneous Catalysis: A Central Science for a Sustainable Future. (2017). doi:10.1021/acs.accounts.6b00510

7. Taylor, K. C. Automobile Catalytic Converters BT - Catalysis: Science and Technology Volume 5. in (eds. Anderson, J. R. & Boudart, M.) 119–170 (Springer Berlin Heidelberg, 1984). doi:10.1007/978-3-642-93247-2_2

8. Chemistry, P. A Theory o f the Catalytic Surface. **28**, 105–111 (1925).

9. Hannagan, R. T., Giannakakis, G., Flytzani-stephanopoulos, M. & Sykes, E. C. H. Single-Atom Alloy Catalysis. (2020). doi:10.1021/acs.chemrev.0c00078

10. Liu, D. *et al.* Identifying Dynamic Structural Changes of Active Sites in Pt-Ni Bimetallic Catalysts Using Multimodal Approaches. *ACS Catal.* **8**, 4120–4131 (2018).

11.   Wang, Y. G., Mei, D., Glezakou, V. A., Li, J. & Rousseau, R. Dynamic formation of single-atom catalytic active sites on ceria-supported gold nanoparticles. *Nat. Commun.* **6**, 1–8 (2015).

12.   Wang, X. *et al.* Insight into dynamic and steady-state active sites for nitrogen activation to ammonia by cobalt-based catalyst. *Nat. Commun.* **11**, 1–10 (2020).

13.   Shinjoh, H. *et al.* Suppression of noble metal sintering based on the support anchoring effect and its application in automotive three-way catalysis. *Top. Catal.* **52**, 1967–1971 (2009).

14.   Rao, R. G. *et al.* Interfacial charge distributions in carbon-supported palladium catalysts. *Nat. Commun.* **8**, (2017).

15.   Datye, A. K., Xu, Q., Kharas, K. C. & McCarty, J. M. Particle size distributions in heterogeneous catalysts: What do they tell us about the sintering mechanism? *Catal. Today* **111**, 59–67 (2006).

16.   Cho, H. R. & Regalbuto, J. R. The rational synthesis of Pt-Pd bimetallic catalysts by electrostatic adsorption. *Catal. Today* **246**, 143–153 (2015).

17.   Regalbuto, J. R. Strong Electrostatic Adsorption of Metals onto Catalyst Supports. *ChemInform* **38**, (2007).

18.   Regalbuto, J. R. *Catalyst Preparation: Science and Engineering (1st ed.).* (2006). doi:10.1201/9781420006506

19.   Cao, D. *et al.* Use of single atom catalysis for improvement of lignocellulosic conversion. *BioResources* **14**, 5018–5021 (2019).

20.   Wang, A., Li, J. & Zhang, T. Heterogeneous single-atom catalysis. *Nat. Rev. Chem.* **2**, 65–81 (2018).

21.   Kyriakou, G. *et al.* Heterogeneous Hydrogenations. **335**, 1209–1213 (2012).

22.   Chen, Y. *et al.* Single-Atom Catalysts: Synthetic Strategies and Electrochemical Applications. *Joule* **2**, 1242–1264 (2018).

23. Qi, K., Chhowalla, M. & Voiry, D. Single atom is not alone: Metal–support interactions in single-atom catalysis. *Mater. Today* **40**, 173–192 (2020).

24. Duke, A. S. *et al.* Active Sites in Copper-Based Metal Organic Frameworks: Understanding Substrate Dynamics, Redox Processes, and Valence Band Structure. *J. Phys. Chem. C* **119**, 27457 (2015).

25. Furukawa, H. *et al.* The chemistry and applications of metal-organic frameworks. *Science (80-.).* **341**, 1230444 (2013).

26. Chughtai, A. H., Ahmad, N., Younus, H. A., Laypkov, A. & Verpoort, F. Metal-organic frameworks: Versatile heterogeneous catalysts for efficient catalytic organic transformations. *Chem. Soc. Rev.* **44**, 6804–6849 (2015).

27. Lee, J. *et al.* Metal-organic framework materials as catalysts. *Chem. Soc. Rev.* **38**, 1450–1459 (2009).

28. Kozachuk, O. *et al.* Multifunctional, defect-engineered metal-organic frameworks with ruthenium centers: Sorption and catalytic properties. *Angew. Chemie - Int. Ed.* **53**, 7058–7062 (2014).

29. Islamoglu, T. *et al.* Postsynthetic Tuning of Metal-Organic Frameworks for Targeted Applications. *Acc. Chem. Res.* **50**, 805 (2017).

30. Yang, D. *et al.* Tuning Zr6 Metal-Organic Framework (MOF) Nodes as Catalyst Supports: Site Densities and Electron-Donor Properties Influence Molecular Iridium Complexes as Ethylene Conversion Catalysts. *ACS Catal.* **6**, 235–247 (2016).

31. Li, Z. *et al.* Sintering-Resistant Single-Site Nickel Catalyst Supported by Metal − Organic Framework. 5–10 (2016). doi:10.1021/jacs.5b12515

32. Drake, T., Ji, P. & Lin, W. Site Isolation in Metal − Organic Frameworks Enables Novel Transition Metal Catalysis. (2018). doi:10.1021/acs.accounts.8b00297

33. Chen, J. G., Menning, C. A. & Zellner, M. B. Monolayer bimetallic surfaces: Experimental and theoretical studies of trends in electronic and chemical properties. *Surf. Sci. Rep.* **63**, 201–254 (2008).

34. Sinfelt, J. H. Catalysis by alloys and bimetallic clusters. *Preprints* **21**, 350–352 (1976).

35. Ejegbavwo, O. A. *et al.* Heterometallic multinuclear nodes directing MOF electronic behavior. *Chem. Sci.* **11**, 7379–7389 (2020).

36. Dolgopolova, E. A. *et al.* Connecting Wires: Photoinduced Electronic Structure Modulation in Metal-Organic Frameworks. *J. Am. Chem. Soc.* **141**, 5350–5358 (2019).

37. Rice, A. M., Leith, G. A., Ejegbavwo, O. A., Dolgopolova, E. A. & Shustova, N. B. Heterometallic metal-organic frameworks (MOFs): The advent of improving the energy landscape. *ACS Energy Lett.* **4**, 1938–1946 (2019).

38. Metavarayuth, K. *et al.* Direct Identification of Mixed-Metal Centers in Metal-Organic Frameworks: Cu3(BTC)2Transmetalated with Rh2+Ions. *J. Phys. Chem. Lett.* **11**, 8138–8144 (2020).

39. Kumar, M., Chaudhari, R. V., Subramaniam, B. & Jackson, T. A. Ligand effects on the regioselectivity of rhodium-catalyzed hydroformylation: Density functional calculations illuminate the role of long-range noncovalent interactions. *Organometallics* **33**, 4183–4191 (2014).

40. Lang, R. *et al.* Hydroformylation of Olefins by a Rhodium Single-Atom Catalyst with Activity Comparable to RhCl(PPh3)3. *Angew. Chemie - Int. Ed.* **55**, 16054–16058 (2016).

41. Jörke, A., Seidel-Morgenstern, A. & Hamel, C. Rhodium-BiPhePhos catalyzed hydroformylation studied by operando FTIR spectroscopy: Catalyst activation and rate determining step. *J. Mol. Catal. A Chem.* **426**, 10–14 (2017).

42. Vilches-herrera, M. & Domke, L. Isomerization − Hydroformylation Tandem Reactions. (2014).

43. Arai, H. & Tominaga, H. Hydroformylation and hydrogenation of olefins over rhodium zeolite catalyst. *J. Catal.* **75**, 188–189 (1982).

44. Kim, T. *et al.* Gas-phase hydroformylation of propene over silica-supported PPh 3-modified rhodium catalysts. *Top. Catal.* **54**, 299–307 (2011).

45. Takahashi, N. & Kobayashi, M. Comparison of ethylene with propylene hydroformylation over a Rh-Y zeolite catalyst under atmospheric pressure. *J. Catal.* **85**, 89–97 (1984).

46. Gilliland, S. E. *et al.* Electrostatic adsorption-microwave synthesis of palladium nanoparticles on graphene for improved cross-coupling activity. *Appl. Catal. A Gen.* **550**, 168–175 (2018).

47. Eriksson, A. & Eriksson, A. Ti-Cu alloys for medical applications. (2019).

48. Bvcrist, L. C. de C. Basic components of a monochromatic XPS system. (2009). Available at: https://en.wikipedia.org/wiki/X-ray_photoelectron_spectroscopy#/media/File:System2.gif.

49. Duke, A. S. *et al.* Active Sites in Copper-Based Metal-Organic Frameworks: Understanding Substrate Dynamics, Redox Processes, and Valence-Band Structure. *J. Phys. Chem. C* **119**, 27457–27466 (2015).

50. Palomino, R. M. *et al.* Interfaces in heterogeneous catalytic reactions: Ambient pressure XPS as a tool to unravel surface chemistry. *J. Electron Spectros. Relat. Phenomena* **221**, 28–43 (2017).

51. AA, W. & LO, J. W. Overview of an Inductively Coupled Plasma (Icp) System. *Int. J. Chem. Res.* **3**, 41–48 (2011).

52. Greenfield, S. Inductively coupled plasma-atomic emission spectroscopy (ICP-AES) with flow injection analysis (FIA). *Spectrochim. Acta Part B At. Spectrosc.* **38**, 93–105 (1983).

53. Elemental, T. ICP or ICP-MS ? Which technique should I use? *A Thermo Electron buisness* 1–20 (2002).

54. Yang, D., Xu, P., Guan, E., Browning, N. D. & Gates, B. C. Rhodium pair-sites on magnesium oxide: Synthesis, characterization, and catalysis of ethylene hydrogenation. *J. Catal.* **338**, 12–20 (2016).

55. West, A. R. *Solid State Chemistry*.

56. Kosasih, F. U. & Ducati, C. Characterising degradation of perovskite solar cells through in-situ and operando electron microscopy. *Nano Energy* **47**, 243–256 (2018).

57. Dann, S. E., Abel, E. W., Davies, A. G., Phillips, D. & Woollins, J. D. *Reactions and Characterization of Solids*. (The Royal Society of Chemistry, 2000). doi:10.1039/9781847551825

58. O'Connell, K. & Regalbuto, J. R. High Sensitivity Silicon Slit Detectors for 1 nm Powder XRD Size Detection Limit. *Catal. Letters* **145**, 777–783 (2015).

59. Measurements, D. C. & Chemisorption, P. Comparison of Static and Dynamic Chemisorption Measurements. 1–3 (1990).

60. Webb, P. A. An Introduction to Chemical Adsorption Analytical Techniques and Methods. *Micromeritics* **13**, 5–7 (2016).

61. *AutoChem 2920 Automated Catalyst Characterization System Operator ' s Manual*. (2009).

62. Benson, J. E. & Boudart, M. Hydrogen-oxygen titration method for the measurement of supported platinum surface areas. *J. Catal.* **4**, 704–710 (1965).

63. Tengco, J. M. M., Lugo-José, Y. K., Monnier, J. R. & Regalbuto, J. R. Chemisorption-XRD particle size discrepancy of carbon supported palladium: Carbon decoration of Pd? *Catal. Today* **246**, 9–14 (2015).

64. Tubus, B. Schematic view of STEM mode. (2017). Available at: https://commons.wikimedia.org/wiki/File:STEM_fig.png#filelinks.

65. Lin, F. *et al.* Surface reconstruction and chemical evolution of stoichiometric layered cathode materials for lithium-ion batteries. *Nat. Commun.* **5**, 3529 (2014).

66. Van Benthem, K. *et al.* Three-dimensional imaging of individual hafnium atoms inside a semiconductor device. *Appl. Phys. Lett.* **87**, 1–4 (2005).

67. Muller, D. A. *et al.* Three-Dimensional Reconstructions and Atomic-Resolution Spectroscopic Imaging of Ensembles of Nanocatalyst Particles Across The Life Of A Fuel Cell. *Microsc. Microanal.* **18**, 1286–1287 (2012).

68. Jones, L., Macarthur, K. E., Fauske, V. T., Van Helvoort, A. T. J. & Nellist, P. D. Rapid estimation of catalyst nanoparticle morphology and atomic-coordination by high-resolution Z-contrast electron microscopy. *Nano Lett.* **14**, 6336–6341 (2014).

69. Liu, J. *et al.* CO2/H2O adsorption equilibrium and rates on metal-organic frameworks: HKUST-1 and Ni/DOBDC. *Langmuir* **26**, 14301–14307 (2010).

70. Wade, C. R. & Dincă, M. Investigation of the synthesis{,} activation{,} and isosteric heats of CO2 adsorption of the isostructural series of metal–organic frameworks M3(BTC)2 (M = Cr{,} Fe{,} Ni{,} Cu{,} Mo{,} Ru). *Dalt. Trans.* **41**, 7931–7938 (2012).

71. Gotthardt, M. A. *et al.* Synthesis and post-synthetic modification of amine-, alkyne-, azide- and nitro-functionalized metal-organic frameworks based on DUT-5. *Dalt. Trans.* **44**, 16802–16809 (2015).

72. Dolgopolova, E. A. *et al.* Electronic Properties of Bimetallic Metal-Organic Frameworks (MOFs): Tailoring the Density of Electronic States through MOF Modularity. *J. Am. Chem. Soc.* **139**, 5201 (2017).

APPENDIX A

SYNTHESIS AND CHARACTERIZATION OF MONOMETALLIC, BIMETALLIC,

AND INCIPIENT WETNESS CATALYSTS

Materials: $Cu(NO_3)_2 \cdot 2.5H_2O$ (98.3%, Mallinckrodt AR), $CoCl_2 \cdot 6H_2O$ (>98.0%, TCI America), $Co(OAc)_2 \cdot 4H_2O$ (98%, Alfa Aesar), $Co(NO_3)_2 \cdot 6H_2O$ (99%, STREM Chem. Inc), $NiCl_2 \cdot 6H_2O$ (98%, Alfa Aesar), $RuCl_3 \cdot H_2O$ (98%, Oakwood Chemical), $RhCl_3 \cdot H_2O$ (98.98%, Engelhard Chemicals), $IrCl_3 \cdot H_2O$ (99.9%, STREM Chemicals, Inc.), 1,3,5-benzene tricarboxylic acid (98%, Alfa Aesar), *N,N'*-dimethylformamide (DMF, ACS grade, BDH), ethanol (EtOH, 200 proof, Decon Laboratories, Inc.) were used as received.

$Cu_3(BTC)_2$ (CuBTC): The $Cu_3(BTC)_2$ MOF was synthesized based on a previously reported literature procedure.[69] A mixture of $Cu(NO_3)_2 \cdot 2.5H_2O$ (700 mg, 3.01 mmol), H_3BTC (470 mg, 2.24 mmol), and DMF: H_2O: EtOH (1:1:1 – 30.0 mL) was sonicated in a 40 mL vial for approximately 5 minutes. The mixture was heated at 75 °C in an oven for 24 hours. After cooling to room temperature, blue crystallites of $Cu_3(BTC)_2$ were collected by filtration and washed thoroughly three times with DMF (3×20 mL). PXRD studies confirmed the crystallinity of the bulk material before and after catalysis experiments (Figure A.1).

Ni₃(BTC)₂ (NiBTC): The $Ni_3(BTC)_2$ was prepared according to a previously reported literature procedure.[70] PXRD studies were employed to confirm the crystallinity of bulk material before and after catalysis experiments (Figure A.2).

Cu₂.₈₂Ru₀.₁₈(BTC)₂ [CuRh(6%)BTC]: The preparation of $Cu_{2.82}Ru_{0.18}(BTC)_2$ was achieved via direct synthesis based on a previously reported procedure.[71] A mixture of $Cu(NO_3)_2 \cdot 2.5H_2O$ (898 mg, 3.87 mmol), and $RuCl_3 \cdot H_2O$ (201 mg, 0.970 mmol) was dissolved in 25.0 mL of EtOH and poured into a flask containing H_3BTC (492 mg, 2.34 mmol) dissolved in 25.0 mL DMF. This mixture was heated in a flask at 60 °C for 24 hours with stirring. The blue-green powder obtained was collected by filtration and thoroughly washed several times with EtOH to remove any residual $RuCl_3$ salt. The material was then evacuated at 160 °C for 24 hours. PXRD studies confirmed the crystallinity of the bulk material before and after catalysis experiments (Figure A.3).

Cu₃₋ₓRhₓ(BTC)₂: The preparation of $Cu_{2.01}Rh_{0.99}(BTC)_2$ [CuRh(33%)BTC] and $Cu_{2.46}Rh_{0.54}(BTC)_2$ [CuRh(18%)BTC] MOFs was achieved by stirring a mixture of $Cu_3(BTC)_2$ powder (226 mg, 0.374 mmol) and 0.0386 M $RhCl_3 \cdot H_2O$ in EtOH (5.00 mL) in a flask for two and three days respectively at 90 °C on a hot plate. The green powder obtained was collected by filtration and thoroughly washed several times with EtOH to remove any residual $RhCl_3$ salt. During the wash procedure, the solvent was replaced twice a day for 72 hours before further characterization. The material was then evacuated at 160 °C for 24 hours. PXRD studies confirmed the crystallinity of the bulk material before and after catalysis experiments (Figure A.4 and A.5).

Cu$_{2.85}$Ir$_{0.15}$(BTC)$_2$ [CuIr(5%)BTC]: The preparation of Cu$_{2.85}$Ir$_{0.15}$(BTC)$_2$ was achieved by stirring a mixture of Cu$_3$(BTC)$_2$ powder (226 mg, 0.374 mmol) and 0.008 M IrCl$_3$·H$_2$O in EtOH (5.00 mL) in a flask for three days at 90 °C on a hot plate. The blue-green powder obtained was collected by filtration and thoroughly washed several times with EtOH to remove any residual IrCl$_3$ salt. During the wash procedure, the solvent was replaced twice a day for 72 hours before further characterization. The material was then evacuated at 160 °C for 24 hours. PXRD studies were used to confirm the crystallinity of bulk material before and after catalysis experiments (Figure A.6).

Cu$_{1.5}$Co$_{1.5}$(BTC)$_2$[CuCo(50%)BTC]: It was prepared according to a previously reported procedure.[72] Freshly prepared Cu$_3$(BTC)$_2$ (0.135gm, 0.203 mmol) was heated in a solution of CoCl$_2$·6H$_2$O in DMF (0.441 M, 10 mL]) at 90 °C for 24 hours in an isothermal oven. After heating, the reaction mixture was cooled down to room temperature, and the resulting green powder was washed thoroughly with DMF to remove excess CoCl$_2$. During the wash procedure, the solvent was replaced twice a day over 72 hours before further characterization. After DMF washing, the powder underwent a solvent exchange process with dichloromethane at room temperature. PXRD studies confirmed the crystallinity of the samples before and after catalysis experiments (Figure A.7).

Cu$_{2.82}$Ni$_{0.16}$(BTC)$_2$ [CuNi(6%) BTC]: It was prepared by modification of the literature procedure used for Cu$_{1.5}$Co$_{1.5}$(BTC)$_2$ synthesis. In a 20 mL vial, freshly prepared Cu$_3$(BTC)$_2$ (0.135 g, 0.203 mmol) and a solution of NiCl$_2$·6H$_2$O (0.33 M, 10 mL DMF) were heated at 90 °C for 24 hours in an isothermal oven. After heating, the reaction

mixture was cooled down to room temperature, and the resulting green powder was washed thoroughly with DMF to remove excess $NiCl_2$. PXRD studies confirmed the crystallinity of the samples before and after catalysis experiments (Figure A.8).

Rh^{2+}/SiO_2, Rh^{3+}/SiO_2 (Incipient Wetness Catalysts): The Rh^{2+}/SiO_2 (Aerosil, OX-50) catalyst was synthesized by incipient wetness impregnation (IWI) using the following procedure: an aqueous solution of $Rh_2(OAc)_4$ was prepared (water accessible pore volume for the silica support=0.82 mL/g), this solution was added in small aliquots to the support while ensuring the sample was well-mixed, and the catalyst was dried at room temperature under vacuum for 3 days. XPS analysis confirmed an oxidation state of Rh^{2+}. The Rh^{3+}/SiO_2 IWI catalyst was prepared in a similar manner using $RhCl_3$ and dried at 120 °C.

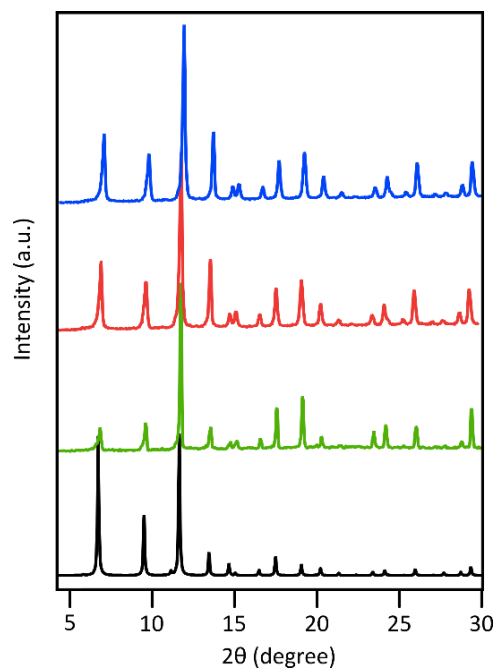**Figure A.1.** PXRD patterns of $Cu_3(BTC)_2$: simulated (black, for reference); as-synthesized (green); and activated before (red) and after (blue) catalysis experiments.

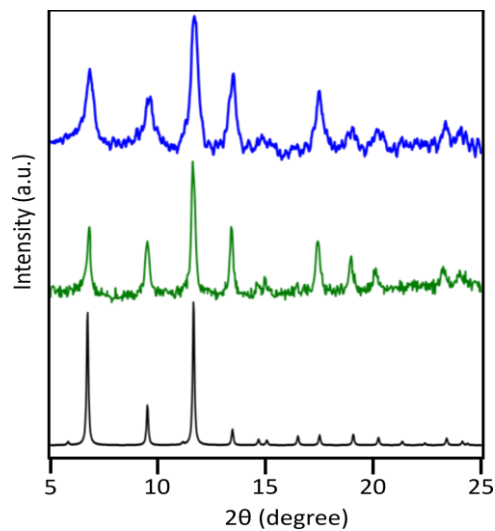**Figure A.2.** PXRD patterns of $Ni_3(BTC)_2$: simulated (black); as-synthesized (green); and after catalysis experiments (blue).
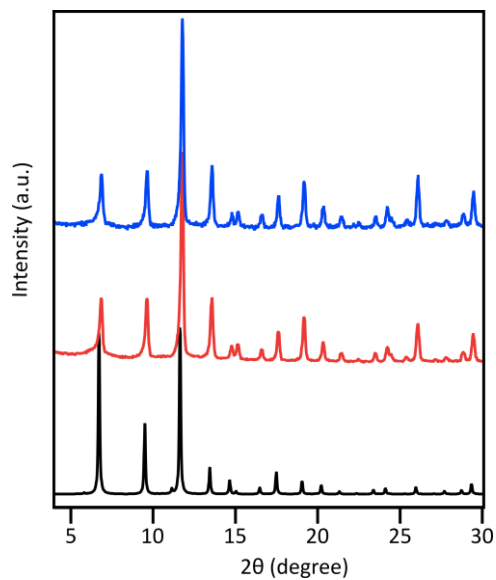
Figure A.3. PXRD patterns of: $Cu_3(BTC)_2$ simulated (black, for reference); and activated $Cu_{2.82}Ru_{0.18}(BTC)_2$ before (red) and after (blue) catalysis experiments.

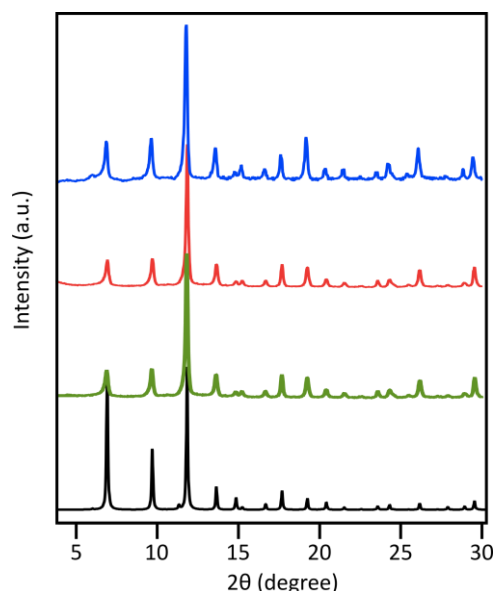**Figure A.4.** PXRD patterns of: $Cu_3(BTC)_2$ simulated (black, for reference); and $Cu_{2.01}Rh_{0.99}(BTC)_2$: as-synthesized (green); and activated before (red) and after (blue) catalysis experiments.

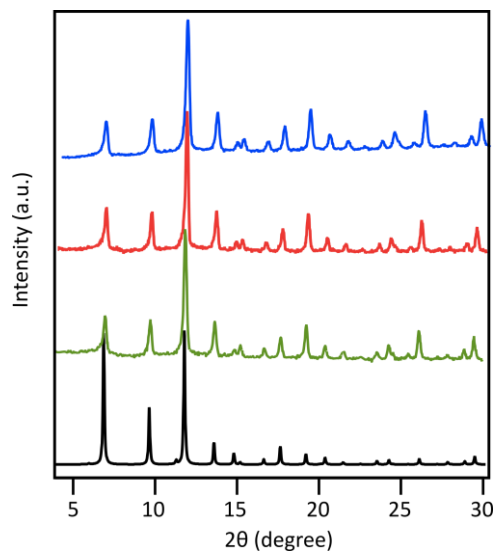**Figure A.5.** PXRD patterns of $Cu_3(BTC)_2$ simulated (black, for reference); and $Cu_{2.46}Rh_{0.54}(BTC)_2$:as-synthesized (green); and activated before (red) and after (blue) catalysis experiments.
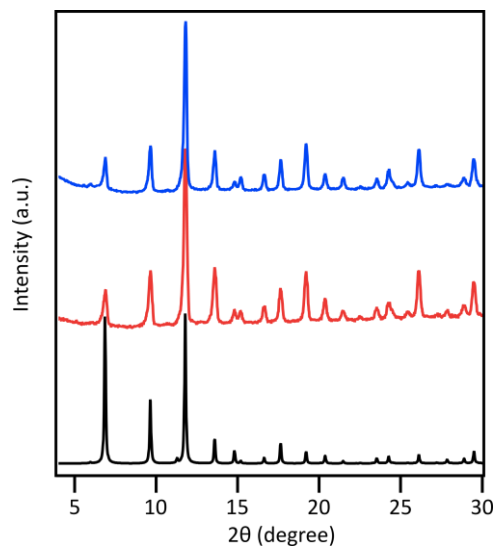

Figure A.6. PXRD patterns of $Cu_3(BTC)_2$ simulated (black, for reference); and activated $Cu_{2.85}Ir_{0.15}(BTC)_2$ before (red) and after (blue) catalysis experiments.

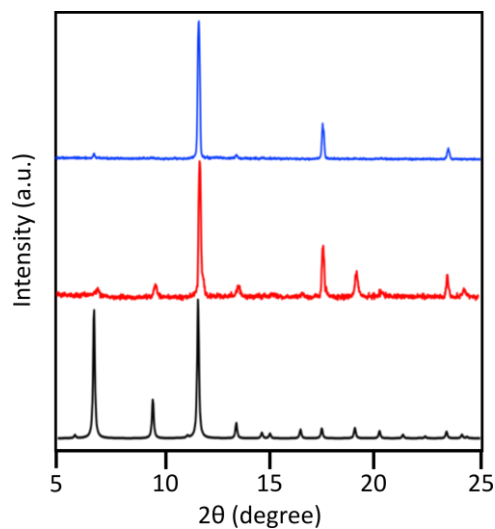**Figure A.7.** PXRD patterns of: $Cu_3(BTC)_2$ simulated (black, for reference); $Cu_{1.5}Co_{1.5}(BTC)_2$ as-synthesized (red); and activated $Cu_{1.5}Co_{1.5}(BTC)_2$ after catalysis experiments (blue).

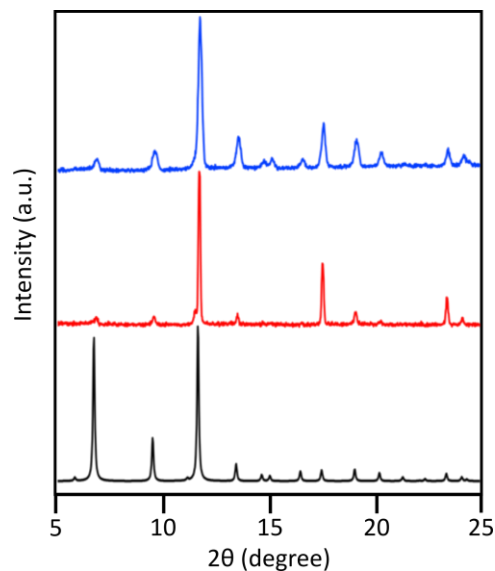**Figure A.8.** PXRD patterns of: $Cu_3(BTC)_2$ simulated (black, for reference); $Cu_{2.82}Ni_{0.18}(BTC)_2$ as-synthesized (red); and activated $Cu_{2.82}Ni_{0.18}(BTC)_2$ after catalysis experiments (blue).

APPENDIX B:

COPYRIGHT PERMISSION

CHAPTER 3

Selective Catalytic Chemistry at Rhodium(II) Nodes in Bimetallic Metal–Organic Frameworks
Author: Deependra M. Shakya, Otega A. Ejegbavwo, Thayalan Rajeshkumar, et al
Publication: Angewandte Chemie International Edition
Publisher: John Wiley and Sons
Date: Sep 17, 2019

© 2019, Wiley-VCH Verlag GmbH & Co. KGaA, Weinheim

Order Completed

Thank you for your order.

This Agreement between University of South Carolina -- Deependra Shakya ("You") and John Wiley and Sons ("John Wiley and Sons") consists of your license details and the terms and conditions provided by John Wiley and Sons and Copyright Clearance Center.

Your confirmation email will contain your order number for future reference.

License Number	5201461344391		Printable Details
License date	Dec 05, 2021		

📄 Licensed Content		📋 Order Details	
Licensed Content Publisher	John Wiley and Sons	Type of use	Dissertation/Thesis
Licensed Content Publication	Angewandte Chemie International Edition	Requestor type	Author of this Wiley article
Licensed Content Title	Selective Catalytic Chemistry at Rhodium(II) Nodes in Bimetallic Metal-Organic Frameworks	Format	Print and electronic
Licensed Content Author	Deependra M. Shakya, Otega A. Ejegbavwo, Thayalan Rajeshkumar, et al	Portion	Full article
Licensed Content Date	Sep 17, 2019	Will you be translating?	No
Licensed Content Volume	58		
Licensed Content Issue	46		
Licensed Content Pages	6		

📄 About Your Work		📁 Additional Data	
Title	MODIFICATION OF ACTIVE SITES IN CATALYTIC MATERIALS FOR GAS-PHASE HETEROGENEOUS CATALYSIS	Order reference number	5201410072905
Institution name	University of South Carolina		
Expected presentation date	Jan 2022		

📍 Requestor Location		📋 Tax Details	
	University of South Carolina	Publisher Tax ID	EU826007151
	631 Sumter Street		
	GSRC 227		
Requestor Location			
	COLUMBIA, SC 29208		
	United States		
	Attn: University of South Carolina		

$ Price	
Total	0.00 USD